Characterization of the Viscoelastic Fracture of Solvated Semi-Interpenetrating Polymer Network (S-IPN) Silicone Hydrogels

Geoffrey A. Tizard III

Thesis submitted to the faculty of the Virginia Polytechnic Institute and State University in partial fulfillment of the requirements for the degree of

Master of Science in

Engineering Mechanics

David A. Dillard – Committee Chairman

Scott W. Case

Robert B. Moore

Peyton L. Hopson

July 22, 2010
Blacksburg, VA

Keywords: semi-interpenetrating polymer network, solvated hydrogels, viscoelasticity, constrained tension fracture, time-dependent fracture

Characterization of the Viscoelastic Fracture of Solvated Semi-Interpenetrating Polymer Network (S-IPN) Hydrogels

Geoffrey A. Tizard III

ABSTRACT

The unique compressive, optical, and biocompatible properties of silicone hydrogels allow them to be used in a wide variety of applications in the biomedical field. However, the relatively weak mechanical behavior, as well as the highly deformable nature of these elastomeric materials, presents a myriad of challenges when attempting to understand their constitutive and fracture properties in order to improve hydrogel manufacturing and performance in applications. In this thesis, a series of experimental techniques were developed or adapted from common engineering approaches in order to investigate the effects of rate and temperature on the viscoelastic constitutive and fracture behavior of two solvated semi-interpenetrating polymer network silicone hydrogel systems.

Viscoelastic characterization of these material systems was performed by implementing a series of uniaxial tension and dynamic mechanical analysis shear tests in order to generate relevant master curves and corresponding thermal shift factors of such properties as shear relaxation modulus, dynamic moduli, and the loss factor. Concurrently, the cohesive fracture properties were studied by utilizing a “semi-infinite” strip geometry under constrained tension in which thin pre-cracked sheets of these cured hydrogels were exposed to several different loading conditions. Fracture tests were performed over a relevant range of temperatures and crosshead rates to determine and generate a master curve of the subcritical strain energy release rate. Experimental methods utilizing high-speed camera images and digital image correlation to monitor viscoelastic strain recovery in the wake of a propagating crack were explored. The results from this thesis may prove useful in an investigation of the interfacial fracture of these hydrogel systems on several different polymer substrates associated with an industrial manufacturing problem.

ACKNOWLEDGMENTS

I would like to thank my advisors Dr. David Dillard, Dr. Scott Case, and Dr. Robert Moore for their support, encouragement, and insight over the duration of this project. And a special thanks to Dr. Peyton Hopson who has served as a technical project monitor on this project over the past two years. Honestly, I am grateful for the opportunity to have worked on such a unique and intriguing project, especially with such a remarkable and knowledgeable committee.

I would also like to thank Steve Pegram and Kerry Sanders for their continued support and collaboration over the past two years which were invaluable in helping to complete this research.

Thank you to the Engineering Science and Mechanics department and the Institute for Critical Technology and Applied Science (ICTAS) for the use of their facilities throughout the duration of this project.

A special thanks to Melissa Nipper for her constant encouragement and willingness to help all of us in the Materials Response Group.

Also, I would like to express tremendous gratitude to my colleagues and lab-mates that have provided me with a one of a kind learning experience while working in the Adhesion Mechanics Lab. Their support and friendship truly made all the difference. Thank you to Hitendra Singh, Kshitish Patankar, Edoardo Nicoli, Katie Murray, Lei Yan, Youliang Guan, Justin Klein, Jake Grohs, Katherine Finlay, and Chase Siuta.

I also owe a special thanks to Gina Cruz and Cadence Martin for their help in producing samples and performing experiments. Having the opportunity to mentor two undergraduate students as intelligent and hardworking as you was my pleasure.

Finally, I am blessed to have such a supporting and loving family that has always been there for me, and has continually encouraged me to better myself. This is not only a personal achievement, but a reminder of the beliefs and values my parents, Jeff and Patti Tizard, have instilled upon me.

Table of Contents

List of Figures

List of Tables

Chapter 1 : Introduction

Motivation

Synthetic hydrogels are an emerging class of soft and highly permeable hydrophilic polymers which contain networks of chemically or physically crosslinked polymer chains. Hydrogels, like most classes of material systems, have a variety of types such as the acrylic and bio-gelatins which are mechanically weak compared to the semi-interpenetrating polymer network and double network hydrogel systems which have demonstrated high compressive and tensile strengths [1, 2]. Also, the elastomeric nature of hydrogel material systems, which offers a high degree of flexibility analogous to natural tissue, combined with impressive optical, adhesive, and compressive properties, gives this class of polymeric materials a large variety of uses in the biomedical field. Current applications of hydrogels range from contact lenses and wound dressings to drug delivery units targeting specific cells in the body and tissue scaffolds for tissue repair [3, 4]. Despite this vast array of life-improving applications, there has been limited research on the constitutive and fracture behavior of synthetic hydrogels and relatively little to no research on these hydrogel systems in a solvated or pre-hydrated state often found in the molding and manufacturing of hydrogels in such applications as contact lenses and medical bandages. By developing engineering methods to adequately test and characterize solvated hydrogel systems, improvements to the manufacturing of hydrogel based products leading to a reduction in waste as well as a better understanding of the material behavior furthering the advancement of hydrogel applications can be achieved.

Many manufacturing processes of hydrogel material products resort to complex molding techniques which require an eventual demold of the hydrogel material from a system of substrates in a highly clean and controlled environment. The soft and relatively weak nature of hydrogel materials, especially in the solvated state, makes them prone to tearing and other flaws during this process. Successful removal of these materials from their molds during manufacturing can require a fine balance between adhesive and cohesive properties, which are often rate and temperature-dependent. In order to adequately approach and resolve such issues during manufacturing, a complete understanding of the viscoelastic constitutive and fracture behavior of the bulk polymer and interface are necessary. With such a complex problem, this thesis sets out to investigate the bulk viscoelastic fracture behavior of two specific silicone hydrogels in their solvated state in order to aid in a manufacturing issue by utilizing viscoelasticity, rubber elasticity, and fracture mechanics concepts.

Thesis Organization

This thesis consists of five chapters written in the format of a book in which each of the main chapters, Chapter 2 through Chapter 4 of this document, contain a separate in-

depth literature review, located in the Introduction and Background section of each chapter, on the topics discussed in the chapter. Chapter 2 of this thesis briefly discusses the solvated hydrogel material systems used in this study and the procedure implemented to fabricate bulk samples, and the remaining four chapters pertain to this investigation of the viscoelastic fracture behavior of two solvated semi-interpenetrating polymer network (S-IPN) silicone hydrogel systems which are referred to throughout this document as Hydrogel A and B. Although Chapter 3 and Chapter 4, can be considered as independent works, these chapters represent the progression of a comprehensive and structured study of the viscoelastic constitutive and bulk fracture properties deemed responsible for causing defects during the manufacturing of these hydrogel materials for a particular application. Chapter 3 of this document discusses the use of dynamic mechanical analysis (DMA) and uniaxial tension testing to study the effects of rate and temperature of these bulk solvated hydrogel systems. Expanding upon the results from this viscoelastic study, Chapter 4 focuses on the implementation of a constrained tension fracture approach adapted for testing semi-infinite strips of these cured monomer systems under several different loading rates and scenarios as well as a range of relevant temperatures in order to generate subcritical strain energy release rate (SERR) curves. Also, Chapter 4 discusses methods to characterize the time-dependent fracture of soft materials, such as these solvated hydrogels, using unique experimental techniques to capture possible viscoelastic dissipation during fracture to further investigate bulk viscoelastic fracture of these solvated S-IPN hydrogel systems.

Although several collaborators have been involved in this research effort and may be co-authors of eventual future publication of these studies, the author of this thesis is the major contributor of the works contained in this document. However, some figures and data pertaining to the interfacial fracture of these solvated hydrogel systems from several different glassy substrates, presented in Chapter 4, were obtained from a collaborator in order to present a comparison between bulk and interfacial fracture.

Supplementary work from several side studies on these solvated hydrogel material systems, which were found to be of significant interest to this research but not included in the body of this work, can be found in the appendices. In particular, prolonged solvent egress studies considered important to the work performed Chapter 3 and Chapter 4 as well as scanning electron microscope images of the fracture surface of the solvated hydrogel systems are examples of such items included in the appendices. Also, tabulated summaries of relevant data and examples of the MATLAB® script used to process the fracture images from the high speed camera can be found in the appendices.

Goals

The research contained in this thesis seeks to develop adapted engineering material testing approaches in order to better understand the viscoelastic constitutive and

fracture behavior of soft material systems, such as the solvated silicone hydrogels investigated herein. By determining methods to adequately characterize these viscoelastic and fracture properties, improvements and advancements in regards to the manufacturing and application of hydrogel systems can be achieved. The following outline lists the specific goals which were deemed crucial in understanding the relevant behavior of Hydrogel A and B pertinent to improving and modeling a manufacturing process for a particular hydrogel application.

Develop and refine a method to cast bulk hydrogel material samples (Chapter 2)

- In order to successfully characterize the constitutive and fracture properties of the bulk hydrogel systems, a standard method to cure samples is necessary as excess oxygen can create voids, and flexible molding materials can result in non-uniform thickness throughout a single sample which can be problematic for testing methodologies.

Characterize the viscoelastic behavior of two representative hydrogel systems by implementing the time temperature superposition principle (TTSP) to form master curves of dynamic moduli data from dynamic mechanical analysis (Chapter 3)

- Determining the temperature and time-dependence of both hydrogel systems over a range of relevant rates or frequencies and temperatures can provide fundamental information on the hydrogels' behavior during a manufacturing process which can occur at high rates and various temperatures.

- Acquiring valid viscoelastic properties is crucial to developing a finite element model to aid in investigating the manufacturing processes of these hydrogel systems.

- Applying the TTSP can aid in correlating experimental testing rates to manufacturing rates in regards to demolding hydrogels from various substrates and be used to determine the correct temperatures to perform experimental tests in order to match the manufacturing case.

Develop a method to successfully collect bulk fracture data to generate the bulk subcritical strain energy release rate curves for both hydrogel systems as a function of crack propagation rate (Chapter 4)

- Characterizing the bulk fracture of these hydrogel systems can provide insight into the threshold strain energy release rates (SERR) at which a flaw or crack in the material will not propagate as well as the critical fracture energies at which failure is catastrophic.

Develop a method to investigate the temperature and time-dependent fracture of the solvated hydrogel systems in a constrained tension fracture geometry (Chapter 4)

- By determining a means to experimentally observe the temperature and time-dependent fracture of these material systems, fracture behavior relevant to high-speed and controlled environment manufacturing processes used to create hydrogel materials in their applied state can be better understood.

In an effort to aid the advancement and innovation of hydrogel research, manufacturing, and application, the chapters of this thesis provide a series of engineering approaches to successfully characterize the viscoelastic constitutive and fracture behavior of solvated hydrogel systems. Chapter 2 discusses the hydrogel materials investigated in this thesis as well as introduce a method to cast bulk hydrogel samples; Chapter 3 investigates the rate and temperature dependence of both Hydrogel A and B; Chapter 4 discusses the use of a constrained tension fracture geometry to determine the SERR of the bulk hydrogel systems and attempts to investigate the time-dependent fracture of solvated hydrogel systems based on experimentally collected constitutive and fracture data.

Chapter 2 : Materials and Fabrication

Introduction and Background

Hydrogels are typically regarded as chemically or physically crosslinked hydrophilic polymers that are highly water swollen viscoelastic solids [2]. These characteristics of hydrogel materials, combined with their extraordinary compressive and adhesive strength as well as excellent biocompatibility, have allowed them to be implemented into a variety of biomedical applications [5]. Although considerable research has been performed in order to explore and improve the various applications and synthesis of these materials in their final water-swollen state, there has been limited research on the solvated or pre-hydrated state in which these materials are manufactured such as the case for cartilage replacement components and contact lenses. By extensively studying the bulk viscoelastic and fracture behavior of these solvated hydrogels, it is possible to improve upon manufacturing techniques in order to reduce waste and advance the applications of hydrogels.

As mentioned in Chapter 1, this thesis discusses the viscoelastic fracture behavior of two semi-interpenetrating polymer network (S-IPN) silicone hydrogel systems in an un-hydrated or solvated state as found during the manufacturing of these materials before being hydrated and used for various applications. In general, interpenetrating polymer networks (IPNs) consist of two or more polymers in network form in which one polymer is polymerized and/or crosslinked in the presence of the others. Figure 2-1 illustrates an IPN with two crosslinked polymer networks, while Figure 2-2 depicts a S-IPN often referred to as a pseudo-IPN [6, 7]. These S-IPN hydrogel systems consist of one or more crosslinked networks and one or more linear or branched polymers which penetrate at least one of the existing networks resulting in a polymer blend with increased mechanical strength and fine morphology [8-10]. Compared to the acrylic hydrogels and bio-gelatins often used for low elastic biomedical and food industry applications, S-IPN hydrogels exhibit a much greater toughness which is even comparable to double network (DN) hydrogel systems [1]. This observed increase in toughness of DN and S-IPN hydrogels arises from a combination of effects, most notably the high heterogeneity of the first network and the ability to redistribute stress concentrations at crack tips to the second network or pseudo second network for S-IPN systems, thus resulting in the creation of a large damage zone [1, 11]. Also, research performed by Webber *et al.* indicates that although DN systems show high toughness values on the initial loading, the resulting mechanical responses from additional loadings showed a lower stiffness and dissipation which stems from alterations in the network structures from the first loading [1, 11]. Additionally, S-IPN and DN hydrogel systems are considered thermoset which makes them resistant to flow while the primary chemical bonds remain unbroken [6].

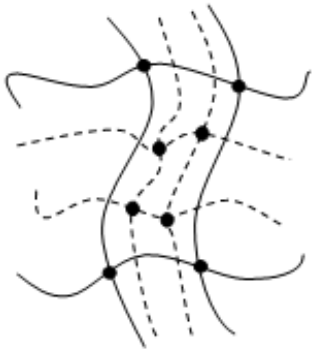

Figure 2-1: Interpenetrating network with two crosslinked polymers (double network)

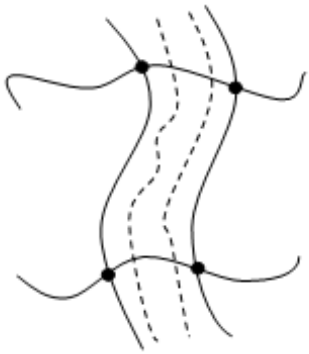

Figure 2-2: Semi-interpenetrating network

The two S-IPN hydrogel systems investigated in this thesis are referred to as Hydrogel A and B, and were received as monomers. The main differences between these cured systems are that Hydrogel A possesses a higher crosslink density and lower solvent content, approximately 22% by weight, compared to Hydrogel B which contains a lower crosslink density and a solvent content that is 42% by weight. These materials, in their cured state, are both highly deformable due to similar amounts of silicone, approximately 30-40% by weight, and relatively low glass transition temperatures of -12^{o}C for Hydrogel A and -90^{o}C for Hydrogel B. Although the material content and properties of these two solvated systems differ, similar precautions and considerations should be taken when investigating hydrogel materials, especially in regards to solvent loss.

Table 2-1: Summary of Hydrogel A and B comparison

	Hydrogel A	**Hydrogel B**
Solvent Content (% weight)	21	42
Glass Transition Temperature, T_g, (^{o}C)	-12	-90
Silicone Content (% weight)	30-40	30-40

When researching hydrogel systems, both diluent ingress and egress are critical concerns which can drastically change the material behavior of hydrogel systems. Mechanical testing of hydrogel materials are often performed in controlled environments that are thermally regulated and have the hydrogel completely immersed in an aqueous solution in order to maintain a swollen equilibrium [2]. Although this is the case for typical hydrogels, solvated hydrogel systems, such as the hydrogels used in this study, do not experience significant uptake of water from the atmosphere since they contain water immiscible diluents which restrict water uptake until the diluents are removed from the system; however, they do exhibit sensitivity to solvent loss. A reduction in the

solvent content of one of these solvated hydrogel systems can drastically change material properties and molecular behavior as these diluents act as internal plasticizers; therefore, measures must be taken to prevent solvent loss from cured samples before and during testing. For Hydrogel A and B, both systems were shown to exhibit solvent loss after they are cured and exposed to ambient air conditions, as presented in Appendix A; however, Hydrogel A proved to be more susceptible to losing solvent compared to Hydrogel B.

Before testing of these materials could begin, a facility to cure bulk samples of these hydrogels was constructed. During the investigation of the bulk material properties of these two solvated hydrogel systems, details and refinements which improved and facilitated the fabrication process of bulk hydrogel samples were discovered. The following sections of this chapter provide detailed overviews of the procedure used to prepare the monomer systems before casting them, as well as the process used to fabricate the bulk samples for both constitutive and fracture testing.

Bulk Sample Fabrication Process

The fabrication process for both Hydrogel A and B begins by degassing the received jars of monomer in a vacuum chamber with an attached vacuum pump, presented in Figure 2-3, at a gage pressure of approximately -85 kPa (-0.85 bar) for at least an hour in order to remove residual oxygen and voids before casting specimens. After degassing the monomer, nitrogen was released into the vacuum chamber and the uncured hydrogel monomer was immediately placed into a nitrogen-filled acrylic glove box from Terra Universal® (Fullerton, CA), shown in Figure 2-4, with oxygen concentrations below 1% and at a temperature of 60°C. Concentrations of oxygen above this 1% threshold can prohibit curing of these hydrogel monomer systems. Nitrogen was provided from a Terra Universal® nitrogen generator, model No. 2700-09A, set to a purity level of no less than 98%. The produced nitrogen was regulated using a simple flow meter mounted above the glove box. The uncured monomer inside the jars was allowed to equilibrate before casting samples. The entire curing setup for these hydrogel systems is presented in Figure 2-5. During the entire curing process, the overhead fluorescent lighting was turned off and all natural light was blocked in order to prevent immediate curing of the monomer due to the emitted frequency of light. Instead, the room was lit with yellow fluorescent lighting (Philips® F32T8/TL 730) which lacks the particular wavelengths, 490 nm and below, that can initiate curing.

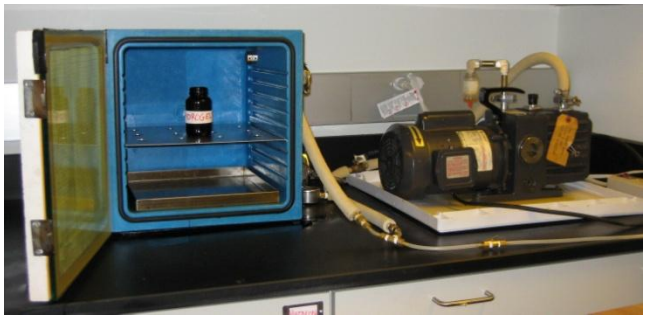

Figure 2-3: Vacuum chamber and pump

Figure 2-4: Acrylic glove box for curing

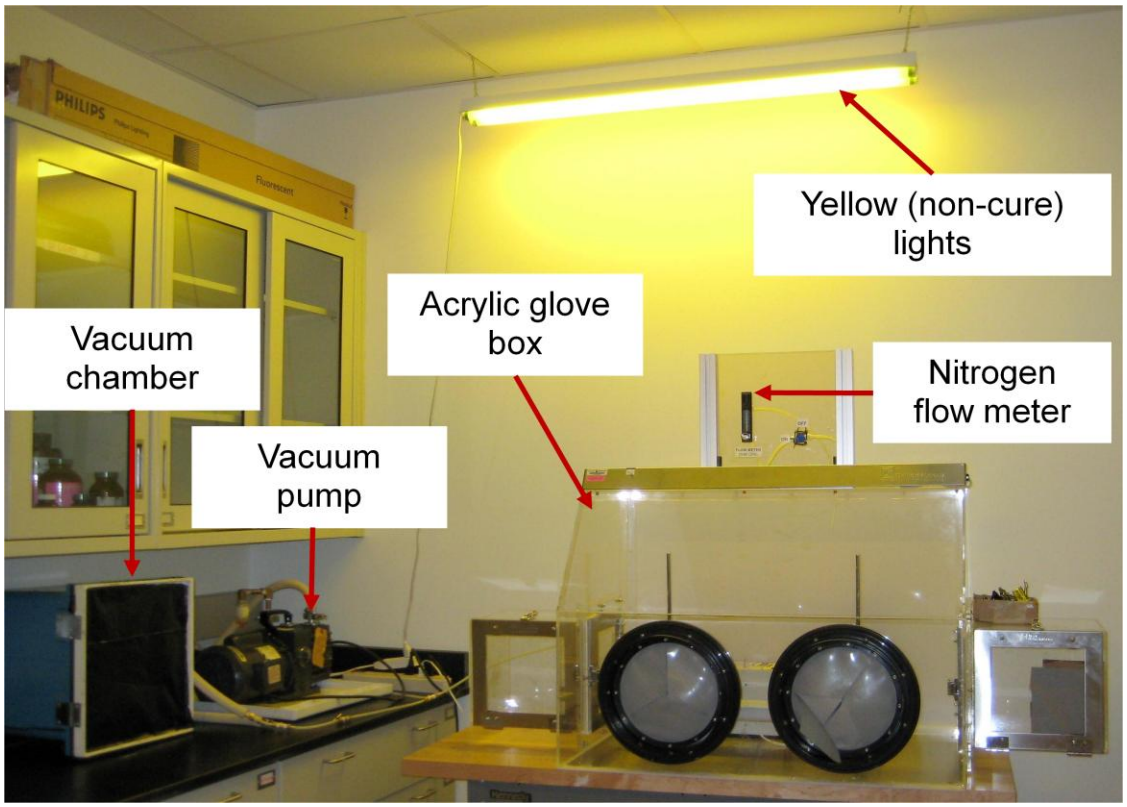

Figure 2-5: Hydrogel curing setup

For bulk samples used in both the viscoelastic constitutive and fracture studies presented in Chapter 3 and Chapter 4, respectively, the uncured monomer was poured into a five-layer sandwich mold, depicted in Figure 2-6, consisting of two rigid outer glass plates, two interior layers of polypropylene release film each with a thickness of 1.8 mm, and a central rubber-silicone gasket approximately 1.8 mm thick, all of which was secured using binder clips. The polypropylene and rubber-silicone were exposed to the nitrogen-filled environment inside the glove box for a period of at least 6 hours before curing bulk samples in order to prevent entrapped oxygen from entering the degassed hydrogel monomer. Although the overall size, length by width, of the sheet was different for the viscoelastic samples compared to the fracture samples, this

technique allowed for sheets of the desired hydrogel system to be cured with a uniform thickness of approximately 1.8 mm. The sample was then placed parallel to a set of specialty actinic lights (Philips® TLK 40W/03), shown in Figure 2-7, that emit radiation in the range of 380 to 480 nm. The radiation from this light system is capable of initiating the curing process of the monomer systems. While placed under these lights, the samples were exposed to an intensity of 0.5 mW/m^2 for a period of 10 minutes. The sheets of cured monomer were contained within the polypropylene sheets until they were prepared for testing in order to prevent the loss of solvent which has been shown to drastically change the material properties of the solvated hydrogel systems. For further information on the solvent egress from Hydrogel A and B, refer to Appendix A.

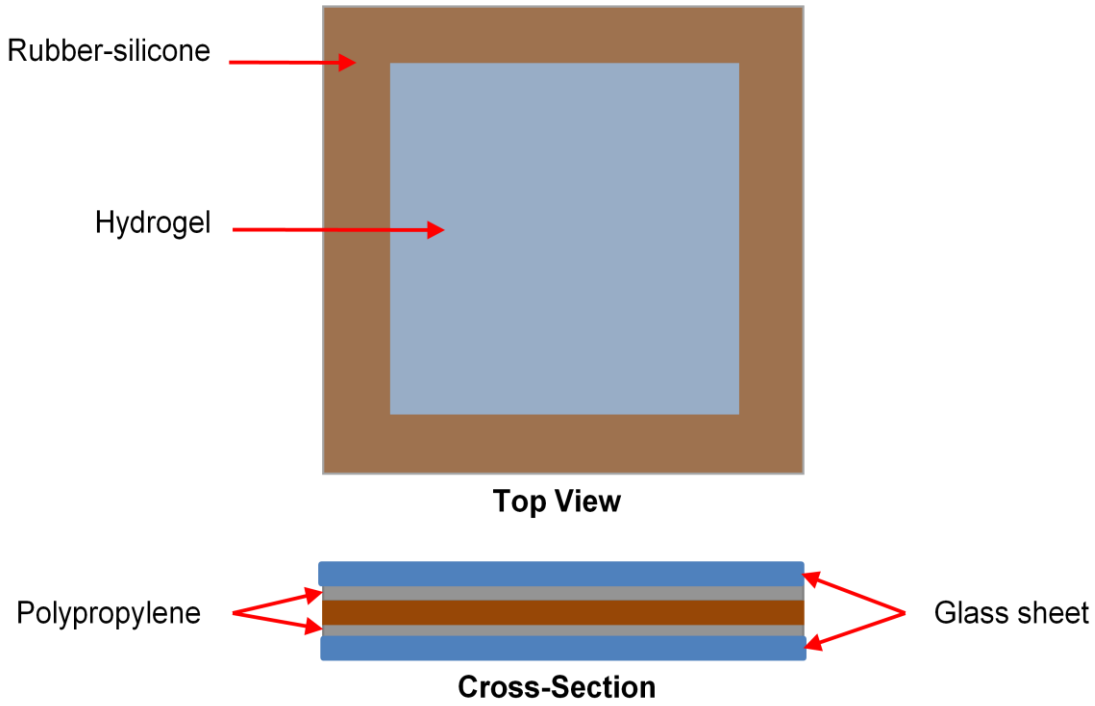

.

Figure 2-6: Diagram of 5 layer bulk sample mold (top and cross-sectional views)

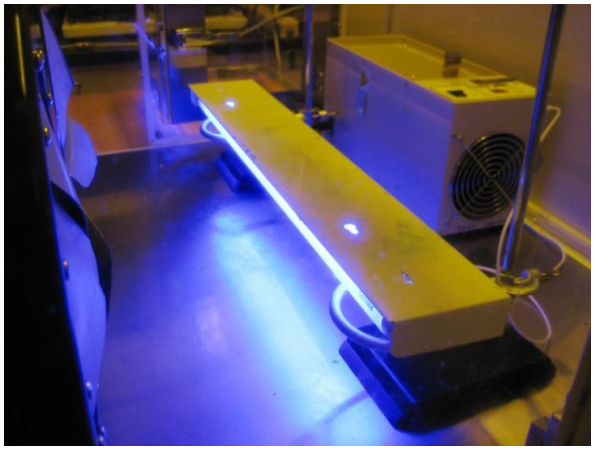

Figure 2-7: Close up of UV curing light source inside glove box

Summary of Solvated Hydrogel Materials and Bulk Fabrication Procedure

The goal of this section was to introduce the solvated S-IPN hydrogel systems, Hydrogel A and B, investigated in this study and present the method used to cure and prepare bulk solvated hydrogel samples for various engineering material tests as well as discuss some of the critical concerns or factors which can change the behavior of solvated hydrogels. Although Hydrogel A and B possess different levels of solvent and silicone content as well as glass transition temperatures, they are shown to be relatively sensitive to levels of oxygen present during the curing process and solvent loss when directly exposed to the atmosphere. The effects of an over abundance of oxygen present when casting the hydrogel samples are considered and prohibited by thoroughly degassing the uncured monomer and exposing the components used to mold the hydrogels into sheets in a high level nitrogen environment for an extended period of time before testing. Also, properly storing the samples before preparation and immediately testing the bulk samples after being cured was shown to reduce the possibility of solvent loss which has been shown to increase the stiffness of the solvated hydrogel material.

Chapter 3 : Evaluating the Viscoelastic and Hyperelastic Constitutive Properties of Solvated Hydrogel Systems

Introduction and Background

Characterization of the temperature and time-dependence of chemically crosslinked silicone hydrogels is critical when manufacturing and integrating these soft elastomeric materials into the human body, as is done with many of the biomedical applications of hydrogels. Even in the solvated state, it is important to fully understand the viscoelastic behavior of hydrogel materials in order to improve manufacturing processes and reduce waste. Although there are many different instruments and mechanical testing procedures to determine the viscoelastic properties of elastomeric materials, this chapter discusses the use of dynamic mechanical analysis (DMA) and uniaxial tension testing to investigate and compare the respective small scale viscoelastic behavior and large scale hyperelastic behavior of Hydrogel A and B.

DMA testing of polymeric or composite materials can provide fundamental information on a particular material's temperature and time-dependence which is important when considering or improving a material for a specific application [12]. Dynamic mechanical analyzers offer a wide range of test methods which are capable of collecting appropriate information used to characterize the viscoelastic behavior of a wide variety of material systems by means of steady state oscillation, creep, or stress relaxation test modes by imposing either a predetermined strain or load on the material sample [13, 14]. The test methods vary based on the clamp selection which include; tension, compression, three-point bending, dual cantilever, and shear. Although there are a variety of test procedures and clamps, the most relevant and easy to perform in order to obtain viscoelastic data for hydrogel systems and other types of soft materials involves the shear sandwich clamps operated over a range of temperatures and frequencies [2, 15, 16].

Since some soft materials exhibit poor tensile strength and complexities due to friction and boundary conditions with compression testing, the shear sandwich grips operated under a sinusoidal shear deformation have proven to work exceptionally well for characterizing soft materials such as hydrogels, denture linings, and other elastomeric biomaterials [12, 17, 18]. Creton *et al.* have shown great success in characterizing the viscoelastic behavior of nano-structured polyelectrolyte hydrogels and hybrid hydrogels utilizing this shear testing method with the DMA [19, 20]. Although it is dependent on the application, this technique produces highly relevant results since it simulates the type and rate of deformation biocompatible soft materials would experience clinically [17, 21, 22].

While conducting experiments with this multi-frequency strain mode on the DMA, the stress, σ, on the material is simultaneously measured with strain. Once equilibrium is

achieved for a linear viscoelastic material, the stress and strain vary sinusoidally with angular frequency, ω, as presented in Equation (1) and Equation (2), respectively. However, the strain lags behind the stress as suggested by the incorporation of the phase lag, δ, in Equation (2) [13, 16].

$$\varepsilon = \varepsilon_0 \sin(\omega t) \tag{1}$$

$$\sigma = \sigma_0 \sin(\omega t + \delta) \tag{2}$$

By expanding Equation (2), the stress is shown to consist of two components, where one component represents the magnitude, $\sigma_0 \cos(\delta)$, in phase with the strain and the other component is the magnitude, $\sigma_0 \sin(\delta)$, 90^o out of phase with the strain, as presented in Equation (3) [16].

$$\sigma = \sigma_0 \cos(\delta)\sin(\omega t) + \sigma_0 \sin(\delta)\cos(\omega t) \tag{3}$$

A sinusoidal stress-strain relationship for linear viscoelastic behavior can then be defined as stated in Equation (4), where G' and G" are the dynamic moduli, storage modulus and loss modulus, respectively, for a bulk material [16]. The storage and loss moduli are related, respectively, to the energy stored and dissipated during a loading cycle of a viscoelastic solid and are defined as shown in Equation (5) and Equation (6), respectively.

$$\sigma = \varepsilon_0 G' \sin(\omega t) + \varepsilon_0 G'' \cos(\omega t) \tag{4}$$

$$G' = \frac{\sigma_0}{\varepsilon_0} \cos(\delta) \tag{5}$$

$$G'' = \frac{\sigma_0}{\varepsilon_0} \sin(\delta) \tag{6}$$

These dynamic moduli values as well as the loss factor (tan δ) are important parameters which describe the linear viscoelastic behavior for a polymer system that can be determined from dynamic mechanical measurements conducted over a range of frequencies and temperatures. While the storage and loss moduli were defined above, the loss factor, synonymous with viscoelastic damping, is the ratio of the loss modulus to the storage modulus. The loss factor represents a measure of the internal friction produced by the movement of molecular chains from imposed deformation [16, 23, 24]. By implementing the time-temperature superposition principle (TTSP), it is possible to generate master curves of the dynamic moduli and loss factor, and obtain corresponding thermal shift factors, $a_T(T)$, which provide key insight into the relevant viscoelastic behavior of these material systems [13, 14].

Initially proposed in the 1940's, the TTSP is a common technique to determine the viscoelastic behavior of polymers at time or frequency scales that are not easily obtained experimentally such as long term behavior and relatively fast behavior of polymer systems [13, 25]. By performing tests on polymeric materials in instruments such as a DMA, it is possible to collect time or frequency data at various temperatures for a number of material properties that are rate and temperature dependent, and construct master curves at a specific reference temperature (T_{ref}). Sometimes this reference temperature is taken as the glass transition temperature (T_g) of a polymer, which is the long range segmental motions of polymer chains, in other cases a reference temperature corresponding to operating temperatures of a particular process is used. Therefore, the advantage of the TTSP is its ability to "trade" temperature for time by conducting mechanical tests of short durations over a range of relevant temperatures to determine modulus values, such as the dynamic moduli, relaxation modulus, and creep compliance, as a function of time or frequency over a significantly larger span than would be practical by other means [13]. For example, when constructing a master curve, temperatures below the selected reference temperature correspond to short times or high frequencies, whereas temperatures above the reference temperature relate to long times or low frequencies. The construction of these master curves provides significant insight as to how the various modulus values of a polymer behave with time and temperature over several viscoelastic behavior regions such as the glassy, leathery transition, and rubbery phases [13, 14].

These regions of viscoelastic behavior are illustrated in Figure 3-1. The glassy region corresponds to temperatures below a material's glass transition temperature in which the polymer will be "glass-like". Progressing to longer times, the polymer moves into a transition region in which the polymer possesses characteristics of leather. After the transition zone, the polymer takes on a rubbery behavior along the rubbery plateau, and for even longer times the polymer could experience a rubbery flow and liquid flow; however, thermosets, such as the semi-interpenetrating polymer network hydrogels discussed in this thesis, typically only exhibit the first three regions [13, 14], as crosslinks prevent flow.

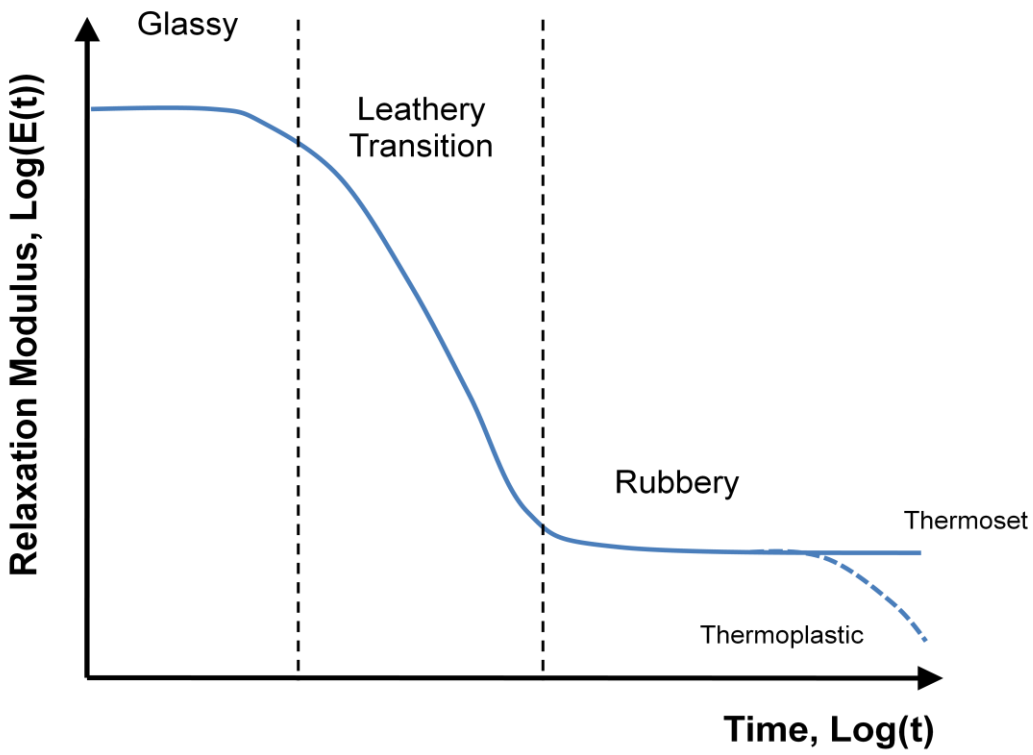

Figure 3-1: Diagram of the three main regions of viscoelastic behavior

In order to illustrate the construction and function of a master curve from data collected over a range of temperatures and several frequencies, Figure 3-2 is an example of the TTSP used to construct a master curve of the storage modulus of Hydrogel A at a reference temperature of 45^{o}C. In order to properly construct a storage modulus master curve, the unshifted data corresponding to temperatures below the 45^{o}C reference temperature were all shifted to the right, while the data at temperatures higher than reference temperature data were shifted to the left. Although details as to the observed behavior of Hydrogel A will not be discussed in this section, Figure 3-2 is an excellent illustration of the three main regions of viscoelastic behavior discussed above and presented in Figure 3-1.

In the construction of these master curves, the data which corresponds to each set of temperatures are shifted by individual thermal shift factor values, $a_T(T)$. Typically, these values are determined experimentally and rest on the assumption that all relaxation times (τ) of a homogeneous polymer are affected by temperature in a similar manner as shown in Equation 7, which is based on theories provided by Rouse and Zimm for dilute solutions of polymers above the glass transition temperature [13]. In this equation the thermal shift factor is shown to be a ratio of the relaxation times at one temperature, T, to that at a reference temperature, T_{ref}, which is shown to equal a constant consisting of a ratio of the viscosities, η, for a dilute solution of the polymer at the two temperatures

multiplied by a ratio of the densities, ρ, and temperatures. Assuming the temperature dependence of the relaxation time is the same for all polymer segments, this ratio of the relaxation times can be taken to the level of a molecule moving through a medium of the bulk polymer resulting in the ratio equaling the thermal shift factor. Therefore, the relaxation times of the polymer at a given temperature can be determined from that at another temperature by multiplying each relaxation time by the shift factor as demonstrated for the shifting of the storage modulus data in Figure 3-2 [13].

$$a_T(T) = \frac{\tau(T)}{\tau(T_{ref})} = \frac{\eta(T)}{\eta(T_{ref})}\left(\frac{\rho_{ref} T_{ref}}{\rho T}\right) \tag{7}$$

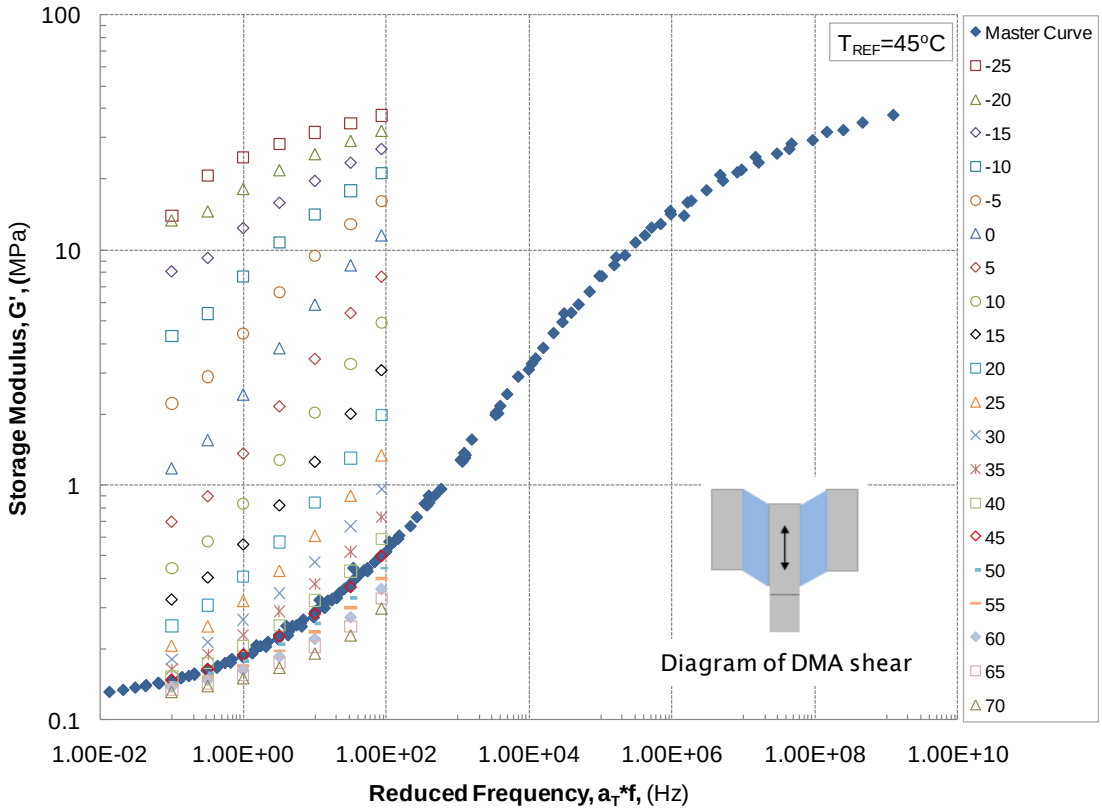

Figure 3-2: Example of master curve formulation using TTSP (Hydrogel A)

Generally, thermal shift factors can be applied to frequency or time values to provide horizontal shifts of the corresponding modulus data in order to generate master curves. Various dynamic mechanical analyzers come equipped with software designed to generate master curves with optimal shift factors; however, determination of shift factors are often performed manually by aligning data from different temperature levels to data of a predetermined reference temperature, typically a material's glass transition

temperature [13, 14]. Generally, the TTSP is considered valid for temperatures below this T_g of a polymer despite being based on the kinetic theory of polymers which is restricted to only temperatures above T_g [13]. The exact limit as to how far below a material's T_g the TTSP will work remains unclear; however, the TTSP is regarded as usable as long as data can be shifted into a smooth master curve [13].

These thermal shift factors can be plotted with their corresponding temperatures and fitted with several different equations; however, the Williams-Landel-Ferry (WLF) equation, presented below in Equation (8), can be useful above the glass transition temperature for many polymers [13, 14, 23]. Although the WLF equation is often used with the so-called universal constants, C_1=17.44 and C_2=51.6, which may be applicable for a wide range of polymers at a reference temperature equal to the material's T_g, there are cases where these values are material dependent due to differences in free volume, which is considered the volume within a polymer that is unoccupied by molecular mass, unusual conformations, and expansion coefficients [23, 26]. This equation generally provides an adequate fit of experimentally obtained thermal shift factor values for amorphous polymers above the material's T_g; however, the WLF equation is shown to deviate below a polymer's T_g because it underestimates the mobility of the molecular chains and fails to account for the excess free volume and increased entropy [27, 28]. Below T_g the polymer is in a non-equilibrium state in which the molecules do not have sufficient mobility to reach the predicted WLF state unless aging times are sufficient. Physical aging of polymer systems can reduce free volume and polymer chain mobility which ultimately results in experimental data approaching the WLF expression even below the material's glass transition temperature [13, 14, 23].

$$\log\left(a_T\right) = \frac{-C_1\left(T - T_{ref}\right)}{C_2 + \left(T - T_{ref}\right)} \tag{8}$$

This phenomenon is graphically depicted in Figure 3-3, where the top diagram suggests that free volume decreases with a decrease in temperature at a given slope representing the free volume expansion coefficient, α_f, until the material's T_g is reached. As the temperature approaches the polymer's T_g a deviation between the experimental data (dotted red line) and the WLF prediction (solid blue line) is shown, where the WLF equation has a greater decrease in free volume with temperature. Since more free volume allows polymer chains to be more mobile, there is an underestimation of the actual molecular chain mobility by the WLF equation since it depicts a greater decrease in free volume than the experimental results. Additionally, the lower graph in Figure 3-3 also presents this deviation between the experimental results and WLF fit at the same temperature shown in the top diagram, resulting in an overestimate of the thermal shift factors by the WLF equation. In this region, the experimentally determined shift factors are shown to be less sensitive to temperature, which corresponds to the decrease in

slope associated with the top graph of free volume versus temperature after the temperature goes below the material's T_g. Here, free volume decreases at a slower rate with decreases in temperature.

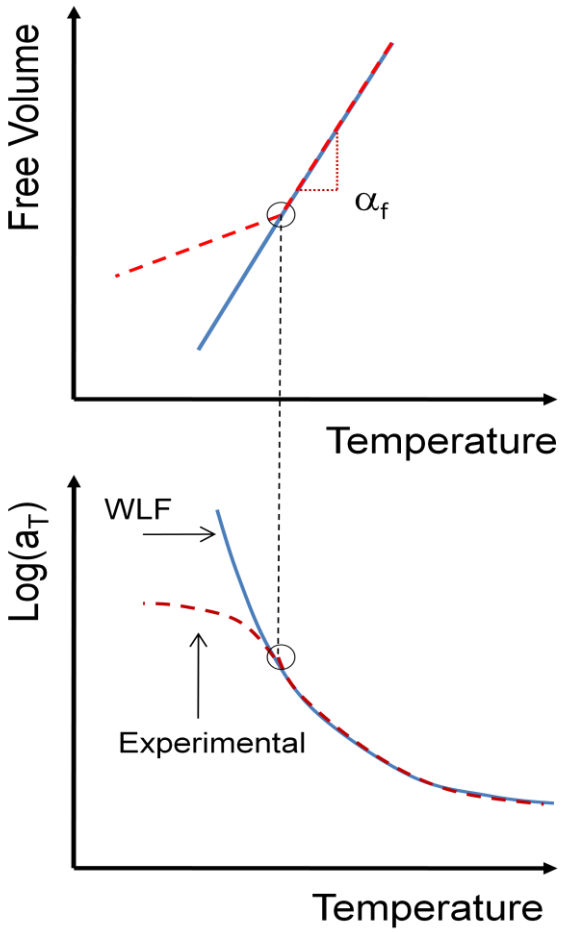

Figure 3-3: Graphical depiction of WLF underestimating polymer chain mobility with temperature

Mathematical representations of experimental data such as these constructed dynamic moduli master curves or other constitutive properties such as relaxation modulus or creep compliance can be obtained with exponential series formulations called Prony series. While a single Maxwell or Kelvin element can be used as mechanical analogs to crudely represent the time dependent response of polymers over narrow time scales, a Prony series can be formulated to provide a more realistic and accurate model of a polymer's stress-strain behavior by combining a series of these elements in different configurations. A generalized Maxwell model, which consists of several Maxwell elements in parallel, is an example of this exponential expansion that has been used to adequately model viscoelastic behavior of a material system by reducing it into a series of characteristic time values (τ_i) with corresponding moduli (G_i) [13, 14]. For the case of frequency-dependent dynamic moduli from DMA shear testing, the storage modulus,

G’(ω), and loss modulus, G”(ω), of each systems can be represented by the Prony series fit provided in Equation (9) and Equation (10), respectively [2, 14]. The characteristic time values and corresponding material coefficients for establishing a Prony series fit presented in these equations can be included in finite element models to provide time-dependent material properties for desired applications or simulations. Additionally, there are a number of interconversion relationships which can be used with developed Prony series fits of dynamic moduli master curves in order to approximate relaxation modulus or creep compliance curves as a function of time as shown in Equation (11), where t is approximately 1/ω. Interconversion relationships such as that used to approximate the shear relaxation modulus presented in Equation (11) can provide test data of a desired modulus to represent the material behavior in finite element modeling.

$$G'(\omega) = G_{\infty} + \sum \frac{G_i \omega^2 \tau_i^2}{\left(1 + \omega^2 \tau_i^2\right)} \tag{9}$$

$$G''(\omega) = \sum \frac{G_i \omega \tau_i}{\left(1 + \omega^2 \tau_i^2\right)} \tag{10}$$

$$G(t) \approx G'(\omega) - 0.4G''(0.4\omega) + 0.14G''(10\omega) \tag{11}$$

While it is important to characterize and model the small strain viscoelastic behavior achieved through rheological testing methods or DMA, it is equally imperative to study the large strain behavior of soft material systems, such as hydrogels, in order to fully understand the material’s mechanical behavior. Large scale strain behavior of soft or elastomeric materials can be characterized by a number of different test methods; however, uniaxial tension and compression methods are the most common and are often performed at various strain rates and temperatures to fully characterize soft material systems. While performing these types of tests over a range of temperatures and rates may require more resources and time compared to the techniques used to characterize the small strain viscoelastic behavior, these tests provide key insights into the material’s strength and toughness as well as the elastic modulus or Young’s modulus, which is a measured value of an isotropic material’s stiffness or resistance to deformation, as a function of rate and temperature [16]. Also, several researchers have had success in performing large deformation hysteresis testing on semi-interpenetrating polymer network (S-IPN) and double network (DN) hydrogel systems by systematically loading and unloading samples, in uniaxial tension and compression, in order to characterize dissipative energy attributed to fracture of covalent bonds in the hydrogel networks [11]. Currently, uniaxial compression testing of swollen hydrogel material systems has become the method of choice for many researchers, such as Shull and

Creton, who are investigating the material behavior of novel hydrogel systems [1, 11]. While this compression method works well for some hydrogel systems in their swollen state due to issues with gripping samples for tensile testing and its applicability to several areas of clinical use, it has recently been shown that results from tensile testing of some hydrogel systems can be notably different from compressive and shear testing results [11, 29]. Webber *et al*. suggests the differing results from these methods are due to alterations of the network structures during deformation for various hydrogel systems, especially double network hydrogels [11]. Additionally, analysis of the mechanics behind the compression of soft or elastomeric materials has shown many complexities and uncertainties with boundary conditions which result in errors in the analysis of compression testing [30]. Furthermore, a characterization of the large scale tensile deformation of certain hydrogel systems could provide insight into the design of hydrogel tissue scaffolds for skeletal muscle and tendons or even other biological tissues in which tensile material properties are important [29, 31].

Tensile testing of material systems is usually performed at a constant displacement rate until the sample fails while simultaneously measuring the load on a material system. This method is commonly used for experimentally determining mechanical properties such as elastic modulus (E), strain at break, ultimate strength, and toughness of swollen hydrogel systems [2]. Typically, Hooke's law, $\sigma = E\varepsilon$, is used to estimate the elastic modulus of materials by calculating the slope of the linear region at low strains, ε, from tensile stress-strain data. Although Hooke's law is adequate for linear elastic materials, it fails for materials with rubber network systems such as elastomers and hydrogels that typically exhibit a nonlinear stress-strain behavior at large strains [18, 32]. Since elastomeric materials are highly extensible, they require additional treatments provide by alternative constitutive relationships to characterize the elastic modulus and model the stress-strain behavior due to a geometric non-linearity relating to the change in cross-sectional area of materials during tensile testing for which Hooke's law does not account.

When performing uniaxial tension tests, there are numerous constitutive relationships which can be used to determine the elastic modulus and model the stress-strain behavior of an elastomeric material, such as the Neo-Hookean, Mooney-Rivlin, and Ogden models [18]. These models are based heavily on rubber elasticity concepts involving equilibrium thermodynamics and most hydrogel systems meet the criteria for normal rubbers which are lightly cross-linked polymer networks that rapidly respond to imposed stresses by rearranging polymer segments [2, 11, 29]. Although the Mooney-Rivlin and Ogden models for nonlinear stress-strain behavior fit the hyperelastic behavior of hydrogel materials, a simple Neo-Hookean method can be implemented to characterize up to the moderate strain region (50%-80%) as shown by the research of Crosby *et al.* on photo-crosslinked hydrogels [18]. However, it is important to note that

this Neo-Hookean model does not capture the high strain non-linear behavior of elastomeric materials as shown in Figure 3-4 [16, 18, 32].

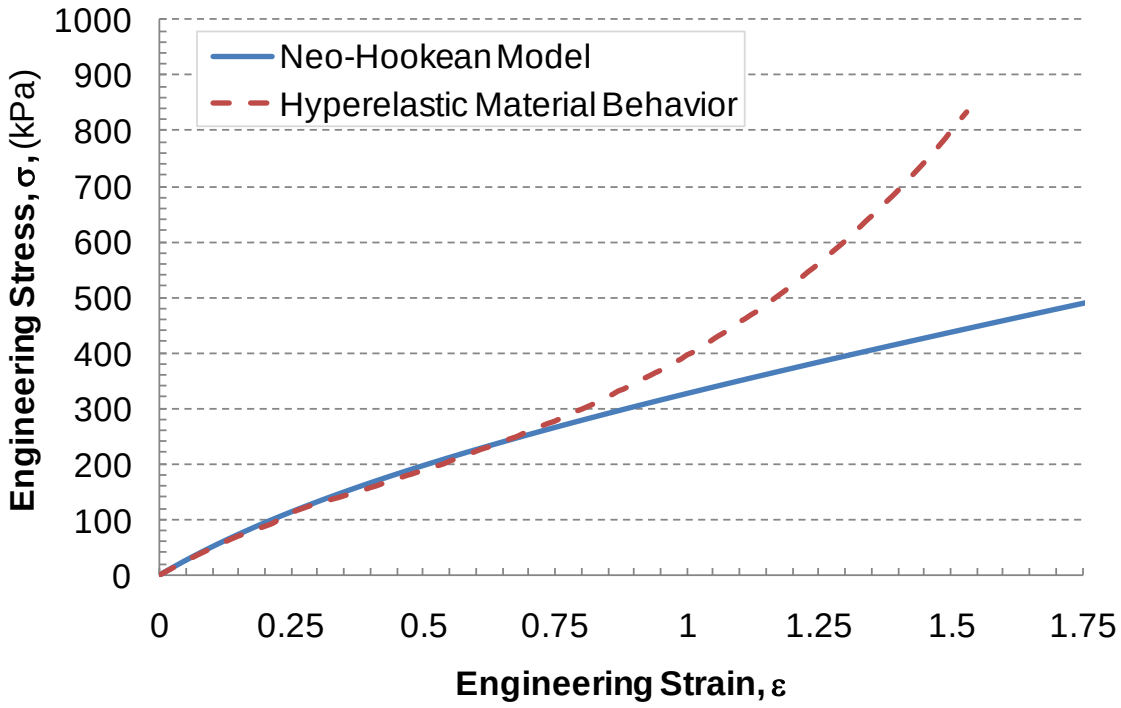

Figure 3-4: Comparison of hyperelastic material behavior and Neo-Hookean model

While details on the formulation of the Neo-Hookean model are shown below, Equation (12) represents the Neo-Hookean model which is simply the material's shear modulus, G, multiplied by the Neo-Hookean strain or deformation metric, $\lambda - 1/\lambda^2$, where λ is the extension ratio, $\lambda=1+\varepsilon$, and ε is the engineering strain [16]. This strain metric takes into account the reduction in cross-sectional area of the tested material sample which enables the Neo-Hookean model to provide a correlation of the stress-strain data for hyperelastic materials up to moderate strains of 80% in some cases; however, this hyperelastic model breaks down at higher strains because it fails to account for the stiffening of the material at large strains as shown in Figure 3-4 [32]. By plotting this strain metric against experimentally obtained stress data, a linear fit of this curve up to Neo-Hookean strain metric value of 1.25, which corresponds to an engineering strain of approximately 65%, is used to determine the shear modulus of the material system as displayed in Figure 3-5.

$$\sigma = G\left(\lambda - 1/\lambda^2\right) \tag{12}$$

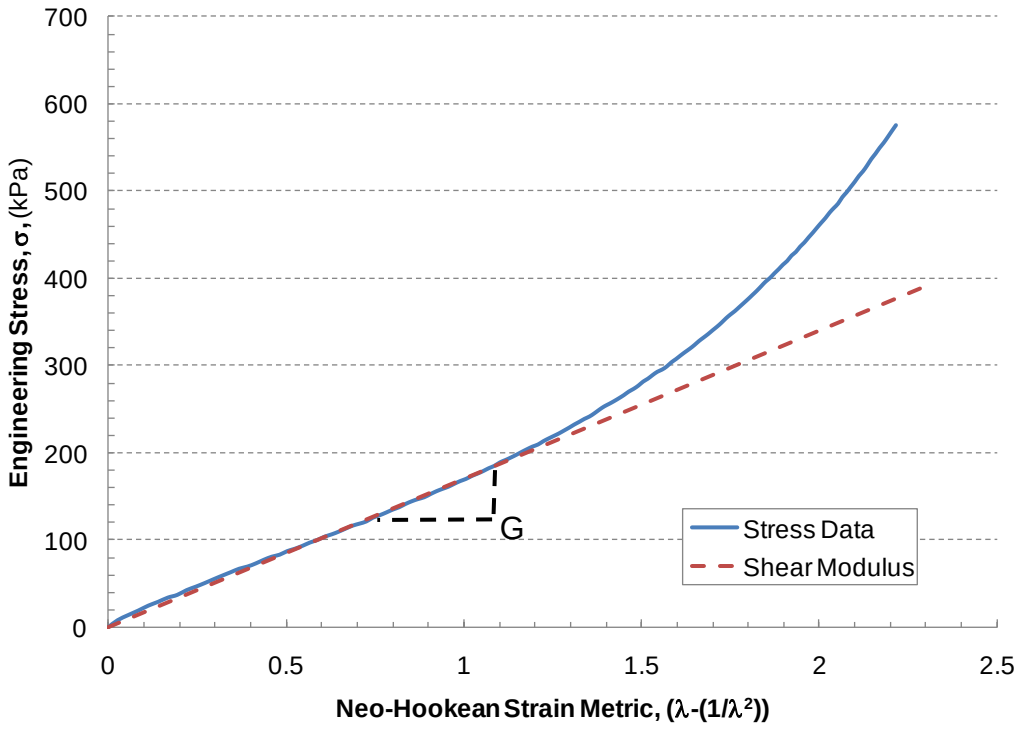

Figure 3-5: Example of Neo-Hookean strain metric used to approximate shear modulus

The kinetic or statistical theory of rubber elasticity, which is based on the molecular chains of an unstrained polymer adopting configurations resulting in a maximum state of entropy that decreases as forces are applied and the chains extend in the direction of the imposed force, is used to develop this Neo-Hookean stress-strain relationship [16, 32]. Equating the entropy change for all chains of the network, ΔS, determined by the statistical theory, to Helmholtz free energy, ΔA, with no change in internal energy on deformation and assuming the strain energy (U) function in the undeformed state is zero, a relationship between Helmholtz free energy and the strain energy function is presented in Equation (13).

$$\Delta A = -T\Delta S = \frac{1}{2} NkT\left(\left(\lambda_1^2 + \lambda_2^2 + \lambda_3^2\right) - 3\right) \tag{13}$$

In this equation, *N* is the number of chains per unit volume in the network, *k* is Boltzmann's constant, *T* is absolute temperature, and λ is the extension ratio , $\lambda=1+\varepsilon$, in the respective directions. The assumption of incompressibility is then applied to Equation (13), where $\lambda_1\lambda_2\lambda_3=1$ since Poisson's ratio, ν, of an elastomer is assumed to be ½. This results in $\lambda_2 = \lambda_3 = \lambda^{-1/2}$, as depicted in Figure 3-6 for the case of uniaxial tension, and thus changing Equation (13) into Equation (14) [16].

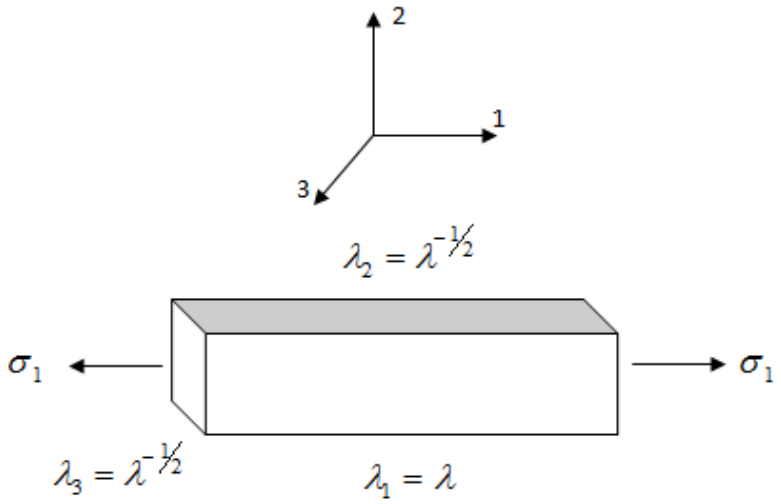

Figure 3-6: Hyperelastic material diagram for case of uniaxial tension

$$U = \frac{1}{2} NkT\left(\lambda^2 + \frac{2}{\lambda} - 3 \right) \tag{14}$$

The Neo-Hookean model is then determined by taking the derivative in strain energy with respect to the extension ratio, as shown in Equation (15), where the quantity *NkT* is equivalent to the shear modulus, *G*, of the elastomeric material. This constitutive relationship presented in Equation (15) can be used to model the small to moderate stress-strain behavior and approximate the shear modulus of elastomeric materials such as solvated hydrogels which has been shown by Crosby *et al* [18].

$$\sigma = \frac{dU}{d\lambda} = NkT\left(\lambda - \frac{1}{\lambda^2} \right) = G\left(\lambda - \frac{1}{\lambda^2} \right) \tag{15}$$

Equation (16) can then be used to calculate the elastic modulus, E, of the material by implementing the assumption of incompressibility for elastomers previously stated to determine Equation (14). With this assumption, ν is approximated as 0.5 and Equation (16) can be used to show that the elastic modulus is defined as three times the calculated shear modulus, $E \equiv 3G$.

$$\frac{E}{2(1+\nu)} = G \tag{16}$$

Additionally, the stress-strain behavior of soft and elastomeric materials was extensively studied by an engineering researcher, Smith, who proposed a qualitative stress-strain at break envelope of elastomeric materials under uniaxial tension testing when evaluated

over a range of temperatures and strain rates as presented in Figure 3-7 [33]. These un-hydrated hydrogel materials are suspected of being in a region with high strains and low stress as found on the far bottom right side of the red envelope just before the outward bulge which signifies higher strains as the testing temperature decreases or the strain rate increases. This drop in strain at break is associated with a viscoelastic fracture process which results in lower breaking strains at slower rates and higher temperatures [33, 34].

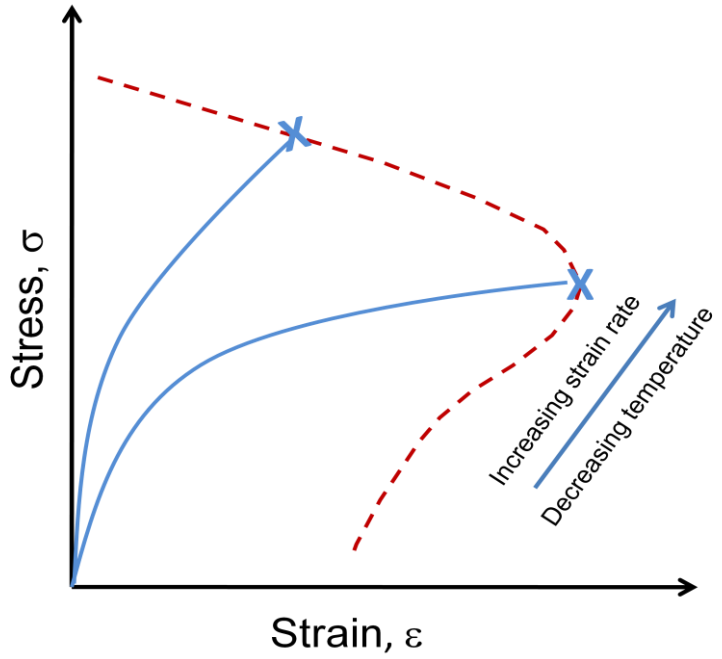

Figure 3-7: Stress-strain at break envelope for elastomeric materials

Characterization of the viscoelastic and hyperelastic behavior of hydrogels is critical to improve and control their material properties as well as advance manufacturing techniques and future applications. While DMA shear testing has shown to be successful in determining the small scale viscoelastic behavior, both compressive and tensile testing methods have proven useful in characterizing the bulk large scale strain or hyperelastic properties of hydrogels. However, due to the complex polymer networks in some hydrogel systems there are shown to be differences between properties determined by compressive and tensile methods resulting from alterations to the network structures due to varying levels of imposed strains on hydrogel systems as discussed by Webber *et al* [11] . This chapter discusses the details of the experimental methods and results from DMA shear and uniaxial tension tests performed over a range of temperatures and rates in order to characterize and compare the small scale viscoelastic and large scale hyperelastic behavior of two solvated semi-interpenetrating polymer network silicone hydrogels, Hydrogel A and B.

Experimental Procedure

DMA Shear Sandwich Testing

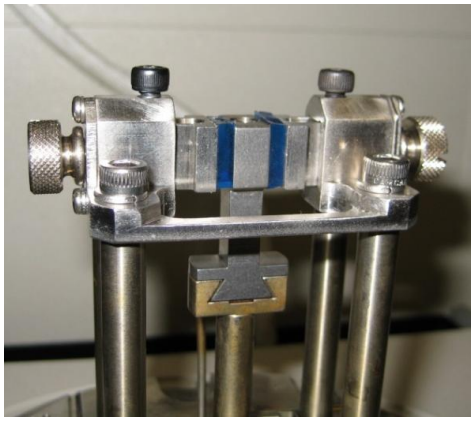

Figure 3-8: DMA shear setup with Hydrogel A

The small strain viscoelastic constitutive properties of Hydrogel A and B were obtained using a TA Instruments DMA 2980 operated in the multi-frequency strain mode while outfitted with shear sandwich clamps as presented in Figure 3-8. In order to provide confidence in the measurements from this instrument, three trials of each hydrogel system were performed in which each trial required two square samples of the desired hydrogel system with dimensions of approximately 10 mm x 10 mm x 2 mm. Bulk sheets of the desired hydrogel system were cured using the procedure outlined in Chapter 2, and then prepared and tested within one hour of curing the sample in order to reduce the effects of solvent loss that are presented in Appendix A. Also, accurate measurements of the uniform thickness of these soft hydrogel materials were obtained using a Mitoyoto® micrometer, presented in Figure 3-9. Each sample was placed between two rigid glass sheets of known thickness and complete wetting of the glass was used to verify uniform thickness. The tip of the Mitoyoto® micrometer was placed in contact with the top rigid glass layer as opposed to the soft and highly compliant hydrogel material, as depicted in Figure 3-10, in order to acquire an accurate thickness measurement.

Figure 3-9: Mitoyoto® Micrometer

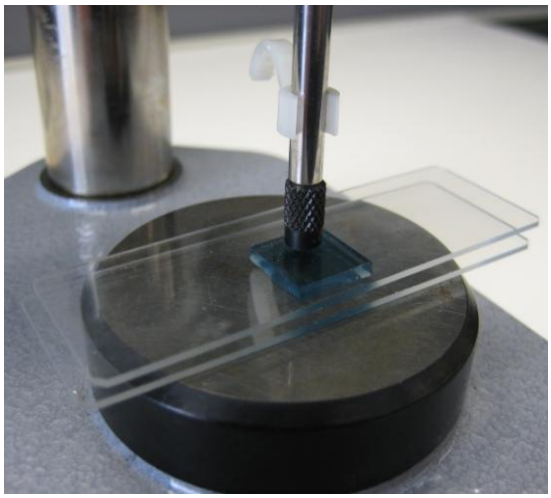

Figure 3-10: Close up of thickness measuring procedure

Each DMA trial was operated under the temperature step-frequency sweep mode which oscillated each sample at the specified set of frequencies for each temperature step

within a predetermined temperature range. Before initiating the test, samples were carefully placed and aligned between each set of square steel shear grips, as shown in Figure 3-8, using a set of tweezers in order to keep the samples uncontaminated and undamaged. Additionally, the samples were compressed sufficiently so that they were not over strained, but still would not slip during testing. For this experiment, a 5^{o}C temperature step was selected for a temperature range from -25^{o}C to 70^{o}C and the samples were exposed to seven frequencies spanning from 0.1 to 85 Hz. A 5 minute isothermal soak time was incorporated to provide enough time for the sample to equilibrate at each step and the amplitude was reduced to 10 μm in order to reduce the possibility of slippage due to high shear forces which occurred during prior tests with greater amplitudes. With this selected amplitude and provided material dimensions, an estimated 0.1% strain was imposed on these DMA shear sandwich samples. The dynamic moduli as well as tan δ were obtained for every tested frequency at each temperature step in order to construct master curves and Prony series fits of Hydrogel A and B which describes their small strain viscoelastic behavior.

Uniaxial Tension Testing

The large strain viscoelastic behavior and properties of these solvated hydrogel systems were also investigated, but obtained by uniaxial tension testing over a range of relevant temperatures and several different strain rates. Bulk sheets, approximately 12.7cm by 12.7cm, of the desired hydrogel system were cured as stated in Chapter 2, and then each sheet was removed from its polypropylene encasement and several dogbone uniaxial tension samples were punched using a standard ASTM # D 638-5-IMP punch die, shown in Figure 3-11, with a cutting press. Pressure sensitive adhesive tape (Scotch® Magic™ Tape ¾ ”) was placed on both sides and ends of the tabs of each sample, as shown in Figure 3-12, in order to prevent/reduce damage imposed by gripping the samples during testing. While the length and width of the samples were standardized, the thickness of each sample was measured with the Mitoyoto® micrometer as outlined above for the square DMA shear samples.

Figure 3-11: ASTM # D 638-5-IMP punch die

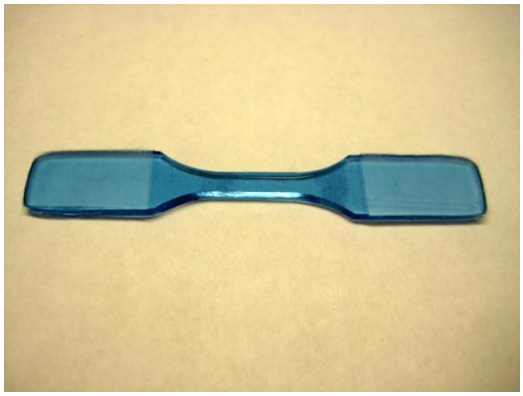

Figure 3-12: Punched and taped uniaxial tension sample (Hydrogel B)

Hydrogel A and B uniaxial tension samples were tested using a constant crosshead ramp to failure method on an Instron® MicroTester 5848 equipped with a 50 N load cell and custom-made environmental chamber displayed in Figure 3-13. Additional information as to the components and function of this environmental chamber can be found in Appendix C. Each material system was tested at several temperatures ranging from -5^{o}C to 60^{o}C and three displacement rates at each temperature level; 0.1 mm/s, 1 mm/s, and 10 mm/s. Five samples were used at each strain rate; therefore, 15 samples were used for each temperature level tested. After the environmental chamber reached the desired testing temperature, samples were placed inside the chamber for 10 minutes prior to the first trial in order to allow the samples to equilibrate thermally. The possibility of solvent loss, especially for Hydrogel A at elevated temperatures, needs to be considered as shown in the solvent loss study in Appendix A. A thermocouple was placed near the sample to provide confidence in the desired temperature level. Samples were secured in pneumatic grips (Instron® 2712-019), which possessed a total surface area of 625 mm^2, set to an air pressure of 103 kPa in order to prevent slipping as well as eliminate or reduce damage imposed by gripping the samples during testing. Load, time, and crosshead displacement were recorded for each run; however, initial trials at 20^{o}C implemented the use of laser extensometry in order to determine an effective gauge length of the material to provide a more accurate strain measurement. In the end, this data was used to determine the effect of rate and temperature on the shear modulus as well as the stress and strain at break for this large scale viscoelastic behavior.

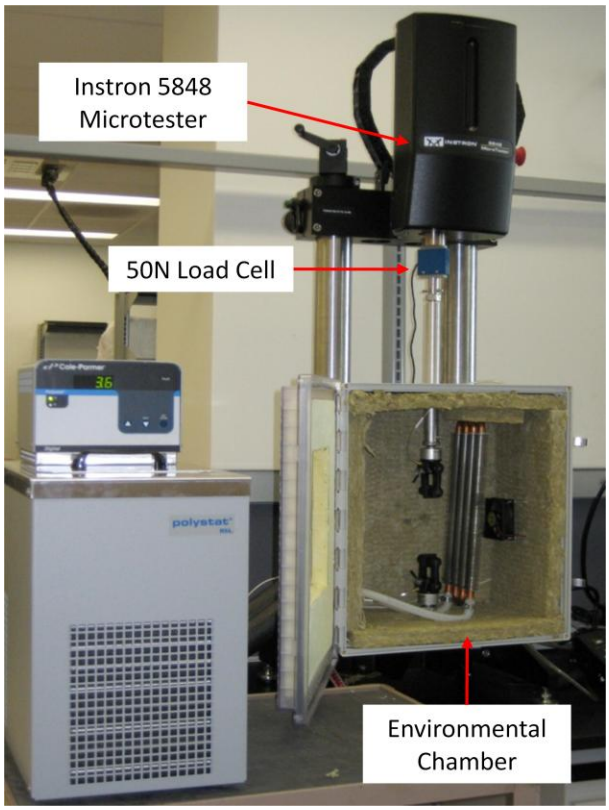

Figure 3-13: Uniaxial tension setup

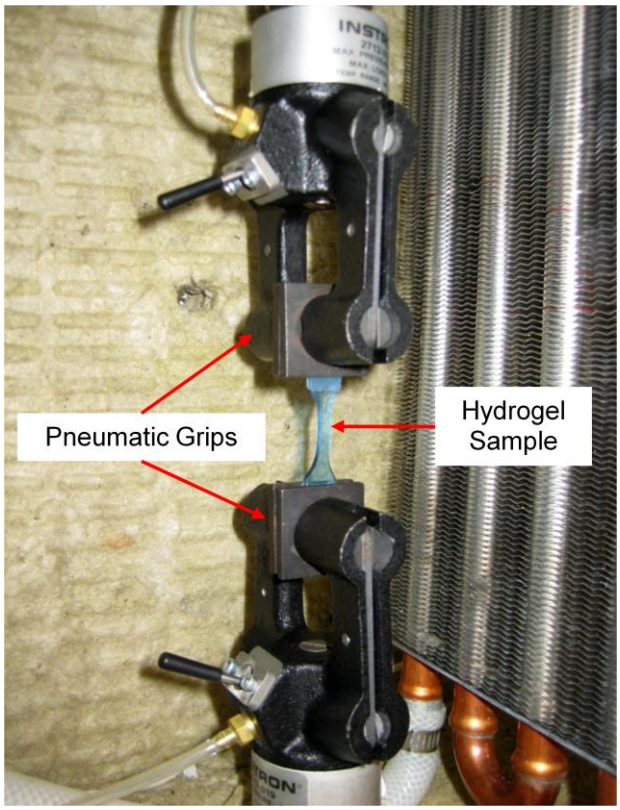

Figure 3-14: Close up of pneumatic grips and mounted hydrogel dogbone sample

Results and Discussion

DMA Shear Testing

Master curves of the dynamic moduli (G' and G") as well as the loss factor (tan δ) for both solvated hydrogel systems plotted against frequency in Hertz (f) instead of radians (ω), where $\omega=2\pi f$, were constructed by manually shifting data, independently from one another, to match at a reference temperature of 45^{o}C and are presented in Figure 3-15 through Figure 3-17, shown below. This reference temperature was selected because it matches the operating conditions at which the manufacturing of these hydrogel systems in their applied state occur. As these figures indicate, good repeatability was found for the three trials of each hydrogel system using the DMA shear sandwich clamps with this temperature-step frequency sweep method. Based on these results, Hydrogel A exhibits a greater storage and loss modulus compared to Hydrogel B by as much as a half to one order of magnitude in some regions, as shown in the storage, loss, and tan δ master curves presented in Figure 3-15 through Figure 3-17. The storage modulus master curve for Hydrogel B, displayed in Figure 3-15, shows a long term or equilibrium plateau which extends approximately two decades longer than the frequency level where Hydrogel A begins to show a transition from its equilibrium plateau. This further

emphasizes that Hydrogel B shows relatively little viscoelastic behavior in this particular temperature and time region, consistent with its equilibrium plateau and dissipates less energy when compared to Hydrogel A.

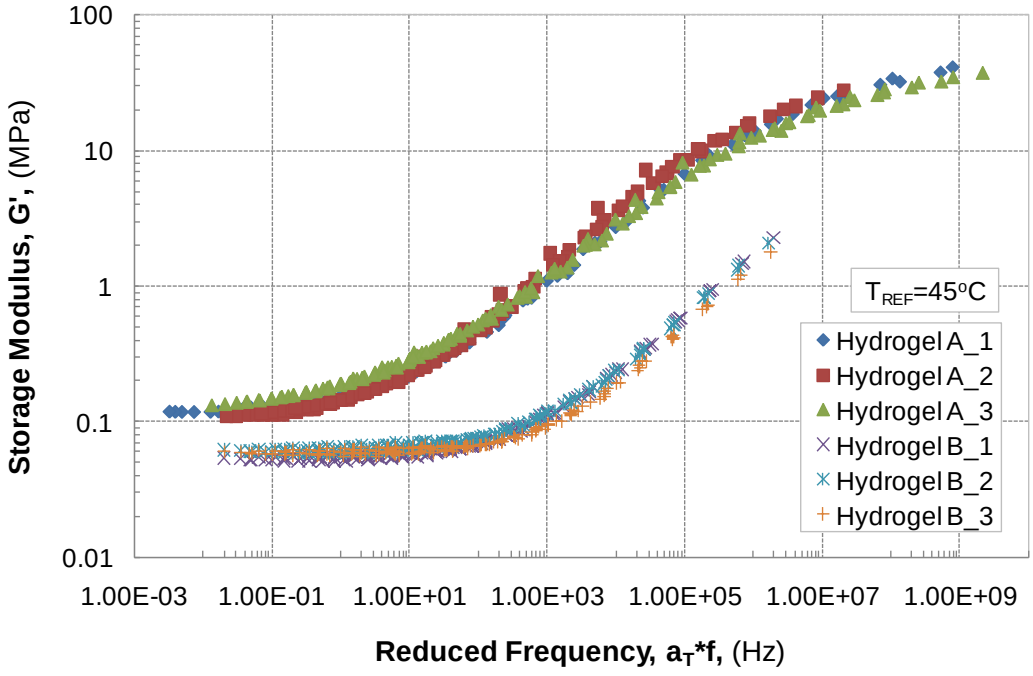

Figure 3-15: Master curves of storage moduli for Hydrogel A and B

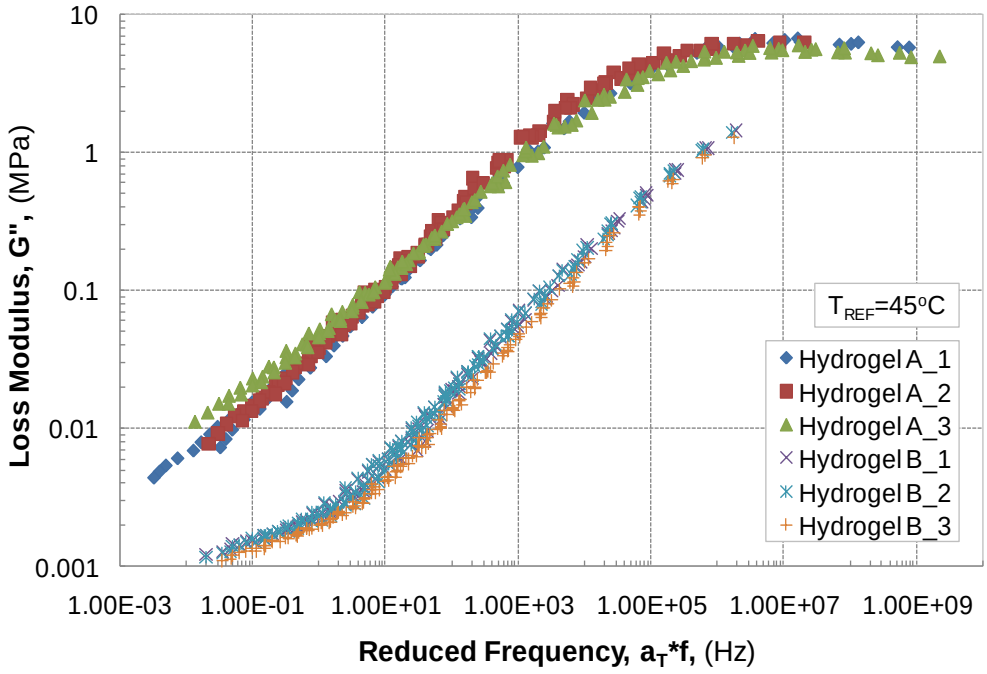

Figure 3-16: Master curves of loss moduli for Hydrogel A and B

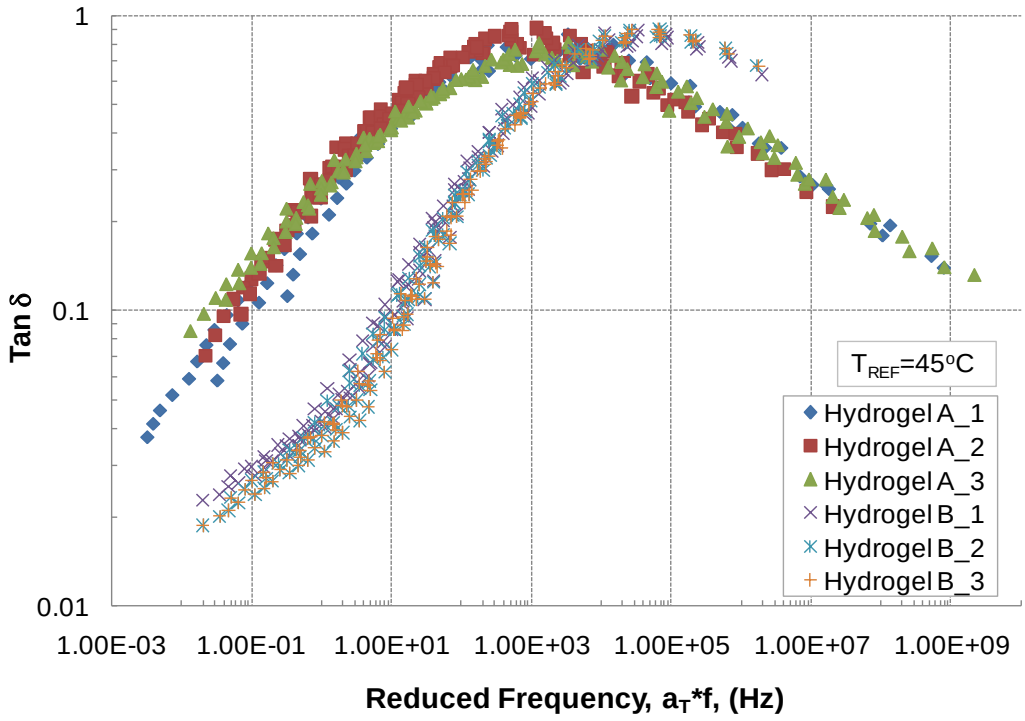

Figure 3-17: Master curves of the loss factor, tan δ, for Hydrogel A and B

The thermal shift factor plots for Hydrogel A and B with corresponding WLF fits are shown below in Figure 3-18. As previously mentioned and observed with the consistency of the master curves for both material systems, there is good agreement and repeatability between the three trials for each material system. The WLF constants, C_1 and C_2, used to apply the fits presented in Figure 3-18 of each material system were determined by averaging the constants for each trial and are presented in Table 3-1. With these WLF parameters, this graph depicts an excellent fit of the thermal shift factors for each hydrogel system using the WLF equation; however, the WLF fit for Hydrogel A begins to overestimate the experimentally determined thermal shift factors at temperatures below its glass transition temperature (T_g) of approximately -12°C. Below this temperature the polymer is in a non-equilibrium state and the amount of free volume is decreasing with temperature more slowly than for temperatures above the T_g. Therefore, the molecular chains do not have sufficient mobility to reach the predicted WLF state without sufficient aging times. This results in lower thermal shift values for experimental data at temperatures below the T_g compared with the WLF prediction [13, 14]. Lastly, this thermal shift factor plot provides evidence that the mechanical properties of Hydrogel A are more sensitive to changes in temperature compared to Hydrogel B for temperatures below 40°C. This sensitivity to changes in temperature is expected for Hydrogel A since it is moving out of the equilibrium plateau region, while Hydrogel B remains in the rubbery plateau to higher frequencies.

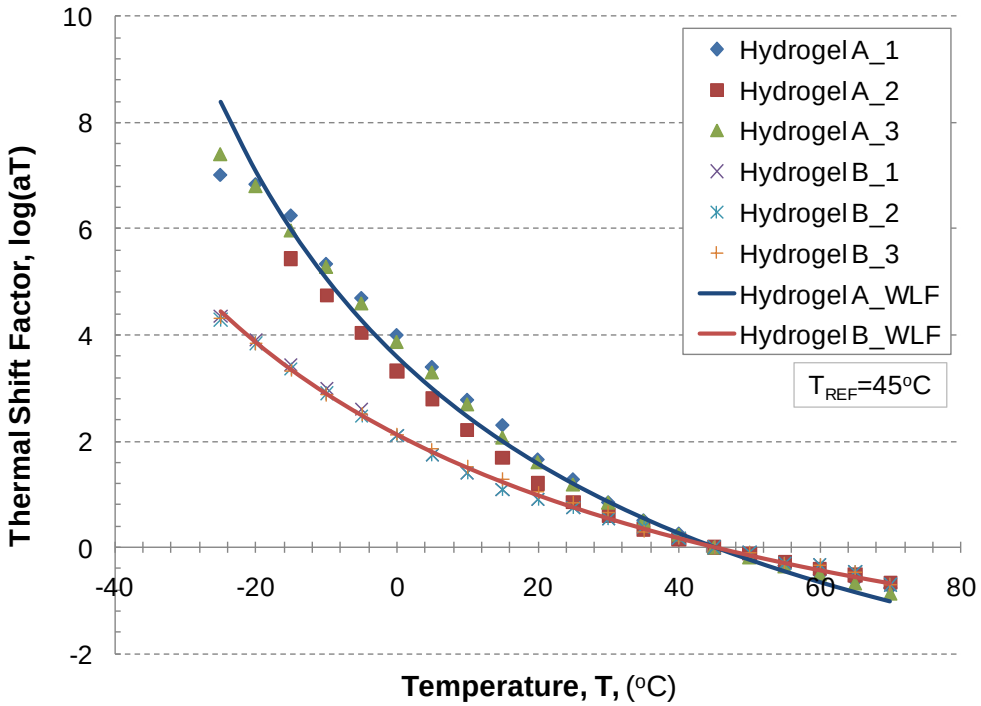

Figure 3-18: Thermal shift factor plot with WLF fits for Hydrogel A and B

Table 3-1: Summary of the WLF coefficients for Hydrogel A and B at T_{REF}=45°C

	Hydrogel A			Hydrogel B	
Trial	**C_1**	**C_2 (°C)**		**C_1**	**C_2 (°C)**
1	6.25	119.9		4.32	136.9
2	4.02	101.6		4.14	135.0
3	7.58	137.3		5.26	154.6
Average	5.95	119.6		4.57	142.2

Prony series fits of the dynamic moduli master curves for Hydrogel A and B are presented in Figure 3-19 and Figure 3-20. By preselecting approximately two characteristic time constants (τ_i) per decade and implementing an absolute sum difference optimization of the Prony series fit using the kernels for the storage and loss modulus provided in Equation (9) and Equation (10), respectively, excellent fits of the dynamic modulus master curves were obtained which can be integrated into numerical modeling applications to describe the time and temperature dependence of Hydrogel A and B.

The coefficients and characteristic time constants from the Prony series fits, found in Appendix B, were used to approximate a shear relaxation modulus, three approximations for each material system are displayed in Figure 3-21. As shown consistently with the storage and loss modulus master curves for both material systems, Hydrogel A has a greater shear relaxation modulus for all values of time presented in Figure 3-21 and Hydrogel B shows an equilibrium plateau which continues at least three orders of magnitude before Hydrogel A.

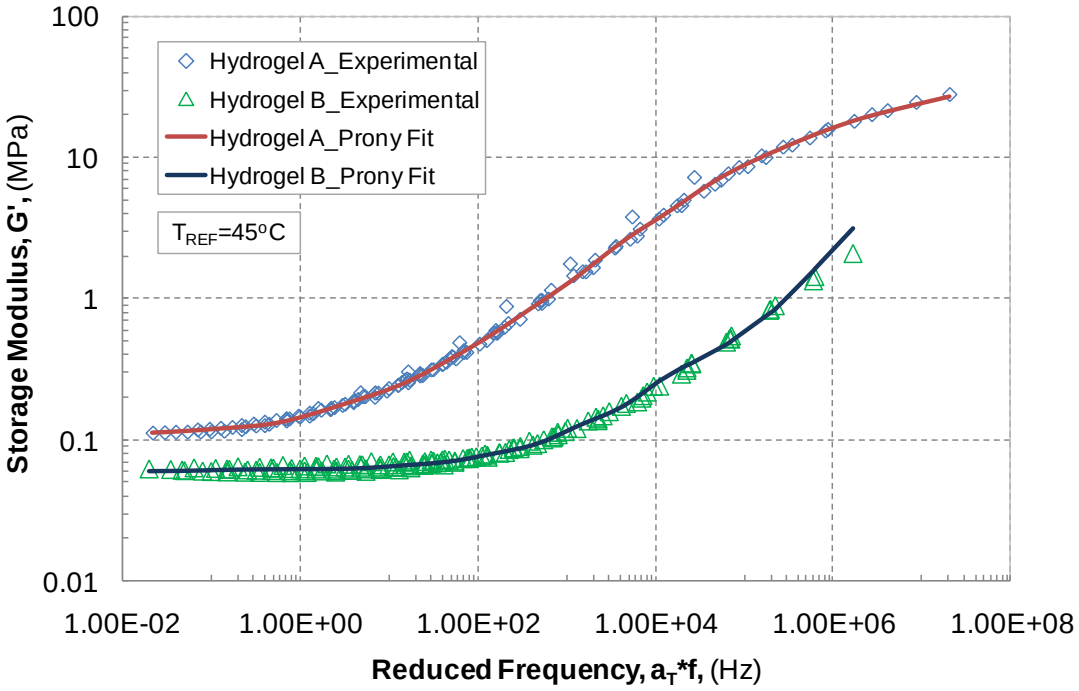

Figure 3-19: Prony series fits of the storage modulus master curves for Hydrogel A and B

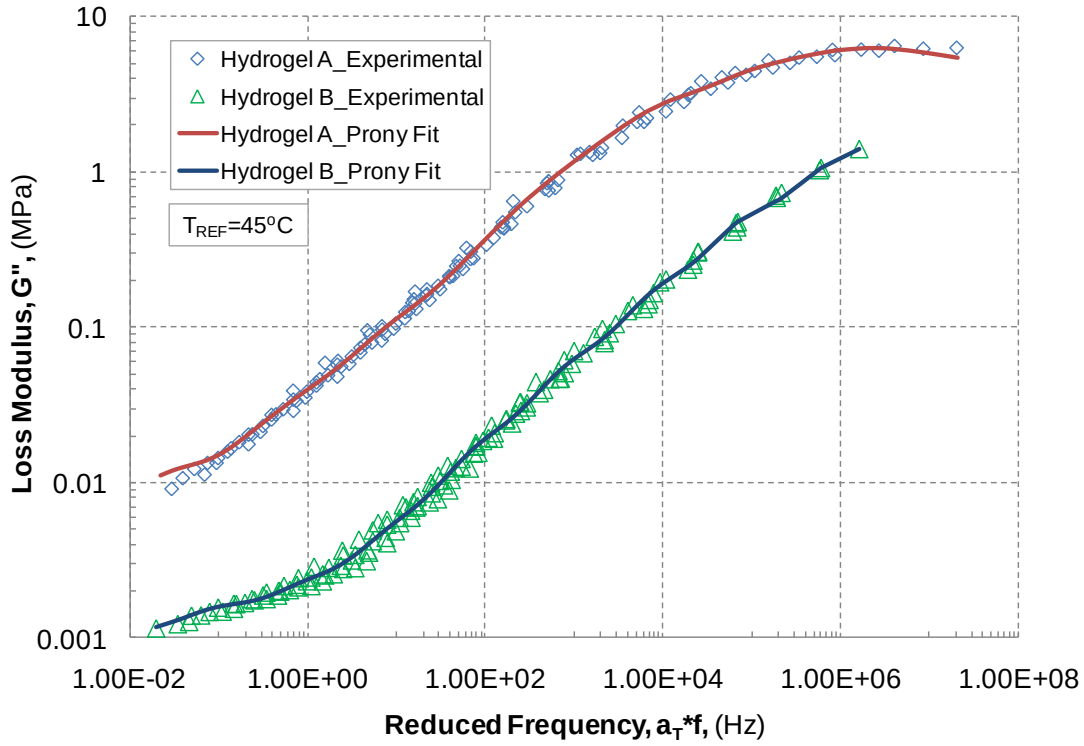

Figure 3-20: Prony series fits of loss modulus masters curves for Hydrogel A and B

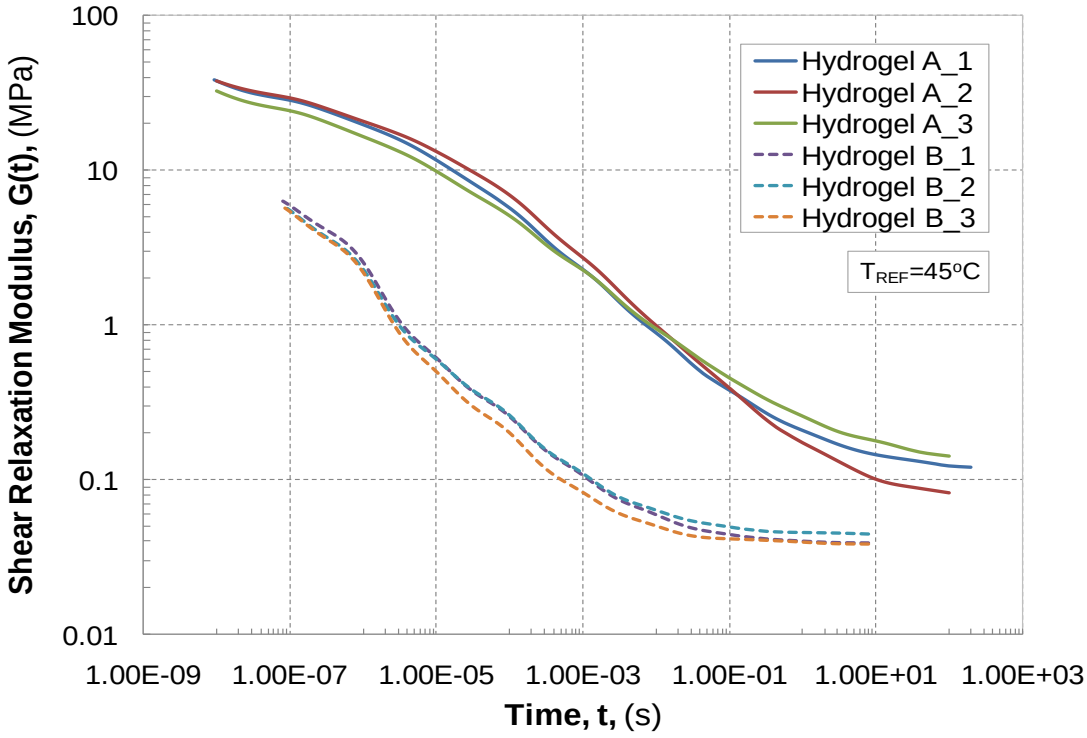

Figure 3-21: Approximation of shear relaxation modulus for Hydrogel A and B using Prony series fits and interconversion relationships

Uniaxial Tension Testing

Representative results of the acquired stress-strain curves at a temperature of 20^{o}C and a crosshead ramp rate of 10 mm/s for uniaxial tension testing of Hydrogel A and B are presented in Figure 3-22 and Figure 3-23 , respectively. While the stress-strain curves for both Hydrogel A and B depict nonlinear stress-strain behavior, especially at larger strains above 80%, Hydrogel B exhibits a lower mechanical stiffness based on the observed level of stress imposed on the system compared to Hydrogel A for similar levels of strain. Based on these representative stress-strain plots of the uniaxial tension data for Hydrogel A and B, relatively consistent behavior between trials for a particular temperature and rate was observed for both Hydrogel A and B. Possible causes for variation between trials could stem from slight variations in the curing of the monomer systems and effects of solvent loss especially at higher temperatures which would cause an increased rate of solvent egress. Additionally, representative plots displaying the effects of temperature on the stress-strain behavior of Hydrogel A and B at a crosshead ramp rate of 10 mm/s are presented in Figure 3-24 and Figure 3-25, respectively. The tested temperature range proved to have a greater effect on the stress-strain behavior of Hydrogel A compared to Hydrogel B, as shown qualitatively by the greater variation between the stress-strain curves at different temperature levels. This was also shown in the DMA shear results where Hydrogel B, for this given range of temperatures and rates, was on the equilibrium plateau, while Hydrogel A was in a transition region which results in its stress-strain behavior being sensitive to changes in temperature over the tested range as displayed in Figure 3-24. These results for the effects of temperature on the stress-strain behavior for Hydrogel A are also consistent with those of Smith’s stress and strain at break envelope for elastomeric materials, where an increase in temperature results in a decrease in stress and strain at break based on region along the stress-strain at break envelope [33].

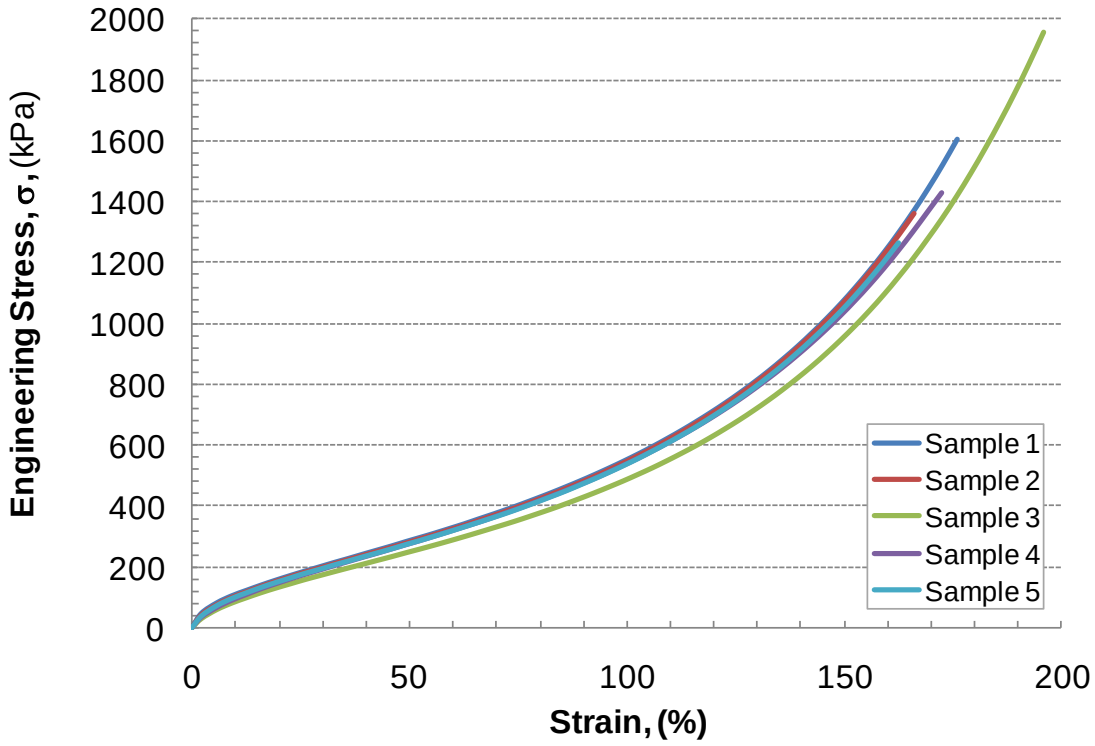

Figure 3-22: Stress-strain plot for Hydrogel A at 20°C and 10 mm/s ramp rate

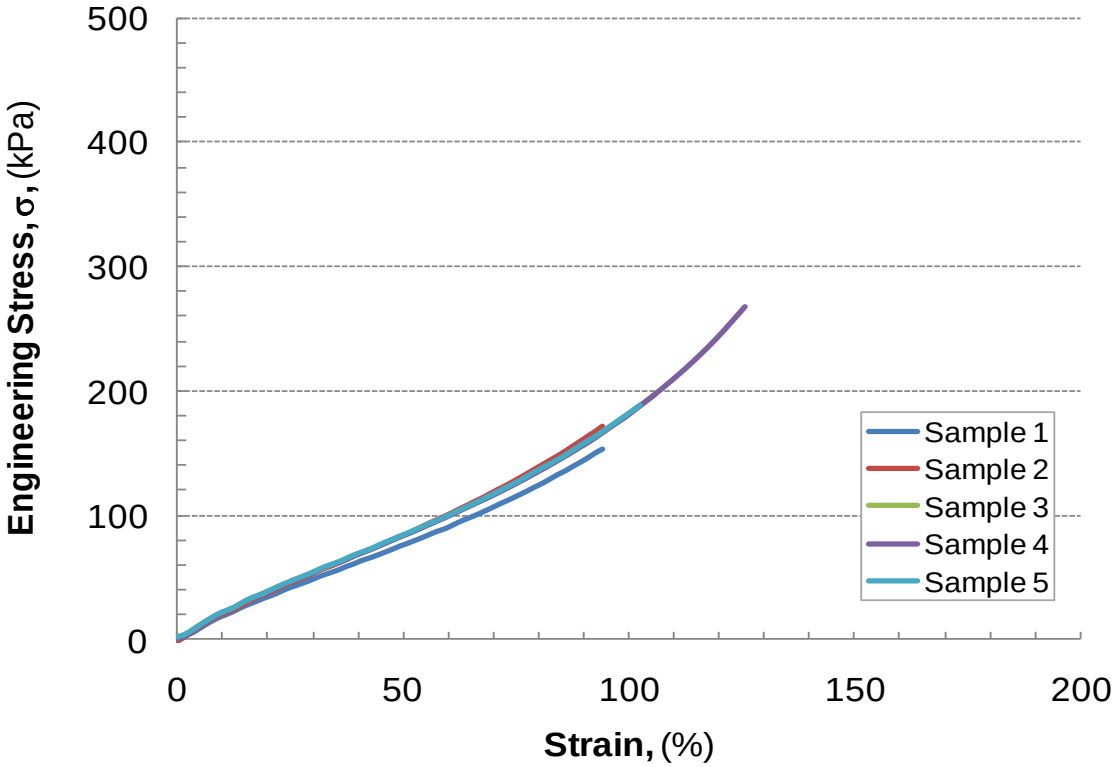

Figure 3-23: Stress-strain plot of Hydrogel B at 20°C and 10 mm/s ramp rate

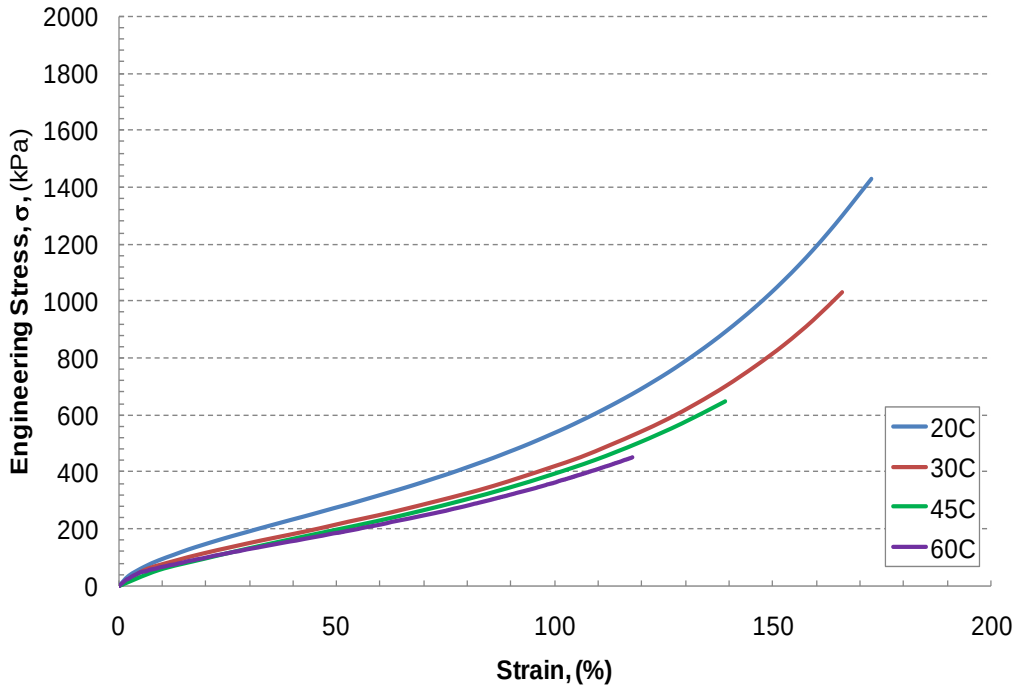

Figure 3-24: Effect of temperature on stress-strain curve for Hydrogel A at a 10 mm/s ramp rate

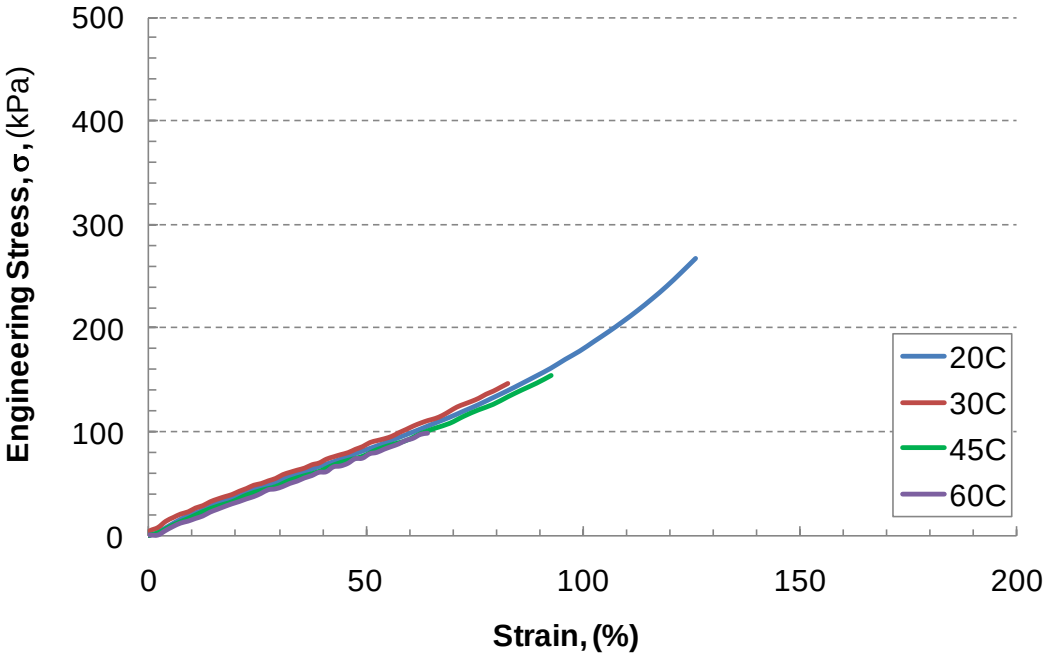

Figure 3-25: Effect of temperature on stress-strain curve for Hydrogel B at a 10 mm/s ramp rate

The stress and strain at break results from uniaxial tension tests of Hydrogel A and B in which samples were ramped at several different displacement rates over a range of temperatures are presented in the set of figures from Figure 3-26 to Figure 3-29. These

charts indicate that Hydrogel A possesses a greater mechanical strength based on the consistently higher stress and strain at break values determined for each set of rates and temperatures. Also, both hydrogel materials appear to be exhibiting the expected trends of increased stress at break with increasing strain rate and decreasing temperature as well as an increase in strain at break as strain rate increases which is not expected for most materials, but is consistent with research performed by Smith on elastomeric material systems [33, 34]. These results correlate with the molecular mobility of the polymer chains present in these hydrogel networks which suggests as the temperature decreases the molecular mobility decreases and chains become stiffer and locked into place thus increasing the stress at break. Additionally, higher stress values at break are recorded for higher displacement rates due to the fact that the polymer chains in these hydrogel systems have less time to relax and reorient compared to testing at slower rates. These results are also consistent with the findings of Smith based on his derived stress-strain at break envelope for elastomeric materials, depicted in Figure 3-7, where a decrease in temperature can result in an increase in strain as shown in Figure 3-26 for Hydrogel A at 0^{o}C [33, 34].

Further analysis of these plots indicate that there is a greater effect of rate and temperature on the stresses and strains at break at each temperature level for Hydrogel A than Hydrogel B over the tested temperature range and set of rates due to Hydrogel B being on the rubbery plateau for this tested region which is also reinforced by the storage modulus master curve constructed from the DMA shear results in Figure 3-15. This result signifies that despite changing the temperature and rate over the analyzed levels, there is relatively little change in viscoelastic behavior of Hydrogel B compared to Hydrogel A. However, once test temperatures are 0^{o}C or below and the 10mm/s crosshead rate is used there is a significant increase in the stress and strain at break for Hydrogel B while Hydrogel A exhibits a definite increasing trend for the stress and strain at break as temperatures decrease and strain rates increase.

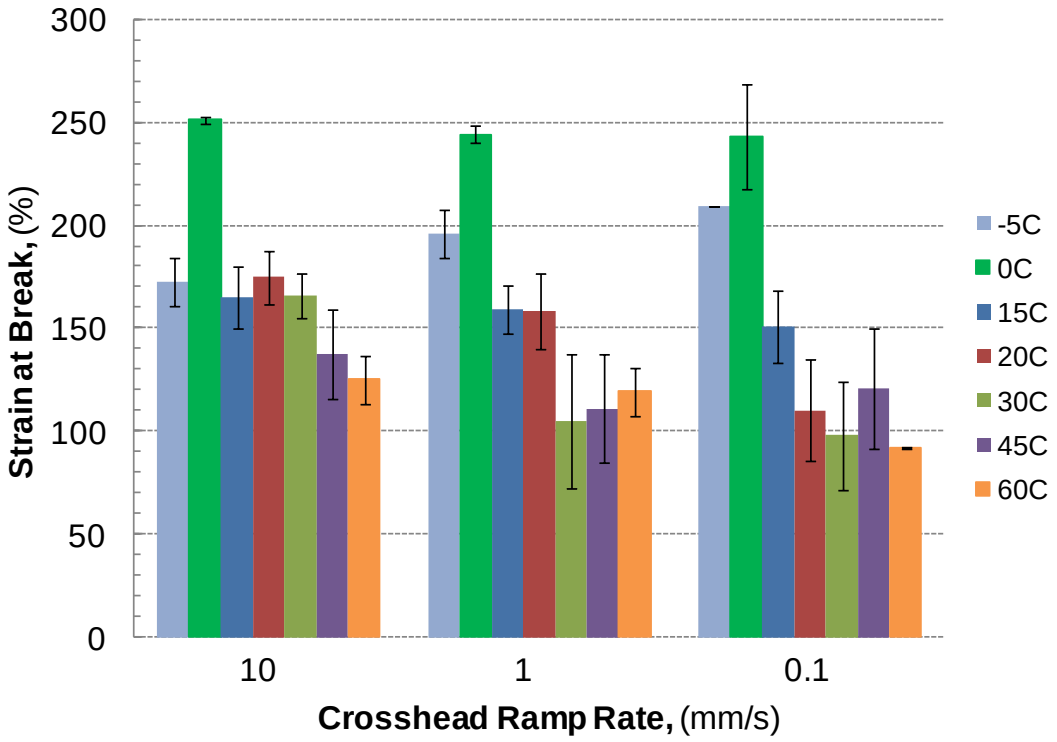

Figure 3-26: Average percent strain at break for Hydrogel A

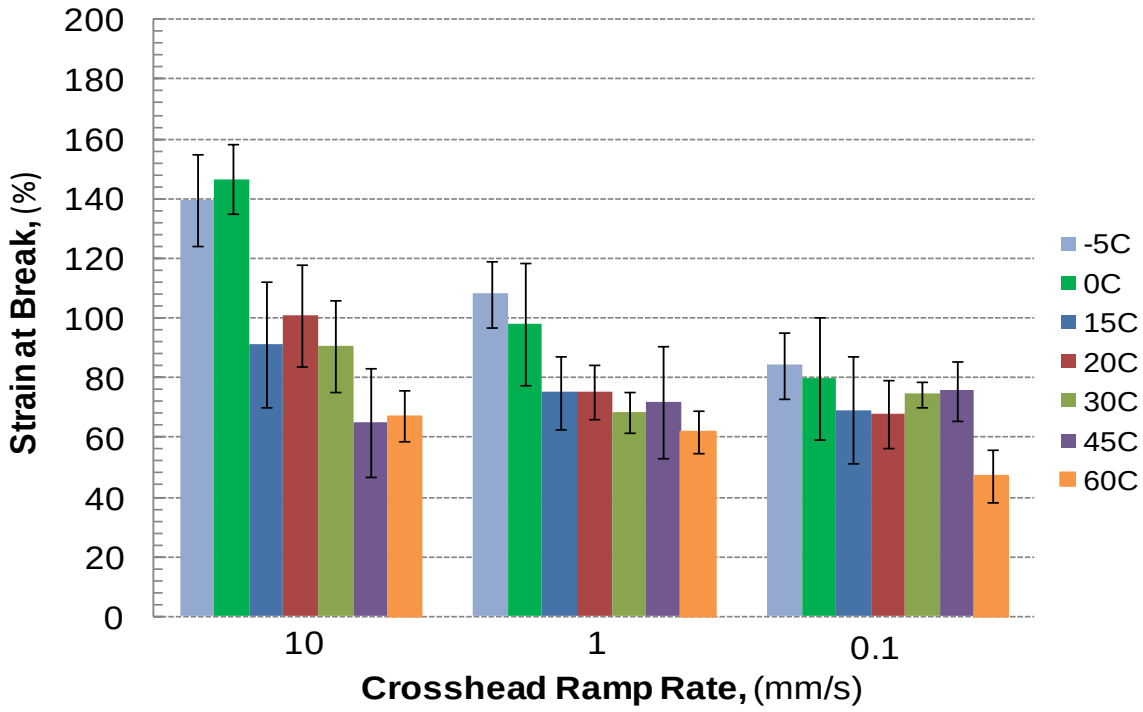

Figure 3-27: Average percent strain at break for Hydrogel B

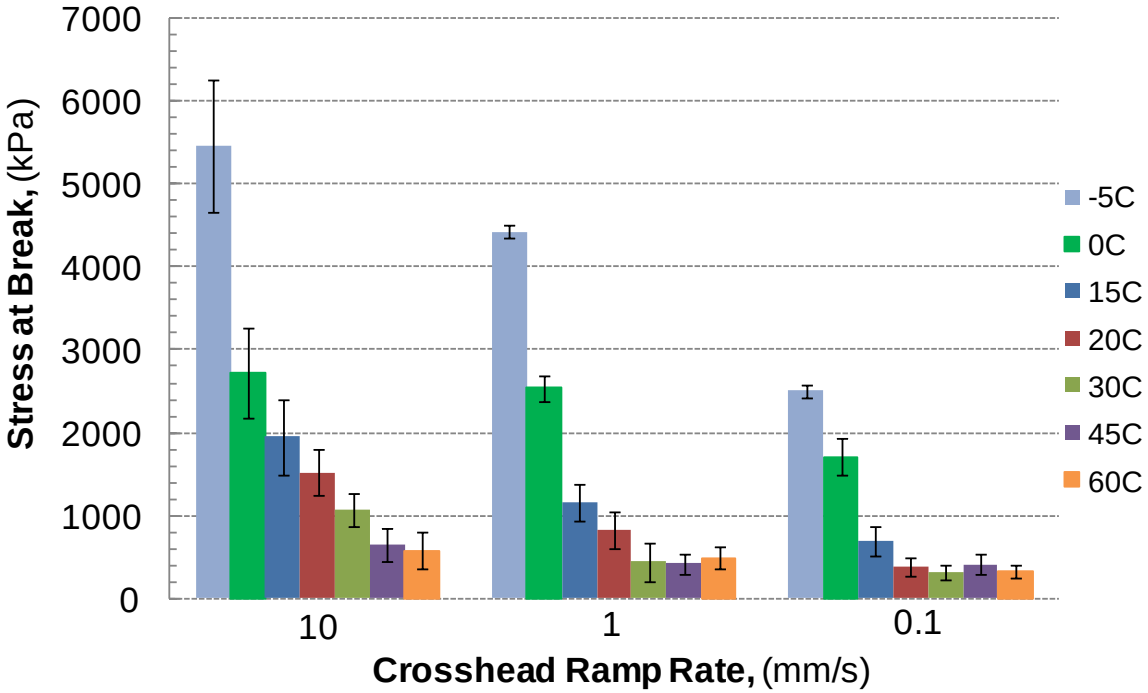

Figure 3-28: Average stress at break for Hydrogel A

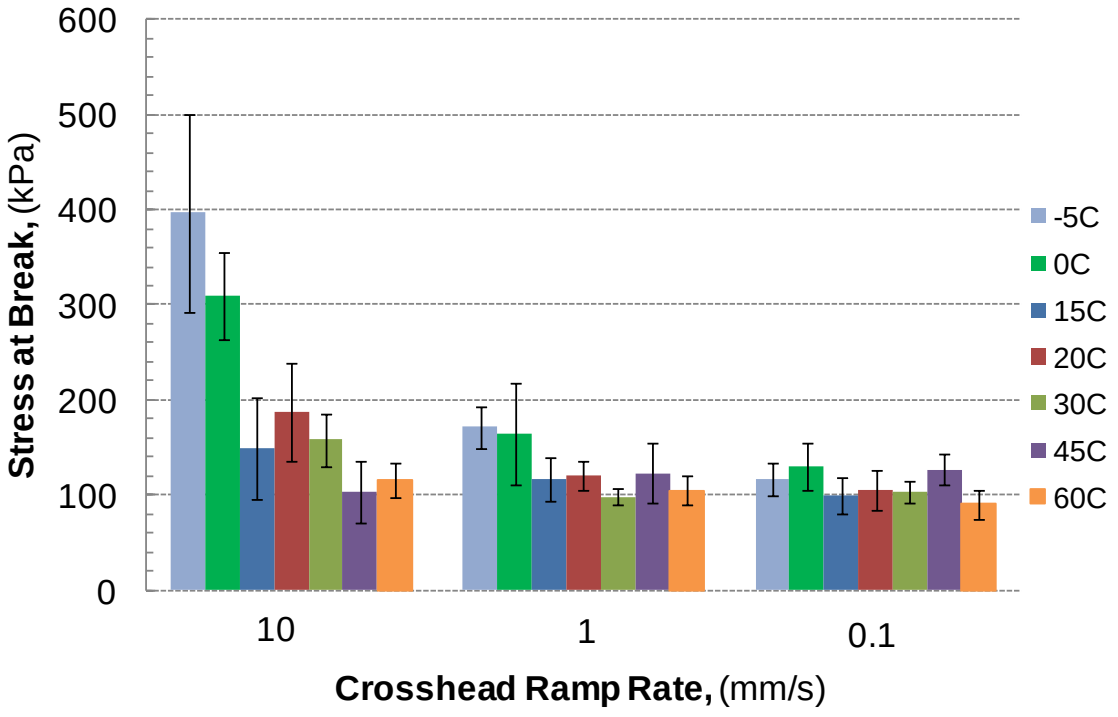

Figure 3-29: Average stress at break for Hydrogel B

Shear moduli values for Hydrogel A and B were also obtained from these uniaxial tension tests performed over a range of temperatures and several rates as shown in Figure 3-30 and Figure 3-31, respectively. As previously stated, a similar trend of Hydrogel B, shown in Figure 3-31, exhibiting little to no change in modulus with changes to temperature and rate, especially for the ranges temperature and rate used in this uniaxial testing scenario, was evident in the small strain behavior testing performed using the DMA shear method as shown in Figure 3-15. The results displayed in Figure 3-31 suggest that Hydrogel A is more sensitive to changes in both temperature and rate, as shown in the DMA testing results provided in Figure 3-15 and Figure 3-18, thus exhibiting a greater viscoelastic behavior and ability to dissipate a greater amount of energy compared to Hydrogel B because tan δ is increasing rather than plastic deformation. Additionally, although there is a pronounced increase in the recorded shear modulus of Hydrogel A as both temperature and rate increase, the results from Figure 3-30 suggest that for temperatures below 20^{o}C a decrease in temperature is shown to have a larger impact on the increase in modulus compared to rate. Lastly, these uniaxial tension results, most notably the trends for the shear modulus values for Hydrogel A and Hydrogel B, help to support the results obtained from the DMA shear tests.

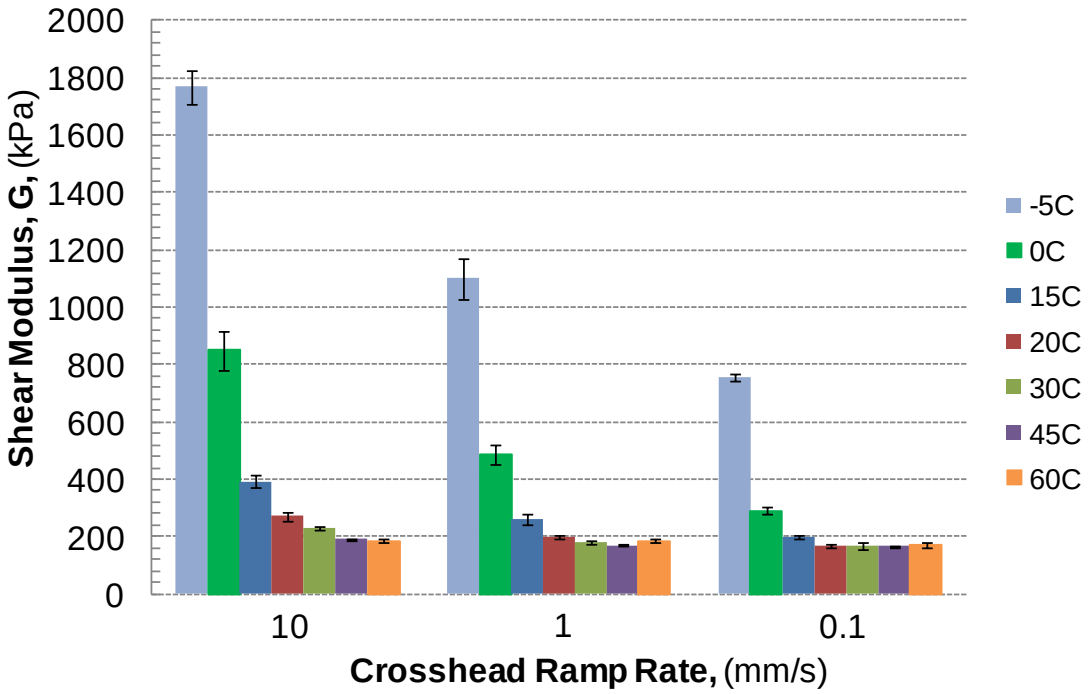

Figure 3-30: Average calculated shear moduli for Hydrogel A

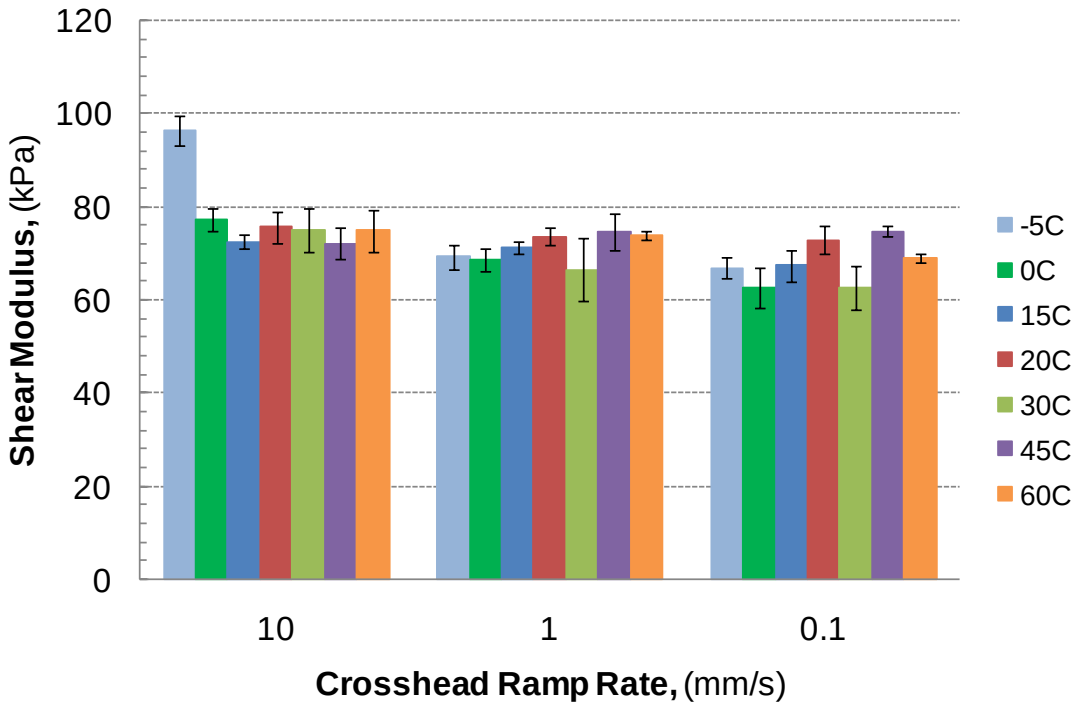

Figure 3-31: Average calculated shear moduli for Hydrogel B

Conclusions

Dynamic mechanical analysis (DMA) shear and uniaxial tension tests were successfully performed on the solvated silicone hydrogel systems A and B over a range of temperatures and rates. The small strain viscoelastic behavior provided by the DMA testing indicated that Hydrogel A possesses a greater storage and loss moduli compared to Hydrogel B for the tested temperature and frequency ranges at a reference temperature of 45^{o}C as shown in Figure 3-15 and Figure 3-16. Additionally, Hydrogel B was shown to exhibit relatively little to no viscoelastic behavior and be less sensitive to changes in temperature compared to Hydrogel A as seen in the acquired thermal shift factor plot, Figure 3-18. The large strain or hyperelastic behavior achieved through uniaxial tension testing proved to indicate similar trends of Hydrogel A and B with changes in rate and temperature. Also, Hydrogel A was shown to have a higher mechanical strength and toughness as displayed by the greater stress and strain at break values achieved in comparison with Hydrogel B which may be due to the higher solvent content of Hydrogel B. Also, rate and temperature were shown to greatly impact the calculated shear modulus of Hydrogel A for the tested temperatures and rates, while the calculated modulus for Hydrogel B proved to show little change with temperature and rate as indicated with the DMA shear results.

Characterizing the fundamental viscoelastic behavior of a solvated hydrogel system such as those obtained from these DMA shear and uniaxial tension tests can provide

tremendous insight into resolving issues with manufacturing of hydrogels or integrating a specific hydrogel system to an appropriate application. Also, observing that Hydrogel B is less sensitive to changes in temperature, as suggested by Figure 3-18 and Figure 3-31, would indicate that small changes in rate and temperature over a particular temperature region would not drastically change the material's behavior compared to Hydrogel A which is moving out of the rubbery plateau into a transition region. Such information can be vital when attempting to improve a manufacturing process of highly complicated viscoelastic materials such as silicone hydrogels.

Chapter 4 : Methods to Determine the Bulk Viscoelastic Fracture Behavior of Solvated Hydrogel Systems

Introduction and Background

Initially, hydrogels, due to their swollen nature, were regarded as a mechanically weak and fragile class of soft materials. As demand increased for tougher biopolymers in the biomedical industry as well as improvements to the technologies and synthesis methods for strengthening hydrogel systems, an understanding of what makes a particular hydrogel system difficult to break or fracture has resulted in recent efforts to characterize the highly deformable nature and fracture properties of hydrogel material systems [20]. This large strain response of hydrogels results in a blunting of the crack tip prior to propagating, similar to that of rubbers and other elastomers, which protects the crack tip from local increases in stress while loading of the sample continues [1]. This behavior results in no plastic deformation near the crack tip yet renders linear elastic fracture mechanics (LEFM) inapplicable to accurately characterize the fracture behavior and properties of hydrogels since hydrogels tend to fracture at strains well above this theory [35, 36]. Thus, methods to understand and analyze the large strain behavior and fracture of hydrogel systems, especially more robust systems, such as interpenetrating polymer network hydrogels, have been developed by adapting techniques typically used for rubbers [1, 20, 37]. Although several different fracture testing methods are currently being used to characterize the fracture behavior of various hydrogel systems, methods such as trouser tear, single edge notch (SEN) tension, and constrained tension, this thesis chapter focuses on the implementation of a mode I opening fracture of a “semi-infinite” hydrogel strip often referred to as a pure shear or constrained tension fracture test to determine the bulk viscoelastic fracture behavior of Hydrogel A and B [1, 19, 20, 37, 38].

In general, fracture mechanics is a branch of materials science and engineering which seeks to understand and characterize the behavior and parameters that form and propagate cracks through material systems [39]. Griffith developed an energy criterion for crack growth of brittle materials using a thermodynamic approach in which the growth of a crack results in the creation of two new surfaces producing an increase in surface energy. Griffith’s expression, Equation (17), shows that an initial crack of area A in a material body with a thickness, t, and constant length, a, grows if the change in total elastic energy, W, per unit increase in crack length is greater than or equal to the fracture energy, $\mathcal{G}$, required to form new crack surfaces. While terms such as fracture energy, tearing energy, and critical strain energy release rate ($\mathcal{G}_c$) are for material properties, the strain energy release rate (SERR) is reserved for situations relating to an imposed or applied fracture energy. Additionally, for time-independent systems, fracture occurs when $\mathcal{G}=\mathcal{G}_c$.

Rivlin and Thomas were the first researchers to successfully apply Griffith's criterion to the tearing of rubber [40, 41]. For the case of studying the rupture of rubber, $\mathcal{G}$ is no longer equal to the surface energy since rubber is not a brittle material and large local deformations occur at the crack tip resulting in a greater dissipation of energy. As long as the energy dissipation for an elastomeric body is confined to a small process zone at the crack tip, the tearing energy or strain energy release rate criterion for an elastomer is applicable [40, 41].

$$-\left(\frac{1}{t}\right)\left(\frac{\delta W}{\delta A}\right)_l \geq \mathcal{G} \tag{17}$$

The investigation of the fracture mechanics behind elastomers and other soft materials becomes increasingly complex because of their large deformations. An evolution of fracture mechanics and Griffith's energy criterion suggests the adhesive and cohesive strength of soft materials and elastomers can be characterized as the amount of fracture energy, $\mathcal{G}$, required to advance a crack by one unit area, which has experimentally been shown to be dependent on crack tip velocity, *v*, and temperature, *T*, where a simple power law, presented in Equation (18), can model the threshold fracture energy, $\mathcal{G}_o$, below which no fracture occurs and subcritical fracture region presented in Figure 4-1[42, 43] . Slower crack propagation rates corresponding to the non-propagating crack or threshold region can be achieved experimentally through slower loading rates or above ambient temperatures, while faster crack propagation rates corresponding to the subcritical and critical fracture regions require sub-ambient temperatures or faster loading rates [43].

$$\mathcal{G}(v,T) = \mathcal{G}_o\left(1 + f(v,T)\right) \tag{18}$$

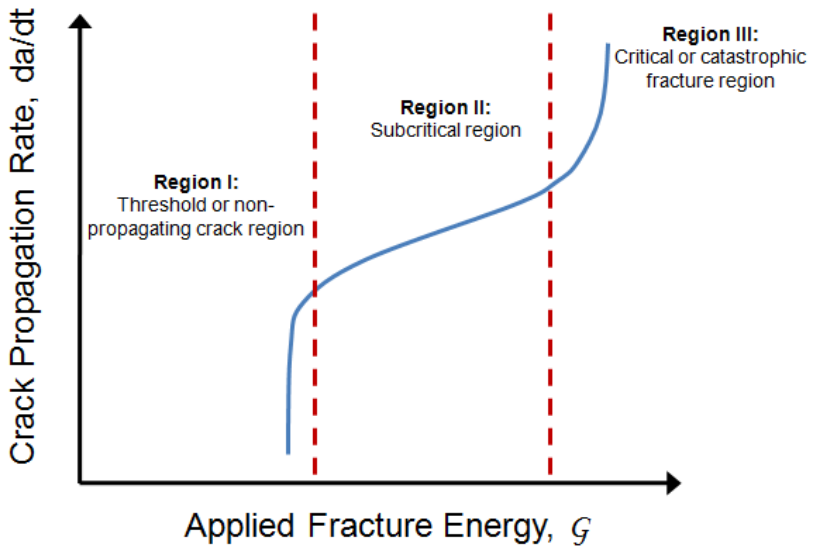

Figure 4-1: Representation of threshold, sub-critical and critical fracture energy region for a material's strain energy release rate (SERR) curve

Additionally, individual research performed by Baumberger and Tanaka found that the fracture energy of swollen hydrogel systems also depends on solvent at the crack tip and crosslink density, where solvent viscosity slows crack propagation and an increase in crosslink density often shows a decrease in fracture energy at a given velocity making the gels more brittle [37, 44-46]. Furthermore, research on the effect of crosslink density of the second polymer network on the fracture energy of double network hydrogel systems indicated a drop in the system's fracture energy as the crosslink density of the second network increased [44]. This decrease in fracture energy due to an increase in crosslink density relates to the classical Lake-Thomas theory for soft elastomers in which the molecular weight between the crosslink junctions is proportional to the threshold fracture energy of a material system based on the assumption that the energy between crosslinks is lost whenever a single bond is severed [47].

The relationships presented below for each of the following fracture geometries, trouser tear, SEN tension, and pure shear, have been used to characterize the fracture energy of hydrogels and other elastomeric materials. While originally these relationships and geometries were applied to the catastrophic tearing of elastomers, there are several cases which result in different types of crack growth based on the loading imposed on the sample. According to Ellul [40], one such case for amorphous non-strain-crystallizing elastomers, such as Hydrogel A and B, is slow and relatively constant crack growth that occurs while the sample is under constant stress. This type of fracture is often referred to as time-dependent or subcritical fracture. In contrast, for the case of a crystallizing elastomer, this time-dependent fracture is generally absent and fracture progresses in a "stick-slip" manner, in which the load increases during the stick portion

up until the critical or catastrophic fracture energy is reached and then the crack springs forward during the slip phase [40]. The trouser tear and pure shear fracture configurations exhibit a temporal instability in which the tearing energy is independent of crack length and the rate of propagation is effectively controlled by input of external work or loading of the sample [40, 48]. In contrast, unstable crack growth occurs for the SEN tension geometry when the applied fracture energy of the system exceeds that necessary to elicit crack growth. This is often referred to as a type of specimen or spatial instability that causes the crack propagation to accelerate and become uncontrollable, hence unstable for this particular geometry [40, 49].

With interests in further investigating the effects of temperature, rate, crosslink density, and environment on the fracture behavior of novel and hybrid hydrogel systems, several mode I and mode III fracture techniques typically used for testing elastomers have been implemented by many soft material researchers. One of the well defined geometries used to determine the mode III or out-of-plane shear mode fracture energy of elastomers and other soft materials is the trouser tear test [40]. Globally, this trouser tear method is a mode III fracture test; however, due to the crack often rotating during testing the crack grows in more of a mode I state. A diagram of this trouser tear geometry typically used for elastomeric materials is presented in Figure 4-2. This technique is usually performed by fixing the lower leg of the sample, while the upper leg is pulled upward at a constant rate. The fracture energy of a material tested in this configuration can be calculated using Equation (19), which simply includes the average of the tearing force, F_{ave}, and width, w, of one of the sample's legs. For this trouser tear test, the crack propagation rate is directly related to the crosshead displacement rate of the tensile testing machine, while other test methods, such as the SEN tension and pure shear, require monitoring of the crack length during testing [48].

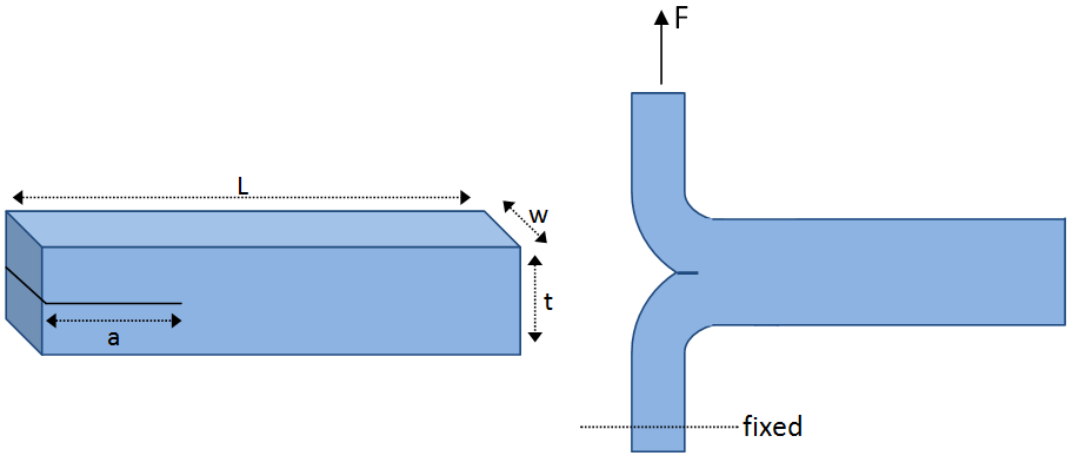

Figure 4-2: Diagram of trouser tear geometry

$$\mathcal{G} = \frac{F_{ave}}{2w} \tag{19}$$

This method was applied by Yu and Tanaka to examine the localized damage zone around the crack tip of double network hydrogels and determine a relationship between the thickness of the observed damage zone and the fracture energy to provide insight into the fundamental toughening mechanism of double network hydrogels which has become increasingly important to the field of regenerative medicine [50]. In their investigation, the damage zone around the crack tip, which corresponds to the softened regions just below the fracture surface due to localized damage accumulation, was directly observed using a color 3D violet laser scanning microscope with reflection mode after immersing the tested samples in water for several days [50]. The results of their study indicated that both fracture energy and thickness of the damage zone increased with the tearing velocity, and there was found to be a linear relationship between fracture energy and damage zone thickness. According to Yu and Tanaka's study, the damage zone thickness could result in several hundred μm, while fracture energy could reach several hundred J/m^2 for their tested double network hydrogel [50]. Such a relationship could prove helpful in attempting to minimize or eliminate damage to manufactured hydrogel products for various applications by restricting the amount of imposed fracture energy to keep damage of a hydrogel system to an acceptable level. Additionally, Tanaka *et al.* in earlier research work on a different variety of double network hydrogels utilizing this trouser tear method found a similar weak dependence of fracture energy on the tearing velocity and typical fracture energy values on the order of 10^2 and 10^3 J/m^2 [44, 45]. Both of these investigations implemented the analytical solution for calculating the fracture energy, $\mathcal{G}$, provided in Equation (19), where F_{ave} is the average tearing force and w is the width of a trouser leg [40, 44, 45, 50] . Although successful measurements of the mode III fracture for hydrogels have been obtained using this trouser tear approach, the relevance to this type of fracture occurring *in vivo* for implantable hydrogel materials has been questioned by many researchers who have implemented and modified mode I fracture approaches [35].

The application of the SEN tension and pure shear or constrained tension methods to investigate the mode I fracture behavior of bulk hydrogel systems have been used extensively by several prominent researchers in the field of hydrogel materials. Diagrams of these two techniques are provided below in Figure 4-3 and Figure 4-4, while details on the pure shear geometry, the fracture technique used to characterize the fracture energy of Hydrogel A and B, are included below in detail [40].

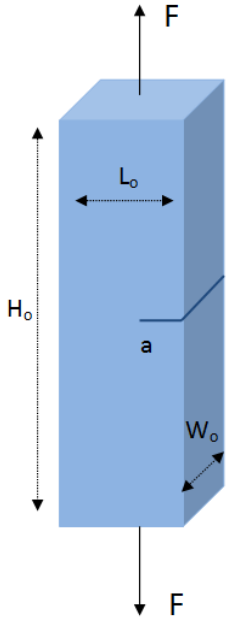

Figure 4-3: SEN tension fracture geometry

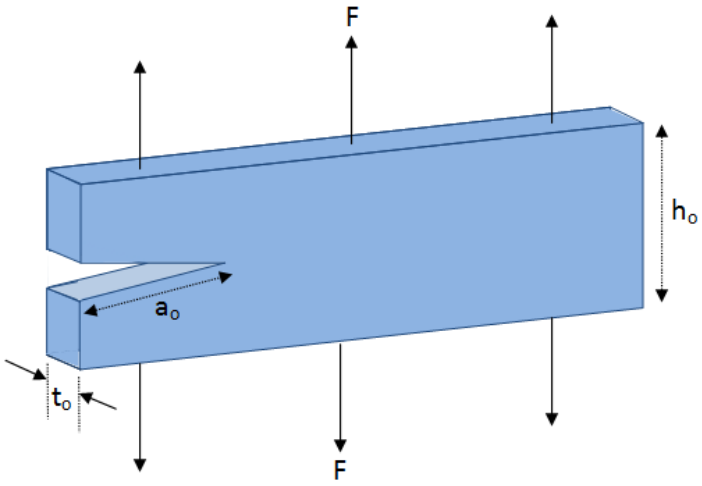

Figure 4-4: Constrained tension or pure shear fracture geometry

Research performed by Kong and Mooney investigated the effect of different crosslink densities on the work to fracture alginate hydrogels using a SEN geometry in tension. Their study found that increasing the elastic modulus of ionically crosslinked gels increased their toughness; however, above a certain elastic modulus, *E*, the toughness of covalently crosslinked gels was inversely related to the modulus due to the ability of calcium crosslinked gels to break in a partial or stepwise fashion which limited the crack from opening [46]. A SEN tension method was also utilized by Creton *et al.* to calculate the fracture toughness of hybrid hydrogel systems containing silica nano-particles [20]. Both Creton and Kong used an analysis provided by Rivlin and Thomas, Equation (20), to calculate the energy release rate, $\mathcal{G}$, of these hydrogels while recording the crack length, a, with a high speed camera [19, 20]. Additionally, *K* is a constant dependent on the geometry, not the stress intensity factor commonly used in fracture mechanics, and extension ratio, λ, and U_o is the strain energy density of the gel for a given extension ratio [20, 40]. The fracture results from Creton's study found a significantly greater toughness for hybrid hydrogel systems infused with inorganic nano-particles [20].

$$\mathcal{G} = 2K(\lambda)aU_o \tag{20}$$

Aside from the SEN tension method, the pure shear or constrained tension approach has also been used by several researchers to determine the fracture energy of various hydrogel systems. With this technique, the specimen is subjected to a uniform

displacement in the 2- direction with the condition that the length of the sample in the 1-direction is constrained, thus resulting in the extension ratio, $\lambda_1=1$, as shown in Figure 4-5 [48]. This geometry has been coined “pure shear” due to the tensile loading of this geometry which results in no rotation or change in length of the principal axes during deformation of the sample [40]. Furthermore, Figure 4-6 depicts the Mohr’s circle diagram for both stress and strain to provide additional insight into the this pure shear loading scenario [51]. Typically, the height of the sample in the vertical direction is approximately a tenth of the sample length, and the sample is rigidly clamped along the horizontal direction, denoted by upper and lower gray blocks as shown in Figure 4-5, to prevent significant lateral contraction of the sample, while it is deformed in tension [40]. During constrained tension fracture experiments, an initial notch is placed on the sample as denoted in Figure 4-4, and the crack propagation rate is measured during the test by monitoring the crack length [1, 48].

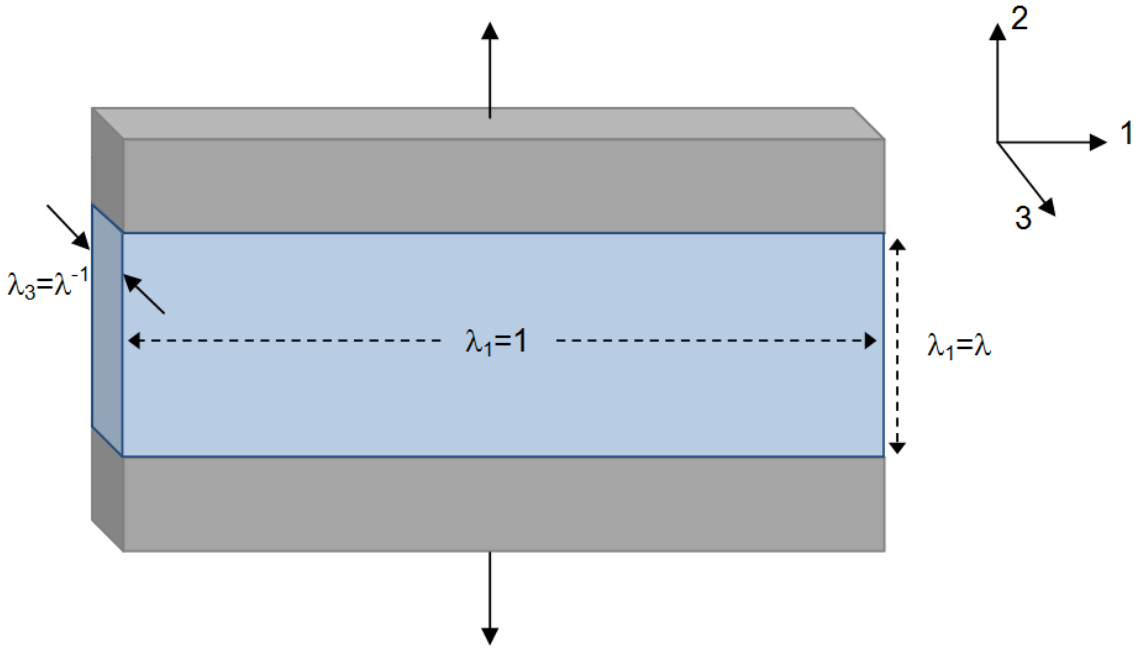

Figure 4-5: Diagram of constrained tension or pure shear

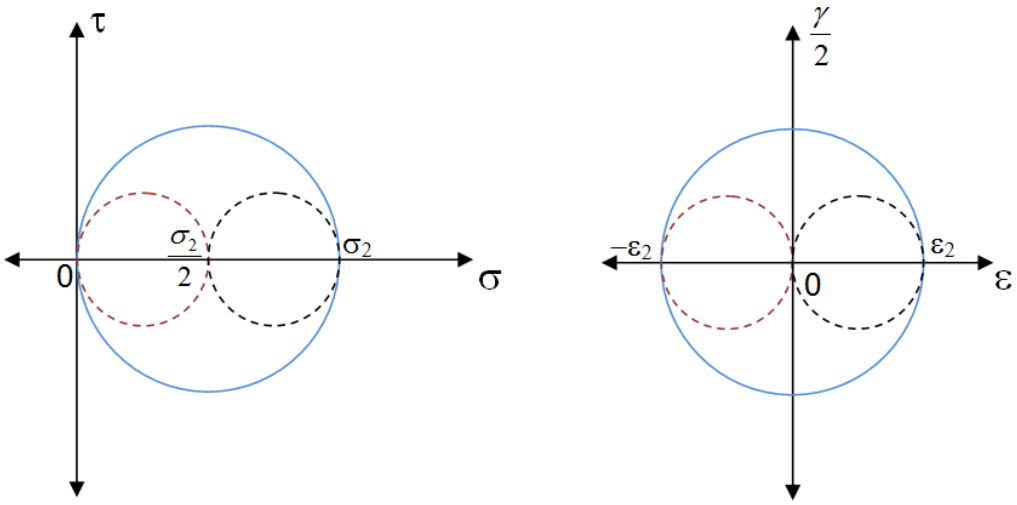

Figure 4-6: Mohr's circle diagram for stress (left) and strain (right) for pure shear configuration

Additionally, Figure 4-7 depicts four regions, A-D, which correspond to different regions of interest for this steady state fracture approach. Region *A* represents the wake or unstrained region, segment *B* is the process zone where fracture takes place and involves a very complex state of strain, area *C* is under a biaxial tension, and portion *D* exhibits edge effects.

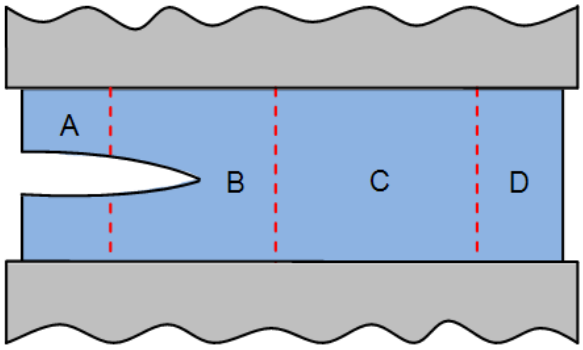

Figure 4-7: Diagram of the pure shear or constrained tension geometry

Fracture energy for a constrained tension sample can be calculated using Equation (21), where the mode I fracture energy, $\mathcal{G}$, utilizing Griffith's energy criterion, is equal to the change in strain energy, *U*, over the change in crack area, *A*. Additionally, the initial dimensions of the sample, such as thickness, t_o, the length, l_o, the crack length, a, and the height, h_o, which make up the un-cracked volume can be multiplied by the strain energy density, U_o, to replace the strain energy term. This then equals the strain energy density, U_o, multiplied by the initial height of the specimen, h_o, as seen in Figure 4-4. For this calculation of the applied fracture energy, the strain energy density can be

calculated using the Gaussian theory of rubber elasticity which accounts for a decrease in the cross sectional area once the sample is placed in tension, as shown in Equation (22) [14, 16].

$$G_I = -\frac{dU}{dA} = -\frac{d\left(U_o t_o h_o \left(l_o - \left(l_o - a\right)\right)\right)}{d\left(a t_o\right)} = U_o h_o \tag{21}$$

$$U_o = \frac{1}{6} E\left(\lambda_1^{\,2} + \lambda_2^{\,2} + \lambda_3^{\,2} - 3\right) \tag{22}$$

While the above treatment of this constrained tension fracture test provides an effective means to approximate the fracture energy for a elastomeric system under substantial deformation, this method glosses over possible viscoelastic behavior during the fracture testing of soft materials such as hydrogels that could greatly impact the measured fracture energies. Many researchers interested in characterizing the fracture energy of soft materials have implemented advanced methods such as finite element analysis (FEA) and digital image correlation (DIC) to investigate the time-dependent fracture and the addition of viscoelastic effects to the fracture analysis [1, 52]. Seitz *et al.* and Baumberger *et al.* conducted several investigations implementing the pure shear fracture geometry to determine the rate dependence and effects of solvent and other environmental conditions on tri-block co-polymer and biopolymer hydrogels, respectively [1, 3, 37, 38]. Strips of their biopolymer hydrogel were cured between two strips of Velcro®, as illustrated in Figure 4-7, used to hold the hydrogel during testing. This novel technique has also been used to characterize the fracture behavior of poly-electrolyte hydrogels performed by Miquelard-Garnier *et al.,* respectively [1, 19]. While several researchers have employed this constrained tension fracture method to hydrogels, Seitz is one of the forerunners investigating the fracture behavior of hydrogels using a finite element approach. Results from his finite element study on several acrylic triblock copolymer gels exposed to this constrained tension fracture method indicated that the stress field directly ahead of the crack to be highly anisotropic and significantly different from predictions provided by LEFM. Seitz explained that this was due to the region of high tensile stresses far in front of the crack tip which resulted in inefficient transfer of elastic energy to the moving crack tip, thus enhancing the energy dissipation of gel systems and increasing fracture toughness of gels at high rates.

Aside from incorporating finite element-based approaches to study and understand the fracture behavior of highly compliant soft materials, DIC systems are effective tools to capture high resolution stain fields for in and out of plane measurements of tested material systems which have been shown useful in studying the time-dependent

fracture and constitutive behavior of elastomeric materials [52, 53]. Although the application of DIC systems to study viscoelastic and fracture behavior of hydrogels and other gel systems has been limited, Moy has conducted interesting research on the fracture behavior of ballistic gelatin systems with the aid of DIC equipment [53]. Results from his investigations provide encouraging evidence that DIC systems could be used to study viscoelastic dissipation associated with large strain fracture behavior of hydrogel systems in order to provide refinements to fracture energy calculations.

Effectively characterizing the fracture behavior of solvated hydrogel systems is critical to understanding the mechanisms which can result in defects during the manufacturing of these materials for various applications, as well as determining ways to improve and strength these materials for biomedical applications. Mode I and mode III fracture methods such as the constrained tension configuration and trouser tear, respectively, have successfully been used to determine hydrogel fracture behavior as well as the fracture energy's dependence on temperature, solvent at crack tip, and crosslink density. However, research investigating the rate and temperature dependence of fracture energy for hydrogel systems has been relatively limited and could provide beneficial insight into improving hydrogel manufacture and application. The remainder of this chapter discusses an experimental method and results utilizing the mode I constrained tension fracture approach under several different loading methods to examine the effects of temperature and rate on the fracture behavior of Hydrogel A and B.

Experimental Procedure

Sample Preparation

A 7.6 cm by 20 cm sheet of the desired hydrogel system with a uniform thickness of approximately 0.2 cm, presented in Figure 4-8, was cured using the bulk hydrogel sample casting method outlined in Chapter 2 for all bulk fracture tests. After removing a sample from its polypropylene encasement, it was prepared by placing a 1.8 cm wide strip of pressure sensitive adhesive (PSA) tape (Scotch® Magic™ 3/4") along the four 20 cm edges, both sides of the front and back of each sample, so that all four PSA tape strips were parallel to each other and contained a 2.5 cm gap between the parallel PSA tape strips on each side of the sample as shown in Figure 4-9. Due to complications resulting in damage to the solvated hydrogel systems when gripping the material directly, this tape was applied in order to reinforce the sample while placed in the grips during testing and provide a surface to adhere the aluminum reinforcement bars which were an extra means to protect the sample from breaking at the grips. Initial tests using this entire sample preparation for constrained tension fracture of these systems verified no slippage of the PSA tape during testing.

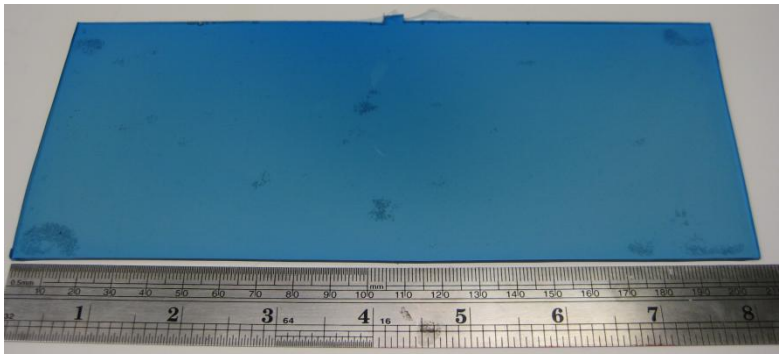

Figure 4-8: Cured sheet of Hydrogel A

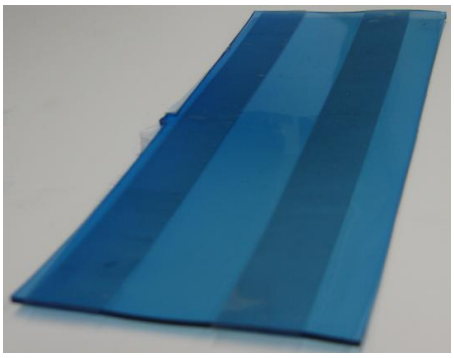

Figure 4-9: Cured sheet with PSA tape strips

Seven holes, 5/8” in diameter, were stenciled on to each 20 cm long PSA tape strip using a marker and aluminum reinforcement bars, approximately 20 cm by 2.5 cm, with seven equally spaced 5/8” diameter holes. Then, holes were punched along each 20cm edge, as shown in Figure 4-10, using a punch die and hammer. The aluminum reinforcement bars with small 2.5 cm long strips of double sided PSA tape (Scotch® Permanent Double Sided Tape 3/4”) between the holes were attached to the 20 cm edges by aligning the punched holes on the hydrogel sample and aluminum bars as shown in Figure 4-11. This double-sided layer of PSA tape was applied in order to keep the reinforcement bars in place while loading the sample into the grips. Additionally, no evidence of slippage from the tape applied to the sample was found by initial testing of this constrained tension fracture method.

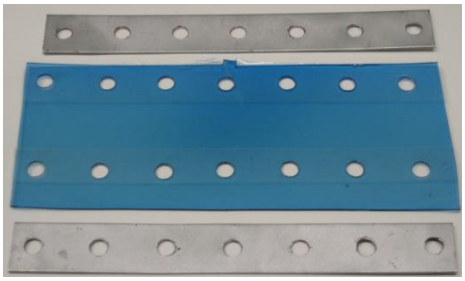

Figure 4-10: Hydrogel sheet with punched holes

Figure 4-11: Hydrogel sheet with attached aluminum reinforcement bars

After securing the aluminum reinforcement bars to the bulk fracture sample, excess hydrogel along the outer edges was removed using a razor blade. A razor blade aligned with a steel ruler was then used to insert a 10 mm initial notch, a_o, at the midline of the sample as shown in Figure 4-12 and Figure 4-13. In the end, the actual tested hydrogel material between the aluminum bars has a length to height aspect ratio of 8:1 which translates into 20 cm by 2.5 cm rectangular strip as depicted in Figure 4-12.

Figure 4-12: Finished constrained tension fracture sample (Hydrogel A)

The length, l_o, of each sample was measured using a steel ruler with 0.5 mm increments and the initial height, h_o, was measured using digital calipers. Lastly, the initial thickness, t_o, of each sample was measured with the Mitoyoto ® micrometer and the method described in Chapter 3.

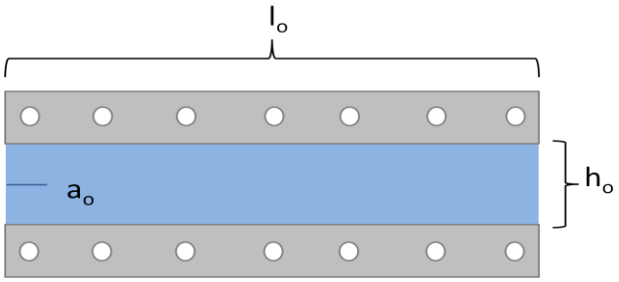

Figure 4-13: Diagram of fully prepared constrained tension fracture specimen

Loading Scenarios and Testing Procedure

Three different loading scenarios were used to obtain the data necessary to construct the subcritical fracture curves for these hydrogel systems where a fixed, increasing, or decreasing strain condition was applied to a constrained tension fracture sample. For both the fixed and increasing strain loading scenarios, fully prepared samples were secured in the aluminum constrained tension grips as depicted in Figure 4-14, while mounted on an Instron MicroTester 5848 load frame equipped with a 2 kN load cell shown in Figure 4-15. Samples were secured by fastening all fourteen bolts so that the sample was not overly compressed resulting in bulging of the material at the grips, which would damage the material and cause fracture at the grips. Also, it was important that the bolts were not too loose which would cause the material to fail at the bolt locations. After securing the sample in the constrained tension grips, any slack in the sample was removed by finely adjusting the crosshead so that there was no visible slack in the specimen or initial strain in the sample. A ruled paper strip with 0.5 mm increments was placed above the sample on the aluminum grips, as shown in Figure 4-14, in order to provide a reference measurement for images of the crack length acquired by a high-speed camera, a Photron® Fastcam APX-RX, used to determine the

crack length during the fracture tests. Additionally, all tests conducted at temperatures other than ambient temperature (20^{o}C) were performed within the custom- made environmental chamber, shown in Figure 4-15, in order to adequately control the temperature for each test.

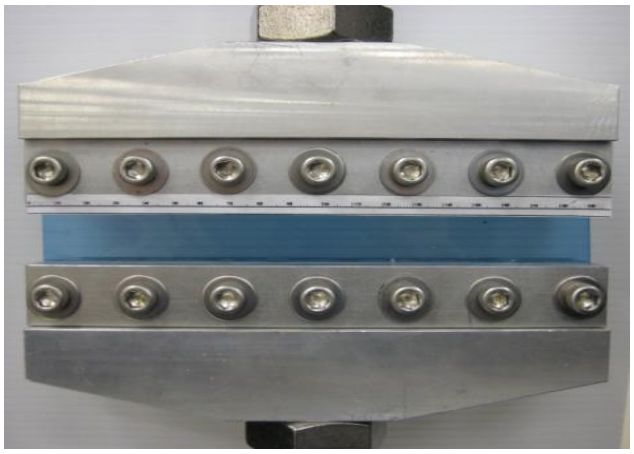

Figure 4-14: Mounted constrained tension fracture sample

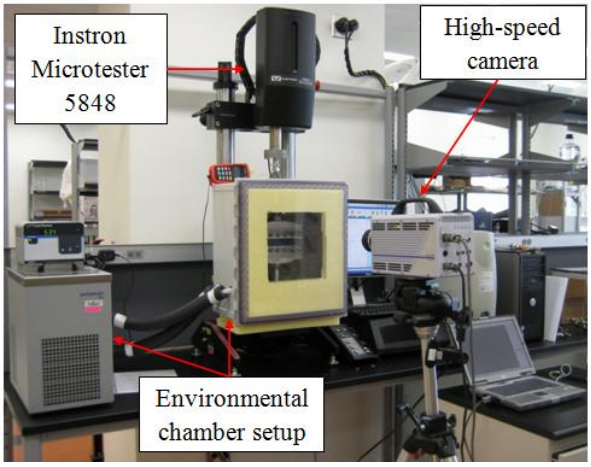

Figure 4-15: Increasing and fixed strain scenario constrained tension fracture setup

During the fixed strain loading, a sample was rapidly ramped at a 10 mm/s or 5 mm/s crosshead ramp rate for Hydrogel A and B, respectively, to a prescribed level of strain, which was based on the initial height of the sample, h_o, shown in Figure 4-13, and held until the sample was fully fractured as graphically depicted in Figure 4-16. As an example, Figure 4-16 shows that the crack length for this fixed strain case increases at a fairly constant rate with an initial jump at the opening of the crack and a pronounced decrease in rate towards the end of the sample. Constrained tension fracture samples of Hydrogel A were tested at prescribed strain levels of 30, 40, 50, and 60% strain, while Hydrogel B samples were tested at prescribed strain levels of 10, 20, 30 and 40% with one trial per strain level for both material systems. These strain levels were chosen for Hydrogel A due to difficulty in producing crack propagation within time range capable for recording crack propagation with the high-speed camera, and the other strain levels were chosen for Hydrogel B for this fixed strain case since the samples would experience unstable crack growth while ramping to strain levels above 40%.

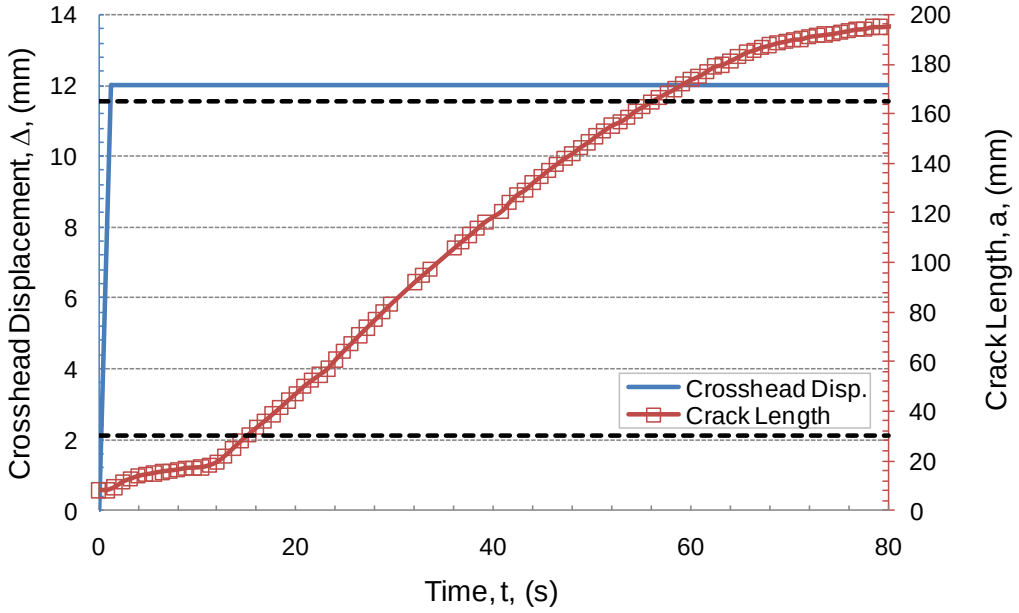

Figure 4-16: Fixed strain loading scenario

Additionally, constrained tension relaxation tests, depicted in Figure 4-17, were conducted on Hydrogel A and B in the Instron MicroTester 5848 load frame for each of the prescribed strain levels, $\hat{\varepsilon}$, tested under the fixed strain fracture method. For these tests, a sample without a pre-crack was rapidly ramped, at the same rates previously mentioned, to its respective strain level in order to determine an effective modulus, E(t), presented in Equation (23). The stress in this equation, $\sigma(t)$, was calculated from the Instron load data and sample dimensions. From the resulting stress relaxation curves for Hydrogel A and B, effective moduli for each tested strain levels were determined by fitting a simple power law equation of the form $E(t) = At^{-B}$, where A and B are constants from the acquired fit. This quasi-elastic approximation was then applied to Equation (22) by replacing the elastic modulus value, E, and was synchronized with the high-speed camera images of crack propagation. Each constrained tension relaxation test was conducted for at least the same duration as the fixed strain fracture test at the given strain level in order to provide enough data for the effective modulus. This was an initial attempt to investigate and introduce viscoelastic time-dependent behavior into this fracture analysis for solvated Hydrogel A and B. Additional details on this method and its results in regards to the stress relaxation curves and fits applied to Hydrogel A and B can be found in Appendix D.

$$E(t) = \frac{\sigma(t)}{\hat{\varepsilon}} \tag{23}$$

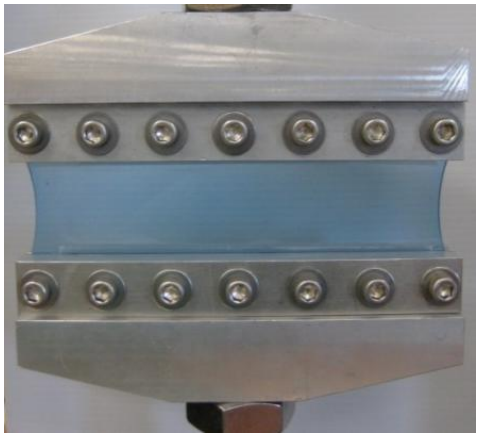

Figure 4-17: Constrained tension relaxation test (Hydrogel A, 60% strain)

For the increasing strain case, shown in Figure 4-18, a constant crosshead ramp rate of 10 mm/s and 1 mm/s for Hydrogel A and 5 mm/s and 1 mm/s for Hydrogel B was applied to the sample until the crack propagated across the entire length of the sample. The crack length for this setup proved to accelerate rapidly as the crosshead advanced. At least two trials were performed for each tested rate of these hydrogel systems at ambient conditions (20^{o}C). Also, only the data between the horizontal black dashed lines for the fixed and increasing strain cases, shown in Figure 4-16 and Figure 4-18, respectively, were used in the analysis of the applied strain energy release rate for each hydrogel system. The data outside these regions, the first 25 mm and last 25 mm of a sample, was heavily affected by initial and end loading conditions associated with this constrained fracture setup which did not satisfy the steady state fracture approach presented in Equation (21) and Equation (22).

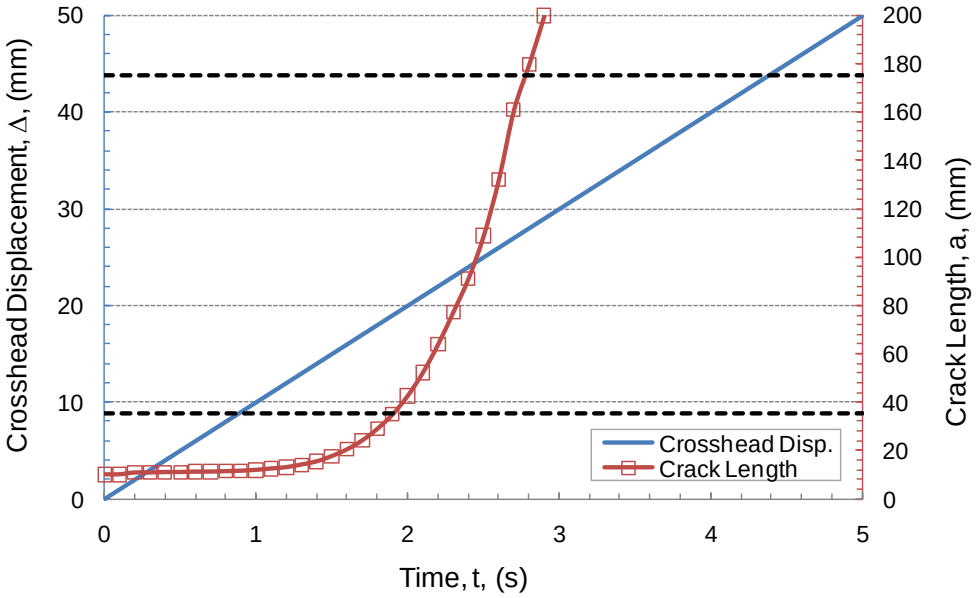

Figure 4-18: Increasing strain loading scenario

For both the fixed strain and increasing strain tests it was important to continually capture the crack length during the test; therefore, a high-speed camera was used to capture continuous images of the crack as it propagated over the entire sample. The high-speed camera was synchronized with the start of the Instron MicroTester and the recorded images were processed using a program developed in MATLAB ® that tracked the position, length, and propagation rate of the crack as well as calculate the strain energy density and applied fracture energy at each instant in time. An example of the images recorded by the high-speed camera and processed by the developed MATLAB® program are presented in Figure 4-19, which shows the original recorded image (top), the processed image to determine the crack region (middle), and the location of the crack tip at that particular instant (bottom). Further details and an example of the MATLAB® crack tracking code developed for this test method can be found in Appendix E.

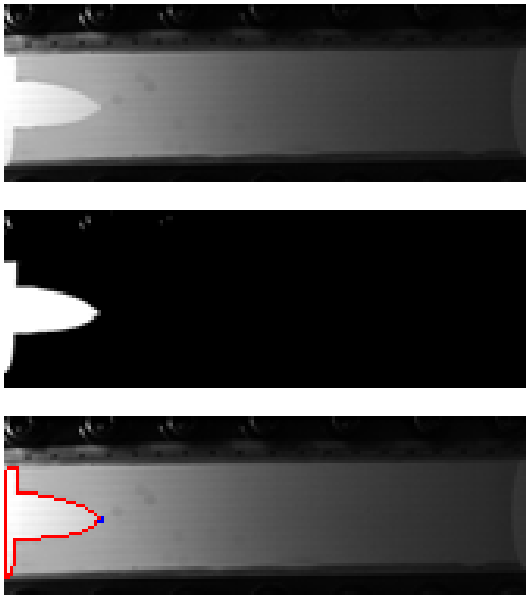

Figure 4-19: Example of the original constrained tension fracture images recorded by a high-speed camera (top), a processed image to determine the crack region (middle), and the detected location of the crack perimeter and tip (bottom)

While the increasing and fixed strain loading conditions provided sub-critical values of the SERR curve for these material systems, this decreasing strain scenario permitted extension into the threshold region of the SERR curve. The decreasing strain case was performed differently than the other two loading scenarios in that the specimen was loaded manually rather than within a load frame. The pre-notched end of the sample was opened to a particular strain, approximately 20% for Hydrogel A and 10% for Hydrogel B, while the other end was constrained to ideally 0% strain, as displayed in Figure 4-20, and the crack propagated until it arrested. The end of the decreasing strain

sample that was constrained to 0% was pinned to prohibit movement of this end for the duration of the test.

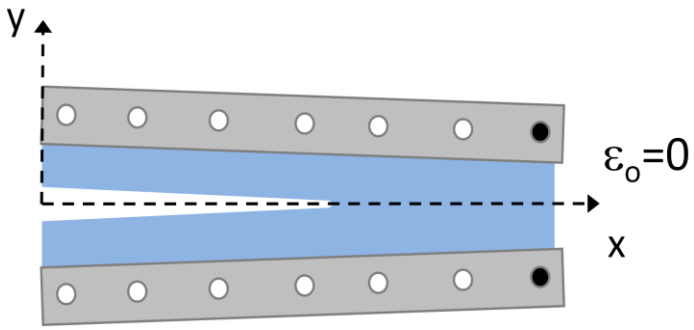

Figure 4-20: Diagram of decreasing strain loading scenario

An equation for the height, h, of the sample as a function of the crack length, *a*, was generated after the completion of each test assuming the crack started and propagated along the midline of the sample as shown in Figure 4-20. Equation (24) represents this linear relationship and was used to determine the extension ratio values for Equation (22) in order to calculate the strain energy density and then the fracture energy of the hydrogel systems as the crack propagated along the sample, where h_o is the initial height of the sample, h_f is the final height of the sample at the arrested crack tip, and a_f is the final crack length measured from the left end of the sample to the crack tip.

$$h(a) = (h_o + \Delta h_o) + \left(\frac{h_f - (h_o + \Delta h_o)}{a_f} \right) a \tag{24}$$

For this loading case, crack length measurements were manually recorded at different time intervals until crack advancement could no longer be detected over a significant period of time, as shown in Figure 4-21. The crack length, from the left end to the crack tip, was visually measured from ruled paper strips with 0.5 mm increments placed beneath the tested sample which started from the left end at 0 mm, as suggested by Figure 4-20. Three specimen of each hydrogel system were tested using this decreasing strain method over a period of 5 days at ambient conditions. Additionally, one long term decreasing strain constrained tension fracture test was performed on each material system in which the samples were tested over 10 days in order to fully determine the threshold fracture energy region. Furthermore, scanning electron microscope images of the fracture surface of these long term decreasing strain tests were conducted and are displayed in Appendix F. While this decreasing strain technique was capable of capturing this threshold fracture energy data for Hydrogel A and B, solvent egress and its potential effects on both hydrogel systems need to be considered since these tests were conducted over relatively long time spans while exposed to ambient conditions.

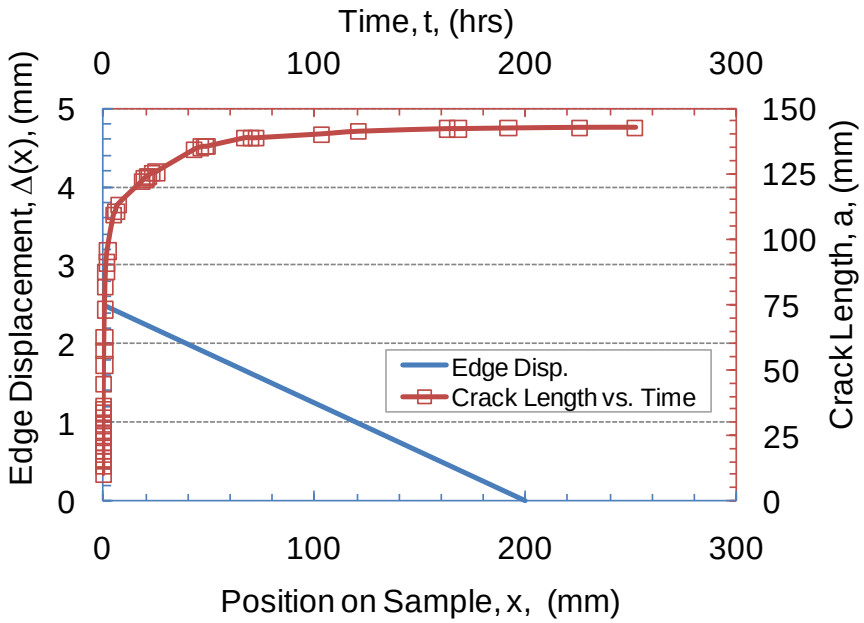

Figure 4-21: Decreasing strain loading scenario

Temperature Testing

As previously mentioned, all constrained tension fracture testing of Hydrogel A and B was performed in a custom-made environmental chamber, presented in Figure 4-15 in order to control the temperature of the testing environment. Only the increasing strain scenario was used to investigate the temperature dependence of the fracture behavior for each hydrogel system. Two constrained tension fracture trials were performed at each of the following temperature levels 0, 15, 30 and 45^{o}C for Hydrogel A and B. After samples were mounted in the constrained tension grips and the environmental chamber reached the desired testing temperature, the sample was enclosed in the chamber for 15 minutes before the start of the test in order to thermally equilibrate. Since results of the solvent egress study on both of these materials systems indicated substantial decrease in solvent content over two hours as shown in Appendix A, solvent egress would only be exacerbated by elevated temperature testing, thus the thermal equilibration time was set to a consistent 15 minutes for all tested temperature levels. The temperature inside the chamber was monitored using an Omega ® HH802U thermocouple unit which was placed within 10 mm of the center of the constrained tension sample to ensure the sample was equilibrated to the desired temperature. Additional testing to ensure that the internal temperature of the specimen reached the desired temperature level by the 15 minute equilibration time was performed by inserting a thermocouple inside of a 2 mm thick sample of each hydrogel system. The results from these tests were used to generate SERR master curves for both Hydrogel A and B and provide insight into the critical SERR of both systems.

Plane Strain Verification

In order to experimentally verify that plane strain conditions do not fail for this bulk fracture testing method, one trial of a Hydrogel A sample with a thickness four times that of the normal bulk fracture samples, 8 mm, was casted as shown in Figure 4-22. Due to the increased thickness of this sample, the sample was exposed to the UV light source for approximately 30 minutes as opposed to the usual 10 minute cure time in order to ensure proper solidification of the sample. The sample was tested under increasing strain conditions mounted in the constrained tension grips on the Instron Microtester, as presented in Figure 4-23 and Figure 4-24, at a 10 mm/s crosshead ramp rate and ambient conditions.

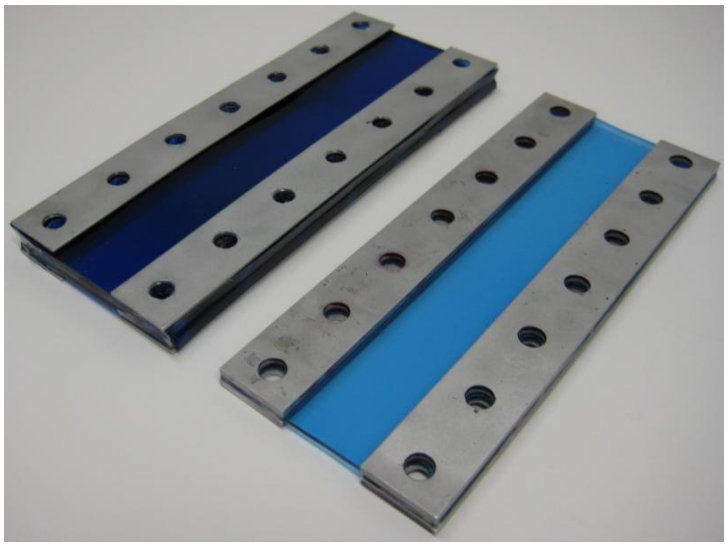

Figure 4-22: Comparison of 8 mm thick sample (left) and 2 mm thick sample (right)

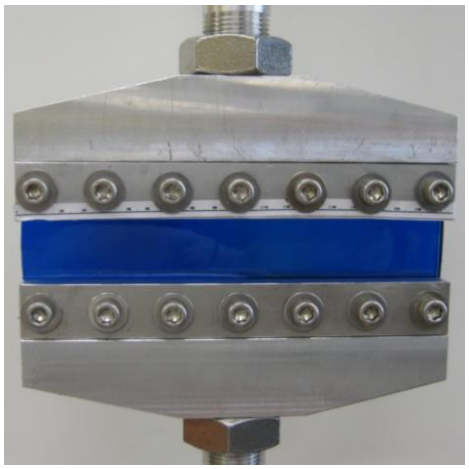

Figure 4-23: Four times thicker constrained tension sample mounted in Instron Microtester

Figure 4-24: Side view of four times thicker constrained tension sample

Methods to Investigate Viscoelastic Fracture of Hydrogels

Since the current steady state fracture approach used to determine the fracture energy of the solvated hydrogels suggests all the externally applied energy is released by fracture, two novel experimental techniques were used to investigate possible viscoelastic dissipation during the time-dependent fracture of Hydrogel A at ambient conditions. Only the time-dependent fracture of Hydrogel A was studied because the results presented in Chapter 3 indicated that it was in a transition region, meaning it demonstrates viscoelastic behavior, while Hydrogel B was shown to be on an equilibrium plateau exhibiting very little to negligible viscoelastic behavior. Both methods implemented this constrained tension fracture geometry operated with the fixed strain loading condition to observe possible viscoelastic recovery in the wake region of the crack, since this method provides a fairly constant crack propagation rate. This is an important phenomenon to examine because if either permanent deformation or time-dependent recovery of strain occurs, then the total amount of energy calculated earlier was not only used to drive the crack. The current method to calculate the fracture energy of the solvated hydrogels in this thesis considers that all the energy imparted on the system due to loading is released through fracture as illustrated by the shaded region under the loading curve in Figure 4-25. However, if loading of the sample during these fracture tests imposes permanent deformation as shown for case 1 in Figure 4-25 or there is viscoelastic recovery of the material after fracture as shown for case 2 in Figure 4-25, then the original method to calculate fracture energy as all the energy imparted on the sample during loading is in fact an overestimate of the fracture energy of these hydrogel systems.

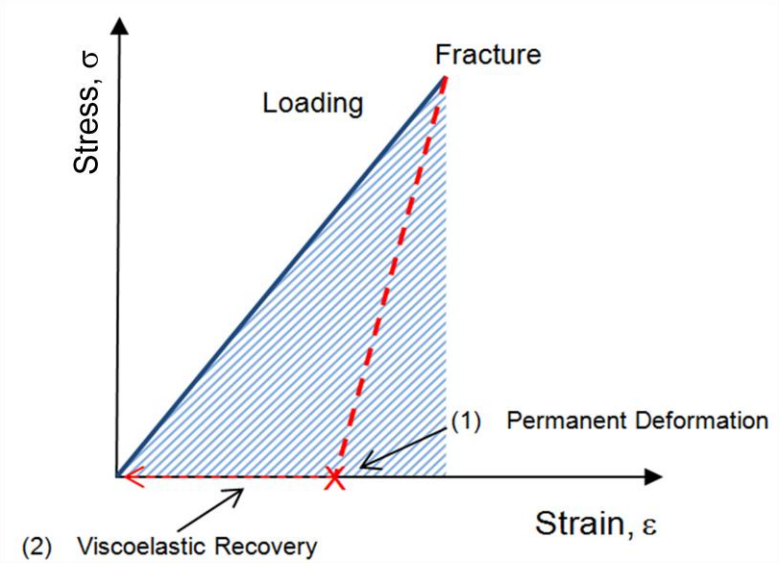

Figure 4-25: Diagram depicting cases for (1) permanent deformation or (2) viscoelastic recovery after fracture

The first method used images of the propagating crack at the 50 mm, 100 mm, and 150 mm positions along the sample which were obtained with the high-speed camera, as shown in Figure 4-26, for fixed strain cases at 30%, 50%, and 60%. The entire profile of the crack was analyzed in each of these images using imaging techniques in MATLAB® in order to determine the crack opening displacement (COD).

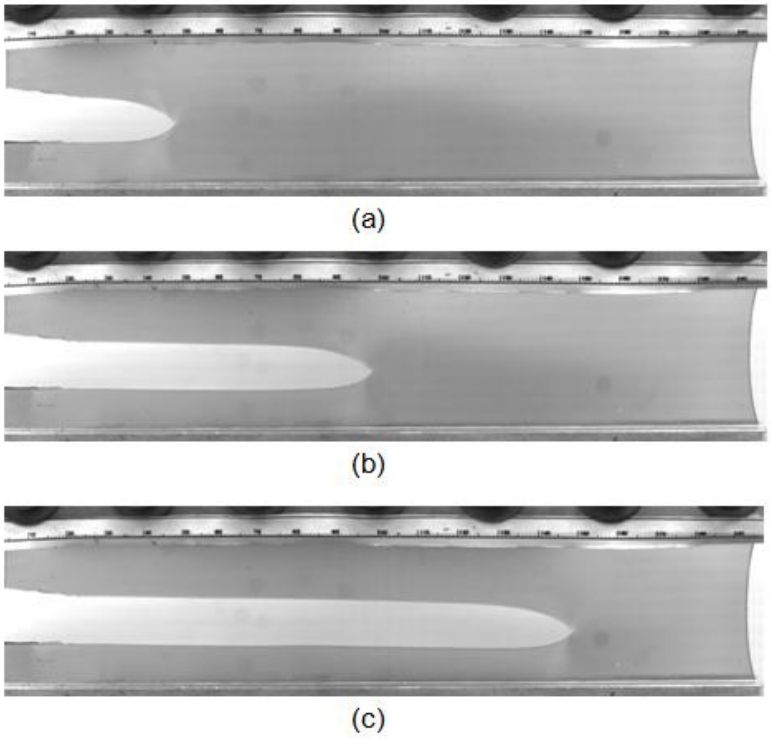

Figure 4-26: High-speed camera images of crack propagation through a Hydrogel A sample under fixed strain loading of 50% with the crack tip at (a) 50 mm, (b) 100 mm, and (c) 150 mm

By observing the behavior of the COD for Hydrogel A along the entire profile of the crack as it propagated past certain positions along the sample, insight into the amount of energy dissipated due to the imposed viscoelastic deformation ahead of the crack tip could be observed by possible viscoelastic recovery in the wake region of the sample over time. Under ideal conditions, if the bulk solvated hydrogel material exhibited no viscoelastic behavior at ambient conditions and for the tested rate, as is the case for Hydrogel B, the COD would reach a limiting value for distances far behind the crack tip that would remain the same signifying only elastic behavior which is not time-dependent, as indicated by the dotted red line in Figure 4-27. Distances far behind the crack tip, approximately the length of one or two specimen height, were studied due to the stress field surrounding the crack tip. For the case of a viscoelastic response, the COD would exhibit a time-dependent relaxation which would increase the COD by a finite amount, $f_{VE}(t)$, at regions far behind the crack tip as time progressed, as represented by the dotted blue line in Figure 4-27. This results as the material within

the wake continues to recover to near its original dimensions over time. Additionally, the h_o distance presented in Figure 4-27 represents the initial height of the sample and h_T represents the total height of the deformed sample which is shown to include the h_1 and h_2 distances representing the remaining material on either side of the crack and the COD; however, for cases were viscoelastic dissipation is observed a time-dependent term, $f_{VE}(t)$, is shown to increase the COD. Figure 4-27 indicates the crack separates the sample into halves in which each half of the material possesses a height, h_1 and h_2, which should be equal to h_o provided that no permanent deformation or time-dependent strain recovery occurs. Furthermore, if no increase in the COD is observed at distances far behind the crack tip for the given time frame needed for the crack to fully propagate across the sample, the viscoelastic deformation for Hydrogel A could be considered negligible at ambient and above ambient temperatures.

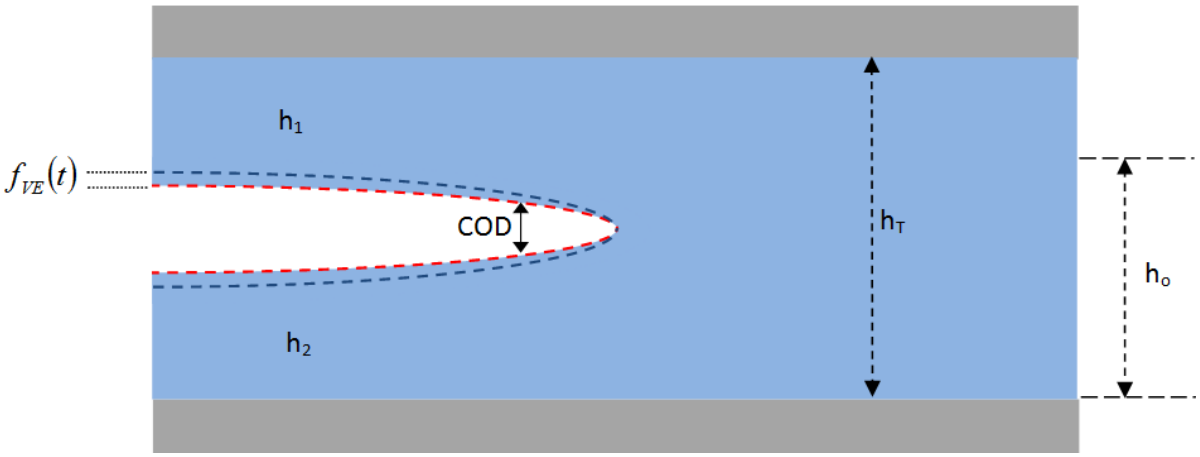

Figure 4-27: Constrained tension diagram with elastic (red) and viscoelastic (blue) cases for the crack opening displacement (COD)

The second experimental method used to investigate viscoelastic fracture of Hydrogel A utilized a digital image correlation (DIC) system developed by GOM® in order to also observe any potential viscoelastic dissipation in the wake region of a crack. This technique required the constrained tension fracture samples to be lightly speckled with solvent-less paint (India Ink), as shown in Figure 4-28 and Figure 4-29, in order to track the in-plane strain.

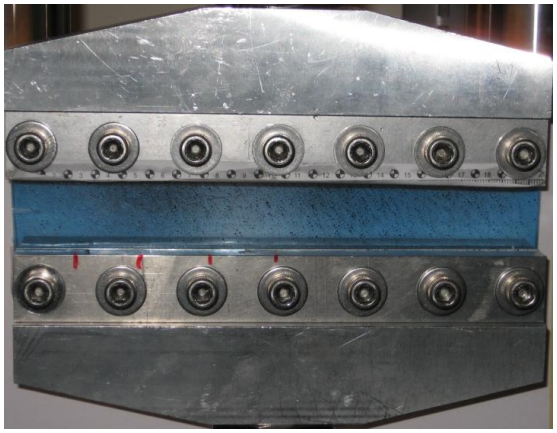

Figure 4-28: Constrained tension fracture sample with speckle pattern

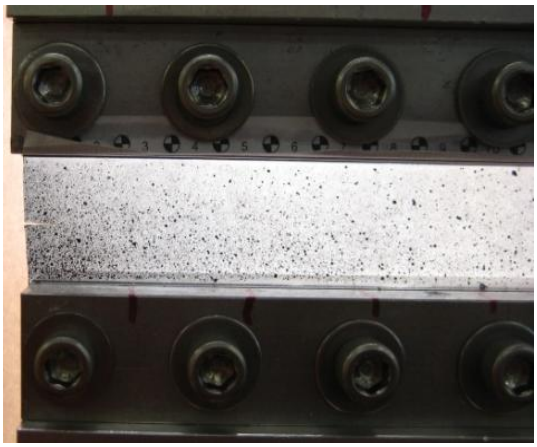

Figure 4-29: Close up of speckle pattern on Hydrogel A

For this experiment, three fixed strain constrained tension fracture tests were conducted on Hydrogel A after preparing and mounting the samples onto the Instron MicroTester 5848 as discussed in the above sections of this chapter. Samples were then ramped to a strain level of 50% with an initial ramp rate of 2.5 mm/s, while the DIC system, which was synchronized with the start of the Instron, recorded the in-plane strain. The initial ramp rate used for this experiment was slower than that used for other fixed strain tests due to problems with the DIC system recognizing the rapidly deformed sample. The tracking algorithm used by the DIC system requires modest strain increments in order to detect changes from the reference state which could have been resolved by increasing the sampling rate of image acquisition or reducing the initial ramp rate. Due to limitations in adjusting the sampling rate to detect the change in deformation, a reduction of the initial ramp rate to the prescribed level of strain proved imperative to capturing quality images of this time-dependent fracture behavior with the DIC system. During these tests, samples were backlit with diffusive light as shown above in Figure 4-29. This entire setup is depicted in Figure 4-30. Although several successful trails were performed on Hydrogel A samples with this DIC technique, significant progress was not made on the analysis of the resulting data before the end of the project; however, images of the strain fields during fracture and suggestions on how to analyze the obtained data are included in Appendix G.

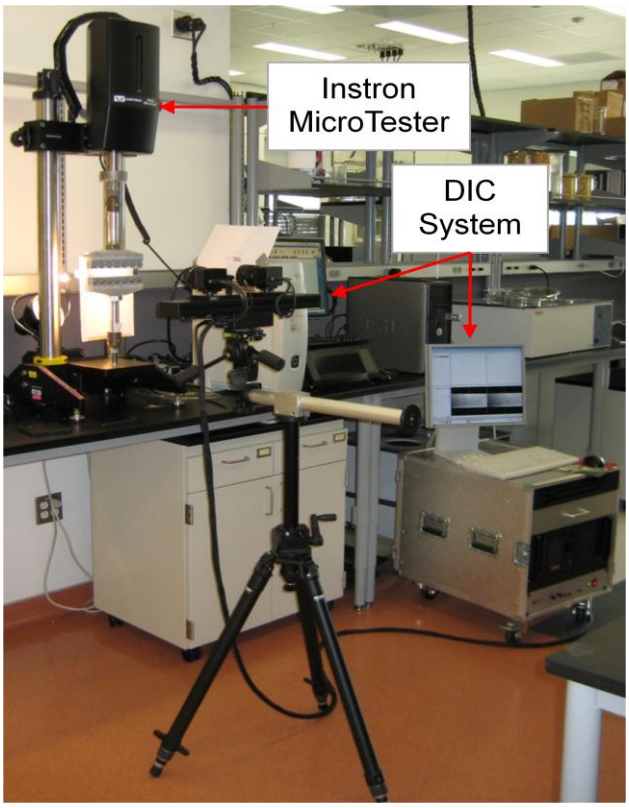

Figure 4-30: Constrained tension fracture setup with DIC system

Results and Discussion

Subcritical Fracture Energy Master Curves

The raw or unshifted fracture energy data for Hydrogel A and B at each of the tested temperature levels is presented in Figure 4-31. In order to construct the subcritical strain energy release rate (SERR) master curves for Hydrogel A and B at a reference temperature of 45^{o}C, the raw data was manually shifted along the vertical crack propagation rate axis to align with the raw data collected at 45^{o}C for the corresponding solvated hydrogel. This is similar to the method of shifting along the time axis that was used in Chapter 3 in order to construct the master curves of the dynamic moduli, but instead of a horizontal frequency shift, a vertical shift of the crack propagation rate was applied. These subcritical SERR master curves for Hydrogel A and B are presented in Figure 4-33 and Figure 4-34. A reference temperature of 45^{o}C was chosen in order to match the operating temperature of these solvated hydrogels during manufacture of an investigated application. While Figure 4-33 depicts the results for each of the three loading methods used on both material systems as well as a validation of the plane strain condition, Figure 4-34 displays all of the results for both solvated hydrogels performed at various temperature levels.

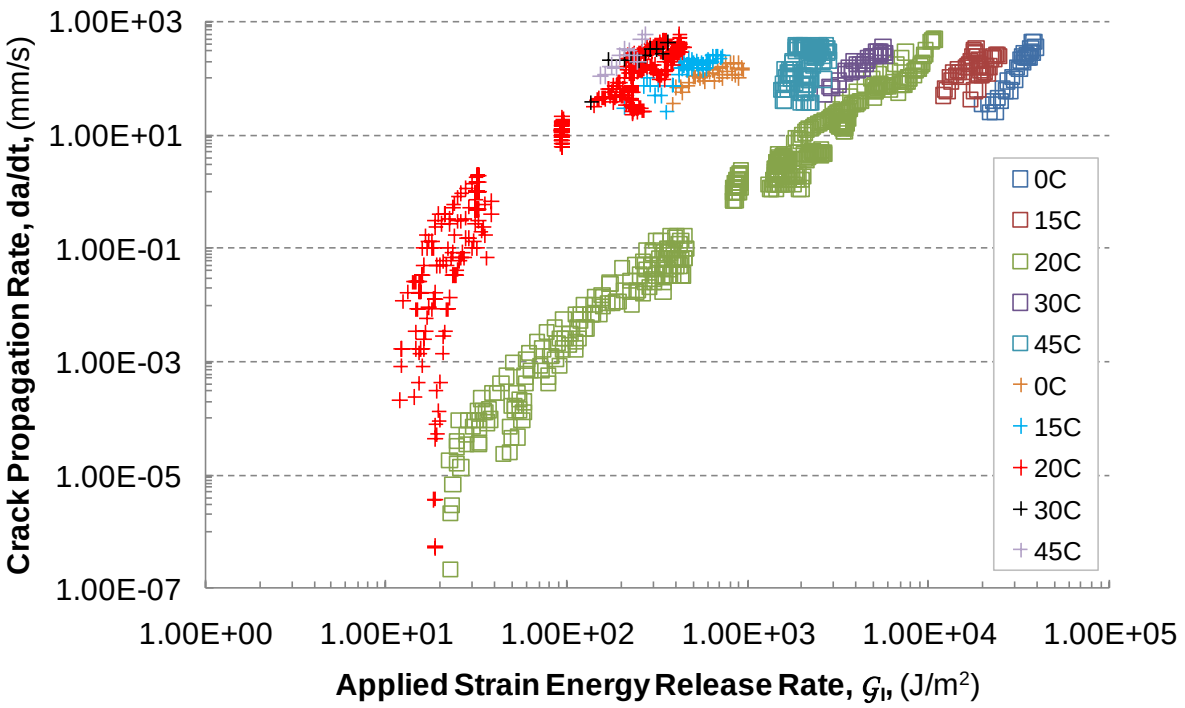

Figure 4-31: Raw or unshifted fracture energy data for Hydrogel A and B

The decreasing strain setup tested on the constrained tension geometry of these solvated hydrogel systems was used to obtain a threshold and lower sub-critical region of the SERR curves that corresponds to slow and arresting crack propagation. The green diamonds for Hydrogel A and green crosses for Hydrogel B represent this threshold and the onset of the sub-critical SERR regions in Figure 4-33. It is interesting to note, but not surprising since these hydrogels consist of similar molecular structures, that these systems have relatively similar intrinsic fracture energy values of approximately 18-22 J/m^2. Further observation of the decreasing strain results indicate that Hydrogel A exhibits an onset of viscoelastic behavior at slower rates than Hydrogel B by as much as three orders of magnitude, as displayed by the knee or bend from the threshold or non-propagating regime into the subcritical region of the SERR curve. Although these results may not directly applicable to industrial manufacturing of applied hydrogels since these results occur at slow rates and manufacturing processes generally occur at relatively fast rates, the decreasing strain results provide confidence in the method used to determine the bulk SERR for these solvated hydrogel systems.

Additionally, scanning electron microscope (SEM) images of the fracture surface of Hydrogel A after one of these decreasing strain fracture tests depicted interesting fracture patterns as the crack length increased. Figure 4-32 (a) shows a smooth fracture surface for a distance of 35-45 along the crack length and Figure 4-32 (b) depicts an angled fracture pattern near the crack tip of the sample at a distance of 115-125 mm

along the crack length. Additional images as well as a possible theory to explain these odd fracture patterns are presented in Appendix F.

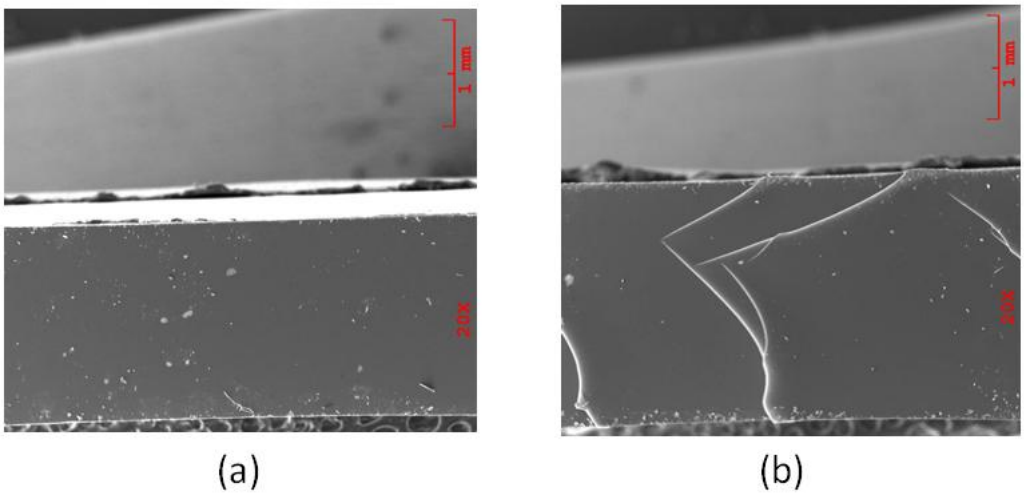

Figure 4-32: Scanning electron microscope images of the fracture surface of Hydrogel A from the decreasing strain case for distances of (a) 35-45mm and (b) 115-125 mm along a 142 mm crack length

The fixed strain and increasing strain test scenarios occurred at higher crack propagation rates and strain energy release rates within the sub-critical region of these curves and are represented by red and blue diamonds, respectively, for Hydrogel A and red and blue crosses, respectively, for Hydrogel B as shown in below in Figure 4-33. This plot shows that Hydrogel A possesses consistently requires higher applied fracture energies to fracture at a given rate, even by as much as a decade greater in some regions, than Hydrogel B throughout this sub-critical region. This phenomenon is further reinforced and understood by the time temperature superposition graphs of the dynamic moduli for Hydrogel A and B provided in Chapter 3, Figure 3-15 and Figure 3-16 , where Hydrogel A was shown to possess greater dynamic moduli compared to Hydrogel B at the rates and temperatures tested. Also, a weak time-dependence was incorporated in the fracture energy calculations for the fixed strain case of Hydrogel A and B by applying the effective moduli, E(t), determined from stress relaxation testing of this constrained tension geometry without an initial crack at corresponding strain levels. Although only a slight decrease in fracture energy was found by incorporating this effective modulus into the fracture analysis as shown in Appendix D, the resulting fracture energy values for Hydrogel A and B still followed the subcritical fracture energy curve created from the results of the increasing and decreasing strain cases. Overall, the results from the increasing and fixed strain methods indicate that Hydrogel A requires greater fracture energy to elicit crack advancement at any given crack propagation rate after deviating from the threshold fracture energy region.

In order to verify that plane strain does not fail for this bulk fracture testing procedure, the effects of thickness were considered by performing an increasing strain fracture test on a Hydrogel A sample with four times the thickness of the normal bulk fracture samples. The results, displayed in Figure 4-33, indicate that the increase in thickness does not suggest failure of plane strain conditions; however, there is a slight increase in the fracture energy achieved by the four times thicker sample compared to the normal samples which may be attributed to an increase in crosslink density as a result of longer UV exposure times needed for the thicker sample or the development of a possible crosslink density gradient through the thickness.

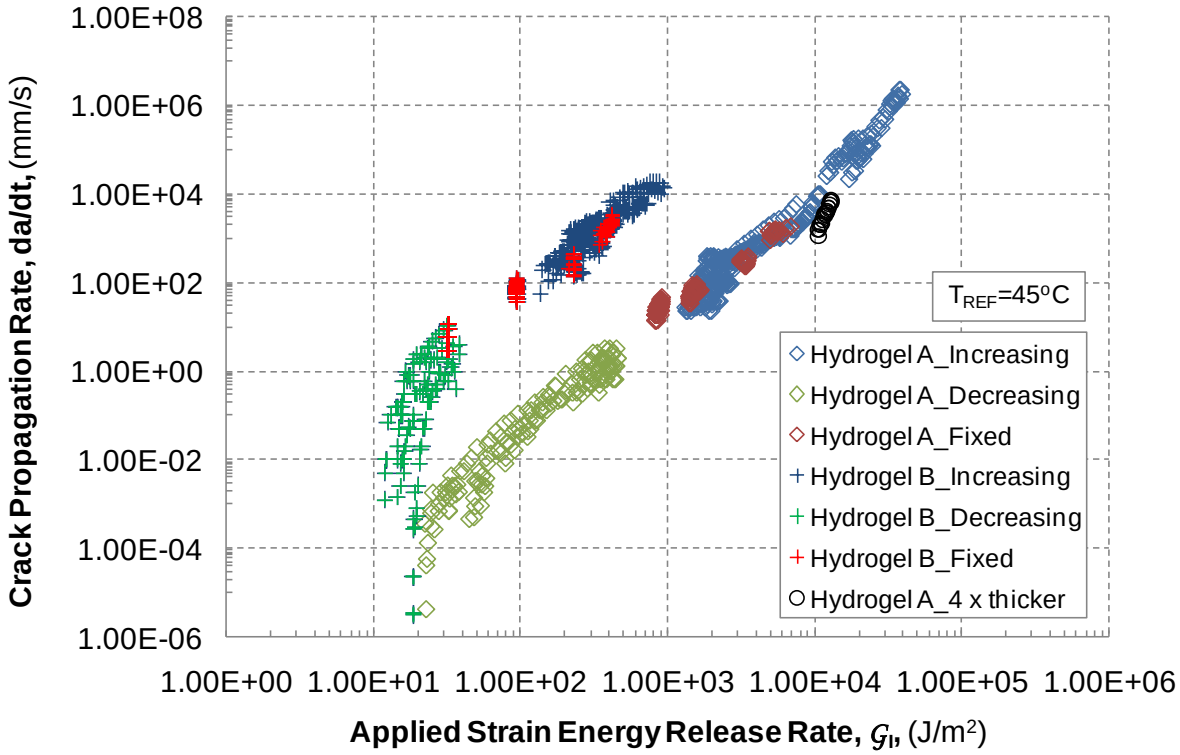

Figure 4-33: Comparison of loading scenarios and subcritical SERR master curves of Hydrogel A and B

Although initial fixed, decreasing, and increasing strain constrained tension fracture tests at ambient temperatures yielded valuable insight into the fracture energies of these systems, additional testing at sub-ambient temperatures of these hydrogel systems was required to further develop the applied SERR curves in order to reach testing rates relevant to industrial applications. Figure 4-34 displays the manually constructed master curves of the applied SERR for Hydrogel A and B at a reference temperature of 45°C. As previously mentioned, sub-ambient temperature testing, such as the 0°C and 15°C tests, extended the SERR curves further into the sub-critical fracture energy region by as much as two orders of magnitude for the crack propagation rate of Hydrogel A and an order of magnitude for Hydrogel B. Although a critical

threshold was not obtained for both Hydrogel A and B by testing at temperatures as low as 0°C, sufficient data was obtained to provide further confidence in this fracture testing method for soft materials as well as provide additional insight into the fracture behavior at high crack propagation rates relevant to industrial processes. Generally, the loss factor term, tan δ, is a good indicator of a material's ability to absorb energy as presented by Pohlit *et al* [54]. By investigating potential correlations between the loss factor and the fracture energy of Hydrogel A and B, dynamic mechanical analysis testing (DMA) could provide insight into fracture energies at lower temperatures where cohesive fracture testing of Hydrogel A and B becomes increasingly difficult to conduct. Furthermore, a correlation between the subcritical fracture energy curves and tan δ values at a reference temperature of 45°C was investigated and is included in Appendix H.

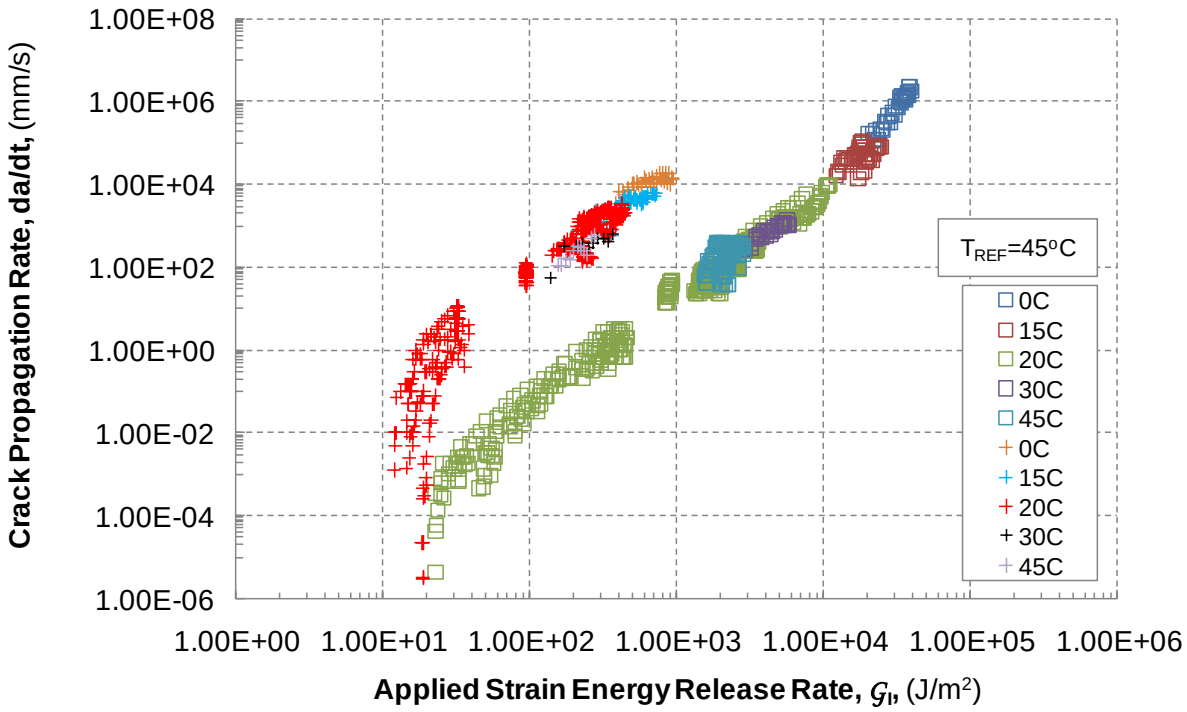

Figure 4-34: Subcritical SERR master curves of Hydrogel A (squares) and B (crosses) at a reference temperature of 45°C

Additionally, the thermal shift factors used to shift the collected fracture data at different temperatures to a reference temperature of 45°C were found to be in good agreement with the WLF fits for Hydrogel A and B obtained from DMA shear testing presented in Chapter 3 as shown in Figure 4-35. Although the DMA shear testing was performed at small strains on the order of 0.1% and fracture specimen experienced intermediate to large strains corresponding to strains of 20 to 80%, these results suggest that similar polymer chain mobility, which is affected by changes in temperature, occurs for both

small and large scale deformations. Similar trends in temperature dependence were observed for the tearing force necessary to promote crack propagation in constrained tension samples of Hydrogel A and B and are presented in Appendix I.

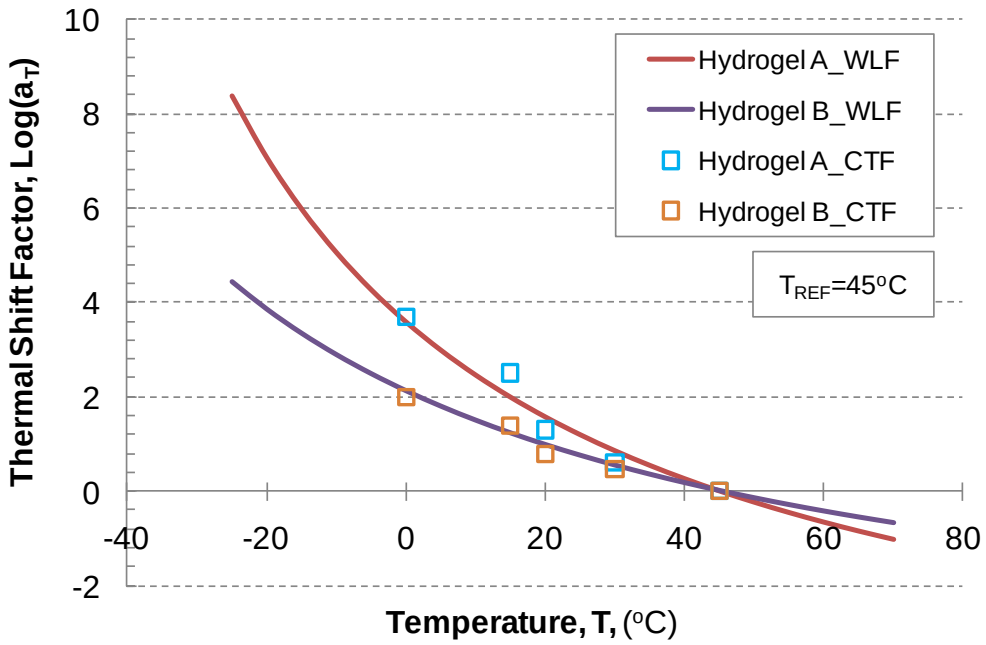

Figure 4-35: Comparison of DMA WLF fits from Chapter 3 and constrained tension fracture thermal shift factors for Hydrogel A and B

A power law equation, Equation (25) , provided by Williams was used to fit the threshold and subcritical SERR regions of SERR master curves at a reference temperature of 45°C for Hydrogel A and B as depicted in Figure 4-36 [39, 43]. In this equation, $\mathcal{G}_o$ corresponds to a threshold fracture energy value representing no crack propagation, v_c represents the crack propagation rate at which viscoelastic effects begin to dominate corresponding to the bend or deviation from the threshold region, and n is the slope of the sub-critical SERR region. Furthermore, Table 4-1provides a comparison of the parameters used to fit the SERR curves of Hydrogel A and B which shows, as discussed earlier, that both systems have similar threshold fracture energies due to their similar molecular characteristics. Also, Hydrogel A breaches into the subcritical SERR region at rates that are approximately three orders of magnitude lower than Hydrogel B, which is consistent with the dynamic mechanical analysis (DMA) shear testing results provided in Chapter 3. The fit for Hydrogel A at this reference temperature begins to degrade as the crack propagation rate reaches 1.00 x 10^4 mm/s, which shows a change in slope of the applied SERR curve's subcritical region corresponding to the onset of a critical threshold applied SERR for Hydrogel A. Additionally, this critical SERR region is captured by performing constrained tension fracture tests at sub-ambient temperatures approaching the glass transition temperature of the material system. In order to fully

characterize the SERR master curves for both Hydrogel A and B, further sub-ambient temperature fracture testing is required which could correspond to the industrial manufacturing rates used to debond hydrogel materials from their manufacturing substrate molds.

$$\mathcal{G}(v) = \mathcal{G}_o\left(1+\frac{v}{v_c}\right)^n \tag{25}$$

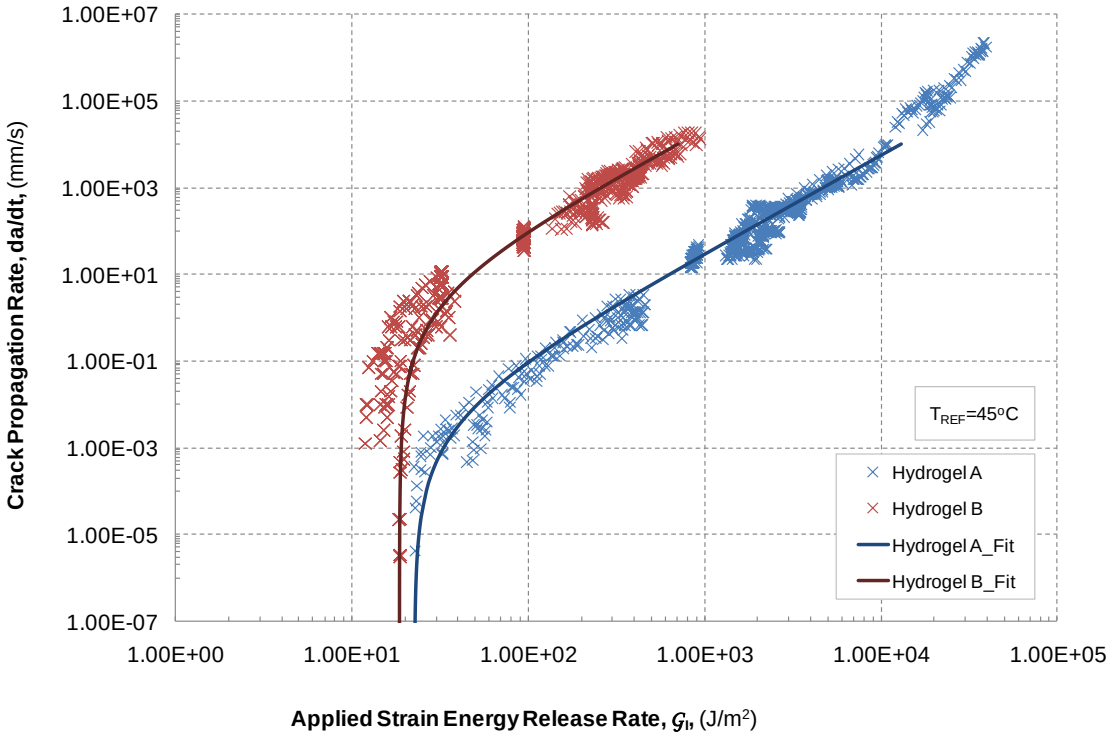

Figure 4-36: Fitted subcritical SERR master curves of Hydrogel A and B

Table 4-1: Parameters used to fit power law equation to Hydrogel A and B

	Hydrogel	
	A	**B**
$\mathcal{G}_o$ (J/m²)	22.8	18.47
v_c (mm/s)	5.62×10^{-3}	3.5
n	0.441	0.456

While Equation (25) includes a dependence on crack propagation rate, *v*, in order to model the subcritical SERR master curves for Hydrogel A and B, Equation (26) was developed in order to incorporated temperature dependence in this expression as suggested by Persson's fracture energy fit in Equation (18) [43].

$$\mathcal{G}(v,T) = \mathcal{G}_o\left(1+\frac{a_T(T)v}{v_c}\right)^n \tag{26}$$

Similar to Equation (25) , $\mathcal{G}_o$ represents the threshold fracture energy at which cracks will not propagate through the material, v_c corresponds to the critical velocity at which viscoelastic effects dominate, and *v* is the crack propagation rate. Temperature dependence is introduced by the thermal shift factor, a_T, which is a function of temperature and is multiplied by the crack propagation rate. For this expression, the William-Landels-Ferry Equation, Equation (8) presented in Chapter 3, was solved for the thermal shift factor and applied to Equation 27. Additionally, this expression requires the experimentally determined WLF coefficients for Hydrogel A and B presented in Table 3-1. Now, Equation (27) includes both crack rate and temperature dependence for a master curve of the subcritical fracture energy of both Hydrogel A and B provided the appropriate material parameters from Table 4-1 and Table 3-1 are applied. Such an equation could prove useful for modeling the behavior Hydrogel A and B for various applications in a finite element based approach.

$$\mathcal{G}(v,T) = \mathcal{G}_o\left(1+\frac{10^{\left(\frac{-C_1(T-T_{ref})}{C_2+(T-T_{ref})}\right)}v}{v_c}\right)^n \tag{27}$$

Comparison of Bulk and Interfacial Fracture Data

While the investigation of the cohesive fracture energy of these hydrogel systems was performed by the author of this thesis and is the focus of this chapter, additional research on the interfacial fracture of Hydrogel A and B cured to a cyclic poly-olefin system was investigated by Murray. For this interfacial case, a simple wedge geometry was implemented which consisted of a thin layer of the cured hydrogel system sandwiched between two rigid cyclic poly-olefin sheets. The collected and analyzed interfacial fracture results are presented and compared to the bulk fracture data in Figure 4-37. While it is difficult to directly compare results of a material for an interfacial fracture case to a bulk fracture case, several statements can be made. The fracture

energy values for the bulk fracture case are shown to be greater than the interfacial due to the greater amount of solvated hydrogel material that must be fractured in the bulk fracture tests. Similar to the bulk fracture energy results, the interfacial fracture data shows that Hydrogel A presents an onset of viscoelastic behavior at slower crack propagation rates compared to Hydrogel B, and Hydrogel A consistently displays greater fracture energies at any given rate within the subcritical fracture region compared to Hydrogel B. Additionally, both interfacial and bulk fracture results indicate that Hydrogel A and B have similar intrinsic fracture energies. Lastly, while both interfacial and bulk fracture results for Hydrogel B do not display a critical fracture energy for the tested temperature ranges, the interfacial results depict a critical fracture energy for Hydrogel A at approximately 17 J/m^2.

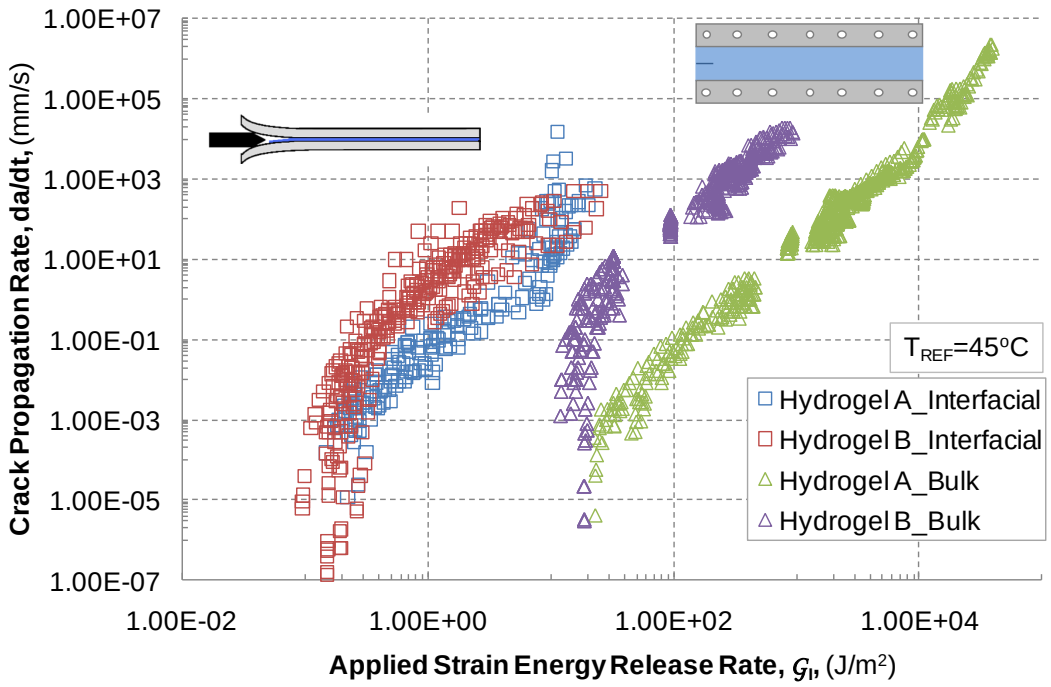

Figure 4-37: Comparison of interfacial (wedge) and bulk (constrained tension) fracture data

Viscoelastic Dissipation in Wake Region of Crack

The crack opening displacement (COD) for constrained tension fracture tests of Hydrogel A operated under fixed strain loading conditions for the cases of 30%, 50%, and 60% strain were plotted against the position along the sample when the crack tip reached 50, 100, and 150 mm in Figure 4-38, Figure 4-39, and Figure 4-40, respectively. These plots were obtained by analyzing the crack profile from high-speed camera images once the crack length reached the 50, 100, and 150 mm positions along the sample. The results for the 30% and 50% strain levels indicate a slight increase in the COD, by as much as 0.8 mm between the 50 mm and the 150 mm cases, along the

first 30 mm of the sample as the crack tip moved from 50 mm to 100 mm and 150 mm, while the 60% did not show this trend which may be a result of error in measuring the COD with MATLAB due to poor image quality. Since the COD is shown to increase within this wake region for the 30% and 50% strain cases, especially once the crack length reaches 150 mm, which is far behind the crack tip, a small strain recovery in the solvated hydrogel material may have occurred. However, this was not confirmed with the highest tested fixed strain case; therefore, further analysis of this method is required in order to determine the resolution of obtaining the COD from the high-speed camera images in MATLAB®. Additionally, when the crack length was shown to reach about 150 mm for all strain cases, an inflection in the COD was observed approximately 50 to 60 mm in the wake of the crack, which is about twice the length of the initial height of the sample, further suggesting possible viscoelastic strain recovery. If this increase in COD could definitely be determined, it would suggest that the steady state fracture analysis used in the above section overestimates the determined fracture energy and a refinement to this analysis would be necessary in order to adjust for the viscoelastic recovery observed in the wake region. Preliminary estimates for the overestimation of fracture energy were approximated to be within the range of 0.5- 2.5 J/m^2 and were determined by estimating the increase in the COD for regions far behind the crack tip and calculating the fracture energy using the equations for the steady state fracture analysis. Based on this approximation, any potential viscoelastic recovery would be deemed negligible in comparison to the subcritical fracture energies observed for Hydrogel A.

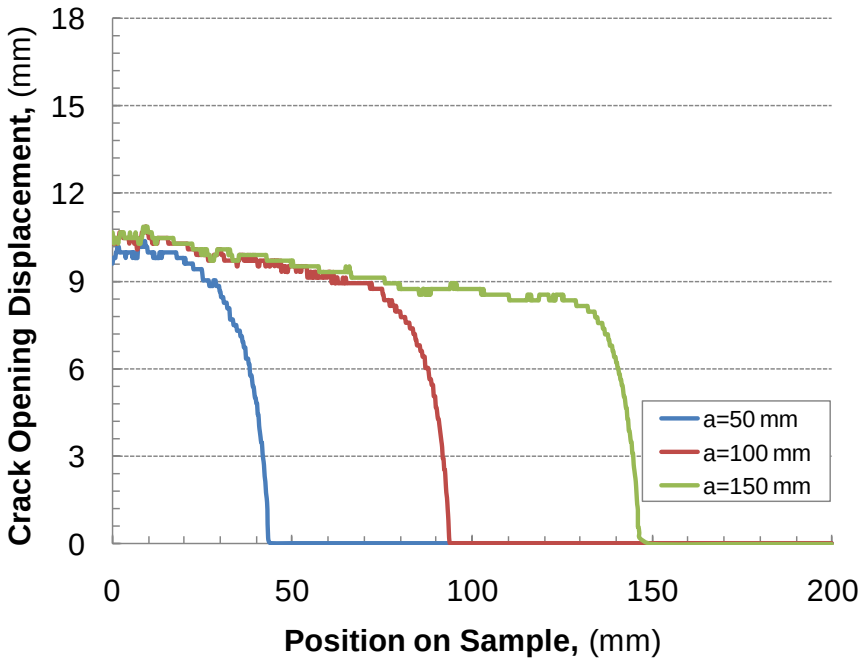

Figure 4-38: Crack opening displacement for 30% fixed strain

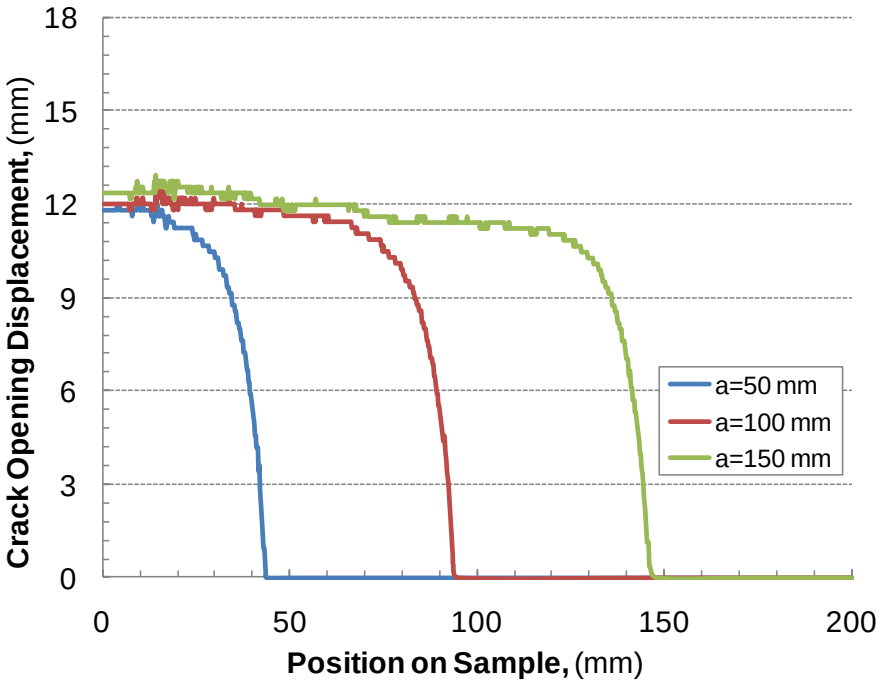

Figure 4-39: Crack opening displacement for 50% fixed strain

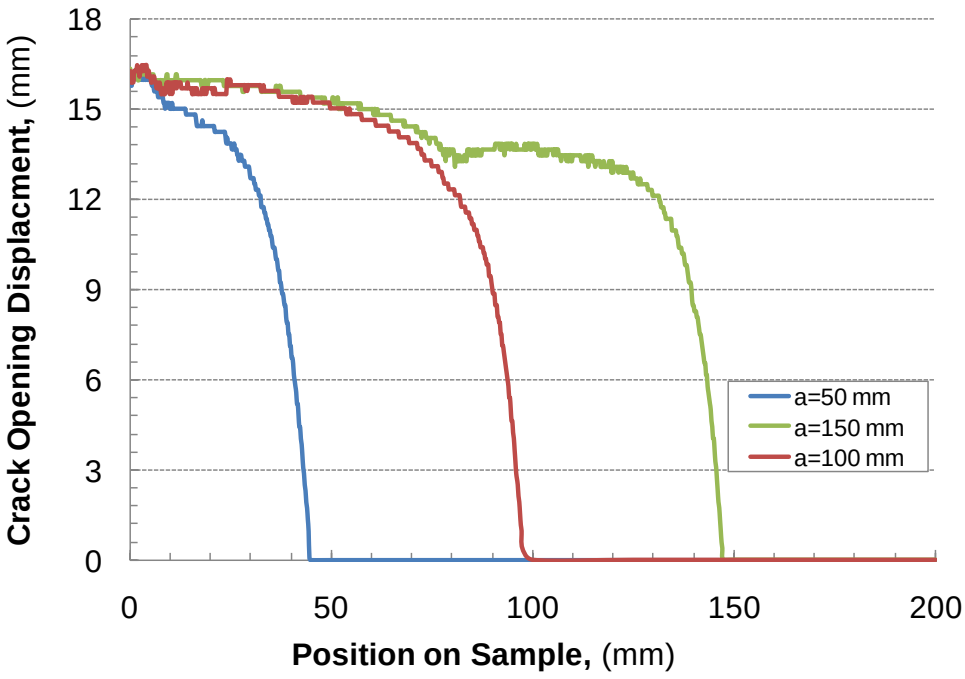

Figure 4-40: Crack opening displacement for 60% fixed strain

Another similar key issue with the results for this investigation into the possible viscoelastic strain recovery of the material in the wake of the propagating crack for Hydrogel A is the relation of the height, h_1 and h_2, of each side of the fractured specimen along the wake region of the crack to the initial height of the sample, h_o. The

sum of the heights for the fractured sections, (h_1+h_2), divided by the initial height of the sample, h_o, should be equal to 1 for regions far behind the crack tip, approximately two lengths of the initial height of the sample, in order to display no permanent deformation or viscoelastic recovery. These results are displayed in Figure 4-41, Figure 4-42, and Figure 4-43 for the fixed strain constrained tension fracture cases of 30%, 50%, and 60%, respectively. Again, for all fixed strain cases, there is no evidence of viscoelastic strain recovery when the crack length reaches approximately 50 mm and 100 mm; however, the results begin to show interesting behavior in the wake region of the crack when the crack length reaches 150 mm. Although the error introduced by measuring the height of these fractured sections using an image analysis program developed in MATLAB® has not be determined, a small inflection approximately 50-60 mm behind the crack tip for when the crack length is approximately 150 mm suggests a slight time-dependence in recovery of Hydrogel A during fracture. This is consistent with the trend observed for the COD in the wake region of the crack presented above which indicated preliminary estimates into the fracture energy associated with the viscoelastic strain recovery to be negligible compared to the recorded subcritical fracture energies for Hydrogel A.

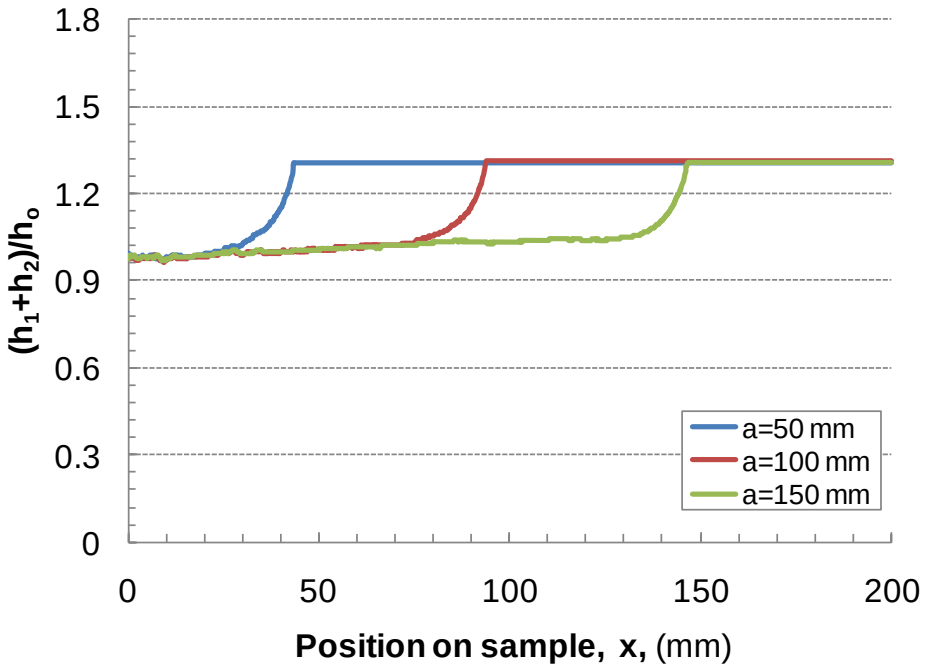

Figure 4-41: Normalized height of material on each side of fractured specimen for 50% fixed strain case

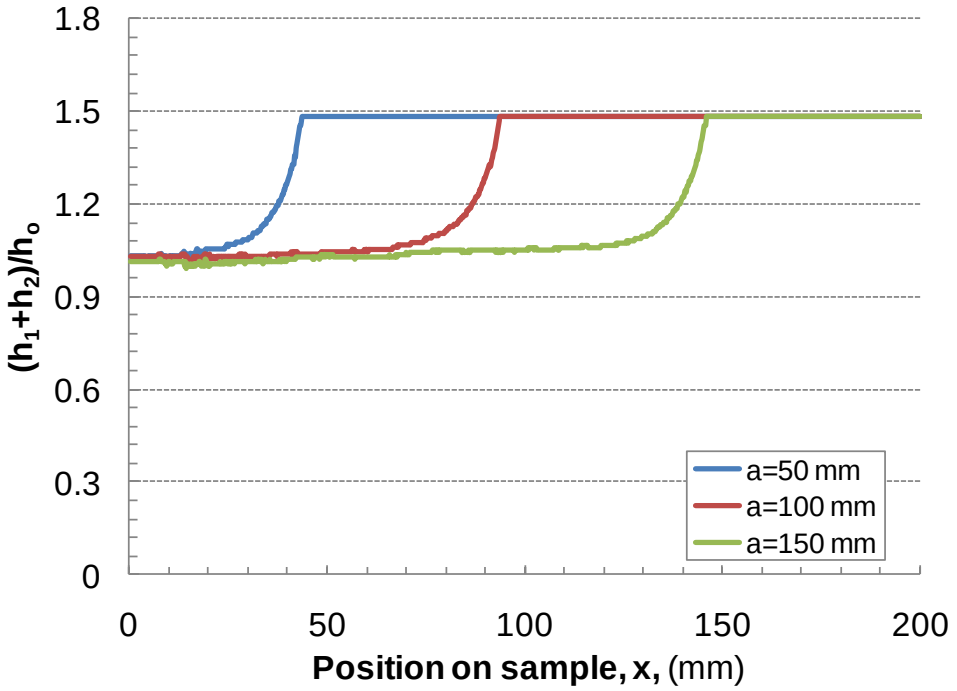

Figure 4-42 : Normalized height of material on each side of fractured specimen for 50% fixed strain case

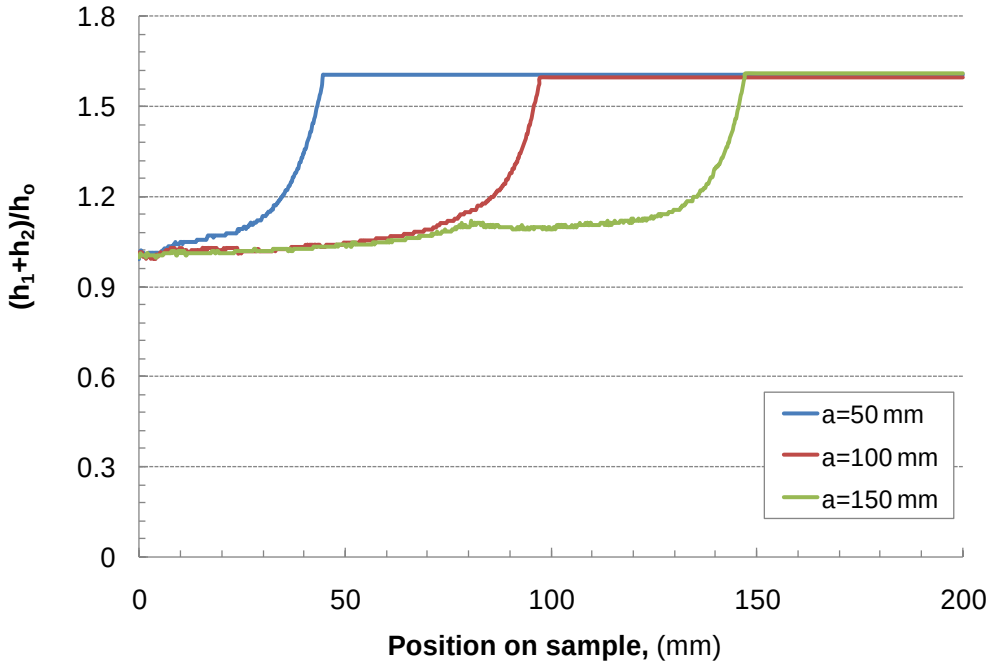

Figure 4-43: Normalized height of material on each side of fractured specimen for 60% fixed strain case

Conclusions

The fracture behavior of the two solvated S-IPN hydrogels investigated in this study were effectively characterized by means of an adapted experimental technique which tested thin sheets of these cured hydrogel systems under mode I fracture using a constrained tension geometry. By utilizing this method with several different loading scenarios such as increasing, fixed, and decreasing strain states, partial SERR master curves for Hydrogel A and B were generated. The analysis of the decreasing strain case for this constrained tension fracture approach provided the threshold corresponding to a region of relatively little to no crack propagation which revealed similar intrinsic fracture energies for Hydrogel A and B as shown in Figure 4-33 and Table 4-1. The fixed and increasing strain cases provided information on the subcritical and near critical behavior of Hydrogel A and B as shown in Figure 4-33. The SERR master curves at a reference temperature of 45^{o}C indicated that Hydrogel A had consistently higher fracture energy by as much as one and a half orders of magnitude in subcritical fracture energy regions beyond the threshold. Additionally, Hydrogel A was shown to display an onset of viscoelastic behavior at crack propagation rates three orders of magnitude slower than Hydrogel B based on the deviation from the non-propagating crack or threshold region. These results are similar to those obtained from DMA shear testing of Hydrogel A and B, displayed in Figure 3-15, where Hydrogel B was shown to be less sensitive to temperature since it was on a rubbery plateau compared to Hydrogel A which is moving out of the rubbery plateau into a transition region for the same frequency and temperature region. Furthermore, thermal shift factors from independently shifting the fracture energies where shown to agree with the WLF fits provided from DMA testing which suggests small and large strain behavior with temperature is similar for these systems.

Although the constrained tension method has been successfully implemented to investigate the fracture energy response of hydrogel systems to rate and environmental conditions, no research on the temperature dependence of the fracture energy for solvated hydrogel systems has been reported. The methods and results from this investigation could be used to understand the behavior of solvated hydrogels, such as Hydrogel A and B, in order to reduce the possibility of defects or fractures during high speed manufacturing processes in controlled environments. For example, Hydrogel B was observed to be less sensitive to changes in the temperatures tested; therefore, Hydrogel B would need to be cooled to lower temperatures in order to possess fracture energies comparable to Hydrogel A at any given rate. Additionally, Hydrogel A's resistance to fracture could possibly make it more favorable and resistant to defects during industrial manufacturing. Also, a study on possible viscoelastic strain recovery in the wake region of the crack for the fixed strain constrained tension fracture of Hydrogel A indicated a slight increase in the crack opening displacement with time. Such results would indicate the occurrence of viscoelastic dissipation which would suggest the

steady state fracture approach overestimates Hydrogel A's fracture energy and requires refinement; however, preliminary estimates indicate negligible overestimation of the fracture energy. Furthermore, an error analysis of the method used to acquire the COD is needed before an exact conclusion can be made. Overall, the constrained tension fracture method performed with several different loading scenarios and across a range of relevant temperatures proved adequate for comparing the viscoelastic fracture behavior of Hydrogel A and B; however, numerical analysis of the mode I fracture approach with finite element software would provide insight into additional refinements to better characterize the fracture behavior of hydrogel systems.

Chapter 5 : Conclusions

Conclusions

This chapter summarizes the key conclusions determined throughout this thesis. It has been broken down to focus on the conclusions made from the investigations conducted on Hydrogel A and B in each chapter of this thesis followed by the overarching conclusions in terms of the impact of solvated hydrogel research on the manufacturing and applications of hydrogel materials.

Chapter 2 was centered on developing an easy and efficient method to cure bulk solvated hydrogel samples with a uniform thickness and determining any critical concerns or considerations for testing solvated hydrogel systems. The major conclusions from this chapter were:

- A five layer sandwich mold consisting of two rigid outer glass layers, two inner layers of polypropylene, and an inner rubber silicone gasket proved to be an adequate method for curing large bulk samples with a uniform thickness for constitutive and fracture testing of these solvated hydrogel systems.
- While solvent ingress of Hydrogel A and B was shown to be negligible due to water immiscible diluents, solvent egress needs to be considered since it can greatly affect material properties.
- Solvated hydrogel samples need to be immediately tested upon curing or stored within their polypropylene molds before testing in order to prevent significant solvent loss.

Chapter 3 was dedicated to investigating the time and temperature dependence of Hydrogel A and B. Both dynamic mechanical analysis (DMA) shear sandwich testing and uniaxial tension testing were conducted over a relevant range of rates and temperatures in order to construct master curves by implementing the time temperature superposition principle (TTSP) and determine essential material parameters. The key conclusions from this chapter were:

- The DMA shear sandwich method is a good technique for characterizing the dynamic moduli and tan δ master curves of solvated hydrogels due to the high degree of repeatability observed for Hydrogel A and B.
- Based on DMA shear results, Hydrogel B was shown to exhibit relatively little to no viscoelastic behavior and be less sensitive to changes in temperature compared to Hydrogel A as shown by the dynamic moduli master curves constructed using TTSP over the tested ranges of rate and temperature.
- Rate and temperature were shown to greatly impact the calculated shear modulus of Hydrogel A for the tested temperatures and rates, while the

calculated modulus for Hydrogel B proved to show little change with temperature and rate.

- Qualitatively, both the small scale strain DMA shear and large scale strain uniaxial tension methods indicated that Hydrogel A was greatly affected by rate and temperature over the tested ranges, while Hydrogel B exhibited a weak or negligible dependence.
- Both WLF and Prony series fits were successfully generated for Hydrogel A and B which can be used for future finite element modeling of these materials.

Chapter 4 was dedicated to investigating the viscoelastic fracture behavior of Hydrogel A and B by means of a constrained tension fracture method typically reserved for elastomeric material systems. Decreasing, increasing, and fixed strain loading methods were developed with this constrained tension geometry to generate subcritical fracture energy – crack propagation rate curves with the increasing strain mode tested over a relevant range of temperatures to determine temperature dependence of the fracture energy for Hydrogel A and B. Additionally, novel methods to investigate the viscoelastic fracture behavior by examining the wake region of a crack propagating through a solvated hydrogel constrained tension sample were pursued. The major conclusions from this chapter were:

- Two solvated S-IPN hydrogels investigated in this study were effectively characterized by means of an adapted experimental technique which tested thin sheets of these cured hydrogel systems under mode I fracture using a constrained tension geometry.
- The decreasing strain loading method proved to be an adequate means of determining the intrinsic or threshold fracture energy for both Hydrogel A and B which were shown to be between 18 and 22 J/m^2. A potential reason for the similarities between these threshold fracture energies are the similar molecular structures of Hydrogel A and B.
- As shown in the subcritical fracture energy master curves, Hydrogel A exhibited the onset of viscoelastic behavior at crack propagation rates nearly three orders of magnitude slower than Hydrogel B.
- Hydrogel A displayed higher fracture energies than Hydrogel B by nearly one and a half orders of magnitude in subcritical fracture energy regions.
- The shift factors used to construct the subcritical fracture energy master curves for Hydrogel A and B were shown to be similar to the shift factors and WLF fits of the dynamic moduli master curves acquired from manually shifting DMA shear testing data.

- Conducting a constrained tension test on Hydrogel A with a specimen that was four times the typical tested thickness demonstrated that plane strain conditions do not fail for this testing procedure used to investigate the fracture behavior of solvated hydrogel systems.
- Temperature dependence was introduced into an equation used to fit the subcritical fracture energy- crack propagation rate curves from this study.
- A slight increase in the crack opening displacement (COD) observed from a time-dependent analysis of fixed strain constrained tension fracture tests of Hydrogel A at ambient conditions suggest possible viscoelastic recovery of the material in the wake region of the crack which may indicate the steady state fracture approach is an overestimate of the fracture energy for Hydrogel A. However, preliminary estimates of this overestimation in fracture indicated negligible values in comparison to the subcritical fracture energies reported for Hydrogel A.
- Although relevant rate and temperature-dependent fracture data was obtained from conducting this constrained tension fracture method under several different loading conditions, the viscoelastic fracture behavior of Hydrogel A and B could be better understood by performing a finite element analysis (FEA) on this constrained tension fracture approach with relevant time and temperature-dependent material properties determined from this study.

Overall, the conclusions deduced from each of the chapters of this thesis provide an assortment of methods to characterize and better understand the constitutive and fracture behavior of solvated hydrogel systems. Conclusions from this solvated hydrogel research that may impact manufacturing and applications of hydrogel systems are:

- Effective characterization of the temperature and time-dependence of solvated hydrogel systems, which are generally made in their applied state within highly controlled environments under high precision and high speed manufacturing processes, was obtained from DMA shear sandwich tests conducted over a relevant range of temperatures and frequencies and the construction of the resulting dynamic moduli and loss factor master curves by utilizing TTSP. This dynamic testing method, compared to methods such as uniaxial compressive or tensile testing, provides a multitude of data over a relatively short period of time, and if applied correctly it can promote a better understanding of the viscoelastic behavior of solvated hydrogels at temperatures and rates applicable to industrial processes in order to identify potential mechanisms responsible for causing material defects and methods to resolve such problems.
- The modified constrained tension fracture methods developed for testing thinly cured sheets of solvated hydrogels provided encouraging preliminary subcritical

fracture energy results when compared with the constitutive behavior of both solvated hydrogel systems which could prove useful for industrial manufacturing of solvated hydrogels for various applications. These results suggest that further analysis and refinements should be applied in order to fully understand and increase confidence in this fracture method; specifically, a finite element based approach which could incorporate the experimentally determined viscoelastic properties of various hydrogel systems.

- While viscoelastic recovery during the constrained tension fracture tests of Hydrogel A operated under fixed strain conditions appeared to be minimal for tested rates and temperatures based on the results of experimental techniques utilizing high-speed images and digital image correlation of the crack propagating through the specimen, finite element analysis of solvated hydrogels are necessary in order to generate a complete understanding of the viscoelastic fracture behavior of these materials.

Future Work

While being one of the first recorded efforts to characterize the bulk viscoelastic fracture behavior of hydrogel systems in their solvated state, this study has provided tremendous insight into the rate and temperature dependence of the constitutive and fracture properties of solvated hydrogels A and B. However, there are several notable areas for refinement of the methods introduced in this study and further *ex-situ* testing of these solvated hydrogels which could enhance the understanding of the behavior of these materials during their manufacture and application. The following are potential items for future work to complete this investigation on the bulk viscoelastic fracture of solvated hydrogels A and B:

- In order to fully understand the bulk viscoelastic fracture behavior of solvated hydrogel systems, such as Hydrogel A and B, and refine the constrained tension fracture analysis for elastomeric materials, a finite element analysis of the constrained tension fracture method operated under the fixed strain condition with the obtained constitutive properties and Prony series and WLF fits, which are needed to model viscoelastic behavior, could be performed. Such a study would greatly strengthen the conclusions of this thesis.

- A study featuring a combination of finite element analysis and a method utilizing digital image correlation (DIC) to observe viscoelastic dissipation and the complex strain region in front of the crack tip for constrained tension fracture samples under fixed strain loading could prove extremely powerful in analyzing the bulk viscoelastic fracture behavior of Hydrogel A and B.

- Further constrained tension fracture testing of Hydrogel A and B at lower sub-ambient temperatures, would generate more fracture energy data that may prove relevant to industrial manufacturing of these systems for various applications and would help to determine the critical fracture energy for Hydrogel A and B.

- Since several different elastomeric material systems, including these solvated hydrogel systems, have shown the ability to shift fracture energies obtained from testing over a range of temperatures to create smooth master curves based on the thermal shift factors obtained from small scale strain testing such as that conducted in a dynamic mechanical analyzer, an investigation into this phenomena for elastomers could prove insightful in terms of similarities between the small and large scale molecular behavior.

- Although efforts were made to investigate a possible correlation between tan δ and fracture energy for both solvated hydrogel systems by implementing a characteristic length equal to the average height of the constrained tension samples, additional methods such as diameter of the caustic during fracture should be investigated as possible options for the characteristic length to reduce crack propagation rate into frequency. If a correlation is found to exist, it could provide a quick and effective means to estimate the fracture energy of a solvated hydrogel system by observing the behavior of the loss factor, tan δ, over a range of temperatures and frequencies.

- An analysis of possible solvent loss during dynamic mechanical analysis (DMA) shear testing despite samples being sandwiched between steel grips could provide greater confidence in the results, or a need for refinement due to solvent loss at higher temperatures.

References

1. Seitz, M.E., D. Martina, T. Baumberger, V.R. Krishnan, C.-Y. Hui, and K.R. Shull, *Fracture and large strain behavior of self-assembled triblock copolymer gels.* Soft Matter, 2009. 5(2): p. 447-456.

2. Anseth, K.S., C.N. Bowman, and L. Brannon-Peppas, *Mechanical properties of hydrogels and their experimental determination.* Biomaterials, 1996. 17(17): p. 1647-1657.

3. Baumberger, T., C. Caroli, and D. Martina, *Fracture of a biopolymer gel as a viscoplastic disentanglement process.* European Physical Journal E -- Soft Matter, 2006. 21(1): p. 81-89.

4. Jind, rcaron, i. Kope, ccaron, ek, and J. Yang, *Hydrogels as smart biomaterials.* Polymer International, 2007. 56(9): p. 1078-1098.

5. Zhao, S.-P., D. Ma, and L.-M. Zhang, *New Semi-Interpenetrating Network Hydrogels: Synthesis, Characterization and Properties.* Macromolecular Bioscience, 2006. 6(6): p. 445-451.

6. *IPNs around the world : science and engineering*, ed. S.C. Kim and L.H. Sperling. Vol. xvi, 294 p. :. 1997, Chichester ; New York :: John Wiley.

7. Sperling, L.H., -, *Interpenetrating polymer networks and related materials*. Vol. xi, 265 p. :. 1981, New York :: Plenum Press.

8. Sperling, L.H., D. Klempner, and L.A. Utracki, *Interpenetrating polymer networks*. 1994, Washington, DC :: American Chemical Society.

9. Han, Y.A., E.M. Lee, and B.C. Ji, *Mechanical properties of semi-interpenetrating polymer network hydrogels based on poly(2-hydroxyethyl methacrylate) copolymer and chitosan.* Fibers and Polymers, 2008. 9(4): p. 393-399.

10. Liu, C., Y. Chen, and J. Chen, *Synthesis and characteristics of pH-sensitive semi-interpenetrating polymer network hydrogels based on konjac glucomannan and poly(aspartic acid) for in vitro drug delivery.* Carbohydrate Polymers, 2010. 79(3): p. 500-506.

11. Webber, R.E., C. Creton, H.R. Brown, and J.P. Gong, *Large strain hysteresis and mullins effect of tough double-network hydrogels.* Macromolecules, 2007. 40(8): p. 2919-2927.

12. CauichRodriguez, J.V., S. Deb, and R. Smith, *Dynamic mechanical characterization of hydrogel blends of poly(vinyl alcohol-vinyl acetate) with poly(acrylic acid) or poly(vinyl pyrrolidone).* Journal of Materials Science-Materials in Medicine, 1996. 7(6): p. 349-353.

13. Brinson, H.F. and L.C. Brinson, *Polymer engineering science and viscoelasticity : an introduction*. 2008, New York: Springer.

14. Ferry, J., *Viscoelastic properties of polymers*. 3rd ed. 1980, New York: Wiley.

15. Wetton, R.E., R.D.L. Marsh, and J.G. Van-de-Velde, *Theory and application of dynamic mechanical thermal analysis.* Thermochimica Acta, 1991. 175(1): p. 1-11.

16. Ward, I.M. and D.W. Hadley, *An introduction to the mechanical properties of solid polymers*. 1993, Chichester ; New York: J. Wiley & Sons.

17. Martínez-Ruvalcaba, A., E. Chornet, and D. Rodrigue, *Viscoelastic properties of dispersed chitosan/xanthan hydrogels.* Carbohydrate Polymers, 2007. 67(4): p. 586-595.

18. Sanabria-DeLong, N., A.J. Crosby, and G.N. Tew, *Photo-Cross-Linked PLA-PEO-PLA Hydrogels from Self-Assembled Physical Networks: Mechanical Properties and Influence of Assumed Constitutive Relationships.* Biomacromolecules, 2008. 9(10): p. 2784-2791.

19. Miquelard-Garnier, G., D. Hourdet, and C. Creton, *Large strain behaviour of nanostructured polyelectrolyte hydrogels.* Polymer, 2009. 50(2): p. 481-490.

20. Lin, W.-C., W. Fan, A. Marcellan, D. Hourdet, and C. Creton, *Large Strain and Fracture Properties of Poly(dimethylacrylamide)/Silica Hybrid Hydrogels.* Macromolecules, 2010. 43(5): p. 2554-2563.

21. Waters, M., R. Jagger, K. Williams, and V. Jerolimov, *Dynamic mechanical thermal analysis of denture soft lining materials.* Biomaterials, 1996. 17(16): p. 1627-1630.

22. Saber-Sheikh, K., R.L. Clarke, and M. Braden, *Viscoelastic properties of some soft lining materials: I--effect of temperature.* Biomaterials, 1999. 20(9): p. 817-822.

23. Shaw, M.T. and W.J. MacKnight, *Introduction to polymer viscoelasticity*. 3rd ed. 2005, Hoboken, N.J.: Wiley-Interscience.

24. Cowie, J.M.G., *Polymers : chemistry and physics of modern materials*. 2nd ed. 1991, Glasgow : New York: Blackie ; Chapman and Hall.

25. Chan, R.W., *Estimation of viscoelastic shear properties of vocal-fold tissues based on time--temperature superposition.* The Journal of the Acoustical Society of America, 2001. 110(3): p. 1548-1561.

26. Sperling, L.H., -, *Introduction to physical polymer science*. 2nd ed. ed. 1992, New York: Wiley.

27. Mark, J.E., A. Eisenberg, W.W. Graessley, L. Mandelkern, E.T. Samulski, J.L. Eoenig, and G.D. Wignall, *Physical properties of polymers*. 2nd ed. 1993, Washington, DC: American Chemical Society.

28. Rubinstein, M., *Polymer physics*, ed. R.H. Colby. 2003, Oxford ; New York: Oxford University Press.

29. Drury, J.L., R.G. Dennis, and D.J. Mooney, *The tensile properties of alginate hydrogels.* Biomaterials, 2004. 25(16): p. 3187-3199.

30. Thornton, J.S., R.E. Montgomery, C.M. Thompson, and D.A. Dillard, *Analysis of interfacial stresses for elastomeric disks in compression.* Polymer Engineering & Science, 1988. 28(10): p. 655-659.

31. Johnson, B., J.M. Bauer, D.J. Niedermaier, W.C. Crone, and D.J. Beebe, *Experimental techniques for mechanical characterization of hydrogels at the microscale.* Experimental Mechanics, 2004. 44(1): p. 21-28.

32. Treloar, L.R.G., *The physics of rubber elasticity*. 3rd ed. ed. Vol. xii, 310 p. :. 2005, Oxford : New York :: Clarendon Press ; Oxford University Press.

33. Smith, T.L., *Deformation and failure of plastics and elastomers.* Polymer Engineering and Science, 1965. 5(4): p. 270-279.

34. Smith, T.L., *Strength of elastorners - a perspective.* Polymer Engineering & Science, 1977. 17(3): p. 129-143.

35. Jackson, A.P., *Measurement of the fracture toughness of some contact lens hydrogels.* Biomaterials, 1990. 11(6): p. 403-407.

36. Shull, K.R., *Fracture and adhesion of elastomers and gels: Large strains at small length scales.* Journal of Polymer Science, Part B: Polymer Physics, 2006. 44(24): p. 3436-3439.

37. Baumberger, T., C. Caroli, and D. Martina, *Solvent control of crack dynamics in a reversible hydrogel.* Nature Materials, 2006. 5(7): p. 552-555.

38. Baumberger, T. and O. Ronsin, *From thermally activated to viscosity controlled fracture of biopolymer hydrogels.* Journal of Chemical Physics, 2009. 130(6): p. N.PAG.

39. Williams, J.G., -, *Fracture mechanics of polymers*. Vol. 302 p. :. 1984, Chichester : New York :: E. Horwood ; Halsted Press.

40. *Engineering with rubber : how to design rubber components*. 2nd ed, ed. A.N. Gent. 2001, Munich : Cincinnati: Hanser ; HanserGardner Publications.

41. Rivlin, R.S. and A.G. Thomas, *Rupture of rubber. I. Characteristic energy for tearing.* Journal of Polymer Science, 1953. 10(3): p. 291-318.

42. Maugis, D. and M. Barquins, *Fracture mechanics and the adherence of viscoelastic bodies.* Phys. D: Appl. Phys. 11, 1978

43. Persson, B.N.J. and E.A. Brener, *Crack propagation in viscoelastic solids.* Physical Review E, 2005. 71(Copyright (C) 2010 The American Physical Society): p. 036123.

44. Tanaka, Y., R. Kuwabara, Y.-H. Na, T. Kurokawa, J.P. Gong, and Y. Osada, *Determination of fracture energy of high strength double network hydrogels.* Journal of Physical Chemistry B, 2005. 109(23): p. 11559-11562.

45. Tanaka, Y., K. Fukao, and Y. Miyamoto, *Fracture energy of gels.* European Physical Journal E, 2000. 3(Compendex): p. 395-401.

46. Kong, H.J. and D.J. Mooney. *Controlling fracture behavior of polymeric hydrogels*. in *Mechanical Properties of Bioinspired and Biological Materials, November 29, 2004 - December 2, 2004*. 2005. Boston, MA, United states: Materials Research Society.

47. Mazich, K.A. and M.A. Samus, *Role of entanglement couplings in threshold fracture of a rubber network.* Macromolecules, 1990. 23(9): p. 2478-2483.

48. Gdoutos, E.E., P.M. Schubel, and I.M. Daniel, *Determination of Critical Tearing Energy of Tyre Rubber.* Strain, 2004. 40(3): p. 119-125.

49. Lake, G.J., Thomas, A.G., *The strength of highly elastic materials.* Proc. R. Soc. Lond., 1967. A(300).

50. Yu, Q.M., Y. Tanaka, H. Furukawa, T. Kurokawa, and J.P. Gong, *Direct observation of damage zone around crack tips in double-network gels.* Macromolecules, 2009. 42(12): p. 3852-3855.

51. Beer, F.P., Johnston II, E. R., and Dewolf, J.T., *Mechanics of Materials*. 4th ed. 2003: McGraw-Hill.

52. Moy, P., Gunnarsson, C.A., Weerasooriya, T., *Tensile deformation and fracture of ballistic gelatin as a function of loading rate.* SEM Conf. Proceedings, 2009(2): p. 848-855.

53. Moerman, K.M., C.A. Holt, S.L. Evans, and C.K. Simms, *Digital image correlation and finite element modelling as a method to determine mechanical properties of human soft tissue in vivo.* Journal of Biomechanics, 2009. 42(8): p. 1150-1153.

54. Pohlit, D.J., D.A. Dillard, G.C. Jacob, and J.M. Starbuck, *Evaluating the Rate-Dependent Fracture Toughness of an Automotive Adhesive.* Journal of Adhesion, 2008. 84(2): p. 143-163.

Appendix A: Solvent Egress Study on Hydrogel A and B

Since preliminary uniaxial tension testing detected a large variation of calculated elastic modulus and stress at break values between newly cured and several day old samples, a solvent loss study was performed on both solvated hydrogel systems in order to determine their sensitivity to ambient conditions as well as to approximate a time frame to test either system before it is declared too old to test. Three 13 mm by 13 mm samples were cut from a 76 mm x 76 mm sheet with a uniform thickness of approximately 1.8 mm for each hydrogel system. Samples were placed on individual glass slides with both 13 mm sides exposed to the ambient environment to promote a two sided diffusion while stored at ambient conditions of approximately 22^{o}C and 30% RH. The mass of the samples was measured periodically over the period of two months using a

The results from this solvent egress study, shown in the Figure A-1 below, indicate that Hydrogel A is much more sensitive to solvent loss than Hydrogel B when stored at ambient conditions, since Hydrogel A lost all of its solvent, 22% by weight, within 400 hours. Additionally, it was decided that Hydrogel A samples could be stored up to one day after being removed from its polypropylene encasement before testing and Hydrogel B samples could last nearly three days, since five percent drop in solvent was detected after 24 hours for Hydrogel A and 120 hours for Hydrogel B.

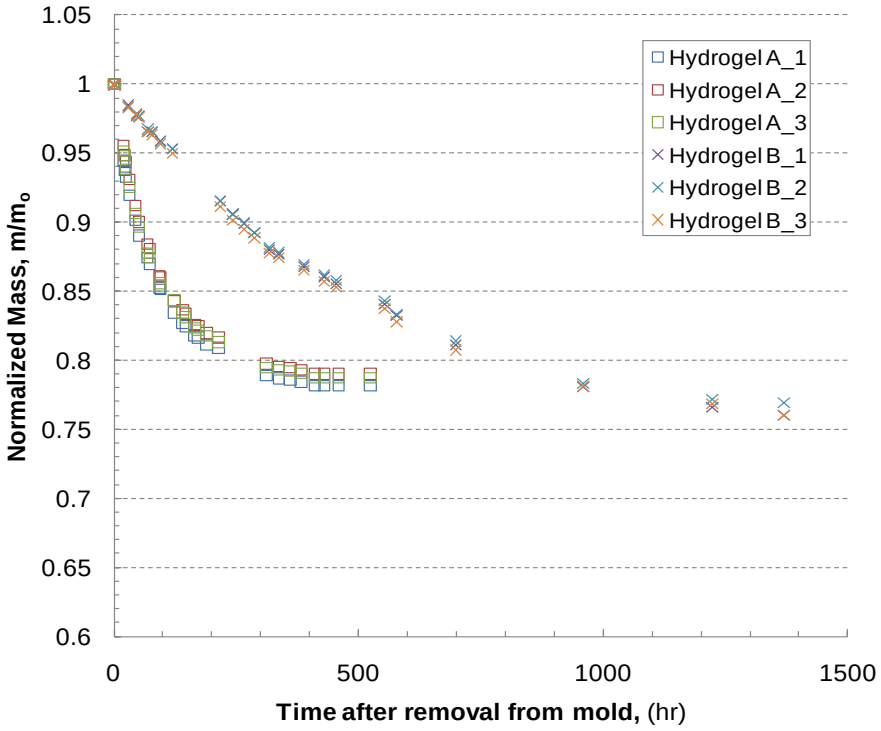

Figure A-1: Solvent egress of Hydrogel A and B over time after demold

Appendix B: Prony Series Characteristic Time and Material Coefficient Values for Dynamic Moduli Master Curves of Hydrogel A and B

The following tables provide the characteristic time values and material coefficients needed to construct the Prony Series fits for all trials of the dynamic moduli master curves for Hydrogel A and B. Two characteristic time values per decade were taken for Hydrogel A and one characteristic time value per decade was used for Hydrogel B.

Prony Series parameters for the storage modulus of Hydrogel A

Characteristic Time Value, τ_i, (s)	**Material Coefficient, G_i,** (MPa)		
	Trial 1	**Trial 2**	**Trial 3**
1.00E-10	2.1973	2.18312	2.1831
3.16E-10	4.6398	4.53429	4.5343
1.00E-09	14.441	14.0842	14.084
3.16E-09	4.1515	3.60747	3.6069
1.00E-08	0.2377	0	0
3.16E-08	6.3854	5.8744	5.8284
1.00E-07	4.5971	4.02575	3.8529
3.16E-07	3.8643	3.39223	3.0207
1.00E-06	5.182	4.75827	4.162
3.16E-06	3.6871	3.70203	2.9109
1.00E-05	2.2735	2.77543	1.8753
3.16E-05	2.7526	3.38598	2.5572
1.00E-04	0.4939	1.07793	0.4583
3.16E-04	1.108	1.46066	1.1334
1.00E-03	0.2692	0.43785	0.3261
3.16E-03	0.3859	0.39027	0.3599
1.00E-02	0.0737	0.16293	0.1148
3.16E-02	0.1247	0.13338	0.1387
1.00E-01	0.0329	0.03817	0.0541
3.16E-01	0.0413	0.04173	0.0579
1.00E+00	0.0175	0.03295	0.0088
3.16E+00	0.0067	0	0.0371
1.00E+01	0.0141	0.00808	0.0007
3.16E+01	0.0006	0.00402	0.0141
1.00E+03	0.1186	0.04483	0.1299
3.16E+03	9E-07	0.00362	7E-08
1.00E+04	9E-07	0.00363	9E-07

3.16E+04	5E-07	0.00362	4E-07
3.16E+04	8E-07	0.00218	4E-07
1.00E+05	0	0.00218	1E-06
3.16E+05	9E-07	0.00219	7E-07
1.00E+06	7E-07	0.0065	3E-07
3.16E+06	9E-07	0.00879	0
Infinite	0.0088	0.03297	0

Prony Series parameters for the loss modulus of Hydrogel A

Characteristic Time Value, τ_i, (s)	**Material Coefficient, G_i,** (MPa)		
	Trial 1	**Trial 2**	**Trial 3**
1.00E-11	2.0521	X	X
3.16E-11	2.0346	X	X
1.00E-10	1.9565	1.9778	1.092157
3.16E-10	3.8939	3.9221	1.716887
1.00E-09	12.366	12.259	9.412249
3.16E-09	2.6422	0	0.171068
1.00E-08	2.5037	3.4919	4.534747
3.16E-08	5.5461	3.7763	4.433287
1.00E-07	4.0191	4.2491	3.891325
3.16E-07	5.449	5.1074	4.042659
1.00E-06	4.8432	4.9935	4.20034
3.16E-06	4.1962	3.8681	2.7194
1.00E-05	4.0137	3.8056	3.489711
3.16E-05	2.8186	1.9828	1.422544
1.00E-04	1.5932	2.4527	1.692084
3.16E-04	0.8674	1.1103	0.368865
1.00E-03	0.8056	0.709	0.871697
3.16E-03	7E-05	0.4151	0.224212
1.00E-02	0.2635	0.1611	0.1447
3.16E-02	0.0139	0.0644	0.147563
1.00E-01	0.106	0.0834	0.064678
3.16E-01	0.001	0.0249	0.019634
1.00E+00	0.0353	0.0261	0.059551
3.16E+00	0.009	0.0144	0

1.00E+01	0.0058	0.0038	0.020684
3.16E+01	0.0111	0.0131	0.009673
1.00E+03	5E-06	0.0461	0.035952
3.16E+03	0.0302	0	0
1.00E+04	9E-07	6E-07	6.43E-07
3.16E+04	5E-07	2E-07	2.03E-07
3.16E+04	8E-07	2E-07	2.03E-07
1.00E+05	0	6E-08	6.43E-08
3.16E+05	9E-07	0.0936	0.05153
1.00E+06	7E-07	0.4434	0.430021
3.16E+06	9E-07	2E-09	0.243354
1.00E+07	2E-06	X	X
3.16E+07	9E-07	X	X

Prony Series parameters for the storage modulus of Hydrogel B

Characteristic Time Value, τ_i, (s)	**Material Coefficient, G_i,** (MPa)		
	Trial 1	**Trial 2**	**Trial 3**
1.00E-10	4.1098	4.109796	4.1098
1.00E-09	4.1098	4.109793	4.1098
1.00E-08	4.1096	4.109479	4.1095
1.00E-07	4.0897	4.077826	4.0776
1.00E-06	3.4776	3.05596	3.048
1.00E-05	0.4615	0.412632	0.386
1.00E-04	0.1954	0.205035	0.1588
1.00E-03	0.0612	0.059229	0.036
1.00E-02	0.02	0.016313	0.0124
1.00E-01	0.0042	0.005328	3E-05
1.00E+00	0.0016	0	0.0021
1.00E+01	4E-05	0.001928	2E-05
1.00E+03	0.0177	0.018881	0.0159
1.00E+04	0.0135	0.015839	0.0129
1.00E+05	0.0136	0.01627	0.0203
Infinite	0.0083	0.008892	0.0098

Prony Series parameters for the loss modulus of Hydrogel B

Characteristic Time Value, τ_i, (s)	**Material Coefficient, G_i,** (MPa)		
	Trial 1	**Trial 2**	**Trial 3**
1.00E-10	4.1095	4.1094	4.1098
1.00E-09	4.1072	4.1056	4.1098
1.00E-08	4.0795	4.064	4.1095
1.00E-07	3.841	3.6696	4.0776
1.00E-06	1.4666	1.5557	3.048
1.00E-05	0.653	0.6506	0.386
1.00E-04	0.1783	0.1962	0.1588
1.00E-03	0.0645	0.0623	0.036
1.00E-02	0.0166	0.0172	0.0124
1.00E-01	0.0035	0.0037	3E-05
1.00E+00	0.0013	0.0014	0.0021
1.00E+01	0.0007	0.0008	2E-05
1.00E+03	0	4E-09	0.0159
1.00E+04	0	4E-10	0.0129
1.00E+05	0.0125	0.0125	0.0203
Infinite	0.0011	0.001	0.0098

Appendix C: Details on Custom-Made Environmental Chamber

This environmental chamber, presented in Figure C-1 and Figure C-2, was constructed in order to perform testing of temperature-dependent material systems, such as these solvated hydrogel systems, on the Instron® MicroTester 5848 in its vertical configuration over a range of temperatures from -25^{o}C to 150^{o}C. The research contained in this thesis used this environmental chamber for both uniaxial tension and constrained tension fracture testing over a range of temperatures. While this temperature range was based on the specifications of the recirculating water bath (Cole-Parmer® Polystat® 6-liter refrigerated circulating water bath) used to control the temperature within the chamber, actual temperatures within the chamber during testing have only been performed between -15^{o}C to 80^{o}C and required certain temperature offsets in order to reach desired temperatures. As for the components of this environmental chamber, the main chamber is a polycarbonate electrical box (FIBOX ARCA®) with a side-hinged transparent polycarbonate front panel with two latches to tightly seal the container. A 50 mm diameter hole was drilled into both the top and bottom of the polycarbonate box. Both holes were aligned appropriately so that the actuator and grips could pass through as needed during testing. Two additional 25mm diameter holes were drilled into the left side of the chamber in order to pass two 12.5 mm ID rubber silicone fiber reinforced tubes which connected the previously mentioned recirculating water bath to a copper aluminum finned heat exchanger. A small computer fan was mounted next to the heat exchanger in order to provide convection within the chamber. The insulation consisted of 25 mm thick mineral wool sheets cut to cover the entire interior of the chamber and 25mm thick closed-cell tubing insulation covering the rubber silicone tubing from the water bath to the chamber.

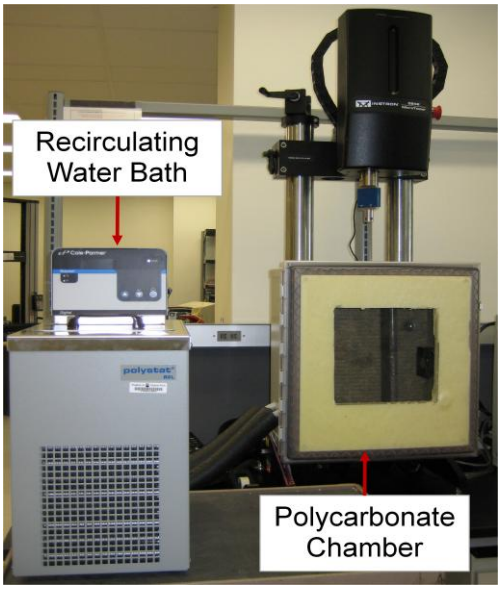

Figure C-1: Environmental chamber setup

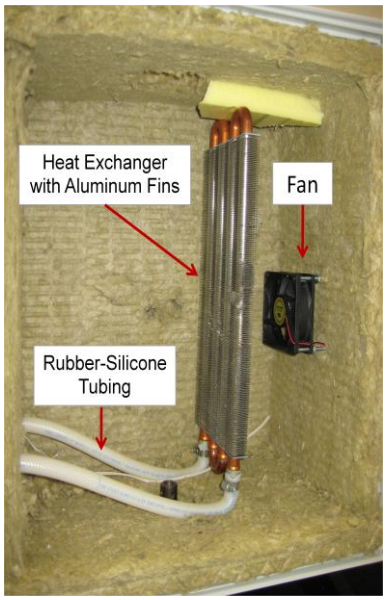

Figure C-2: Interior of environmental chamber

Appendix D: Effective Modulus Results for the Fixed Strain Fracture Method

An example of the stress relaxation curves used to generate an effective modulus for the fixed strain constrained tension fracture tests discussed in Chapter 4 at several strain levels for Hydrogel A and B are presented below in Figure D-1 and Figure D-2, respectively. These plots only show the stress relaxation curve after the initial ramp to the prescribed strain levels. Based on these representative graphs for stress relaxation of Hydrogel A and B, Hydrogel A displayed a consistent 28% decrease in the relaxation modulus during the duration of the conducted tests for all strain levels, while Hydrogel B displayed approximately a 7-8% drop in relaxation modulus from the peak value to the end of test value. This suggests that Hydrogel A displays more of a relaxation after being loading to the prescribed strain level, thus more energy is dissipated during the relaxation tests for Hydrogel A than Hydrogel B which is consistent with the results shown for the viscoelastic behavior for Hydrogel A and B in Chapter 3. Also, this may help to explain the slight slope observed for the fracture energy values of Hydrogel A which was not observed for Hydrogel B. Additionally, the power law fits for the sample relaxation curves are posted on these plots and these were the equations that replaced the elastic modulus value as an effective modulus which decreased with time.

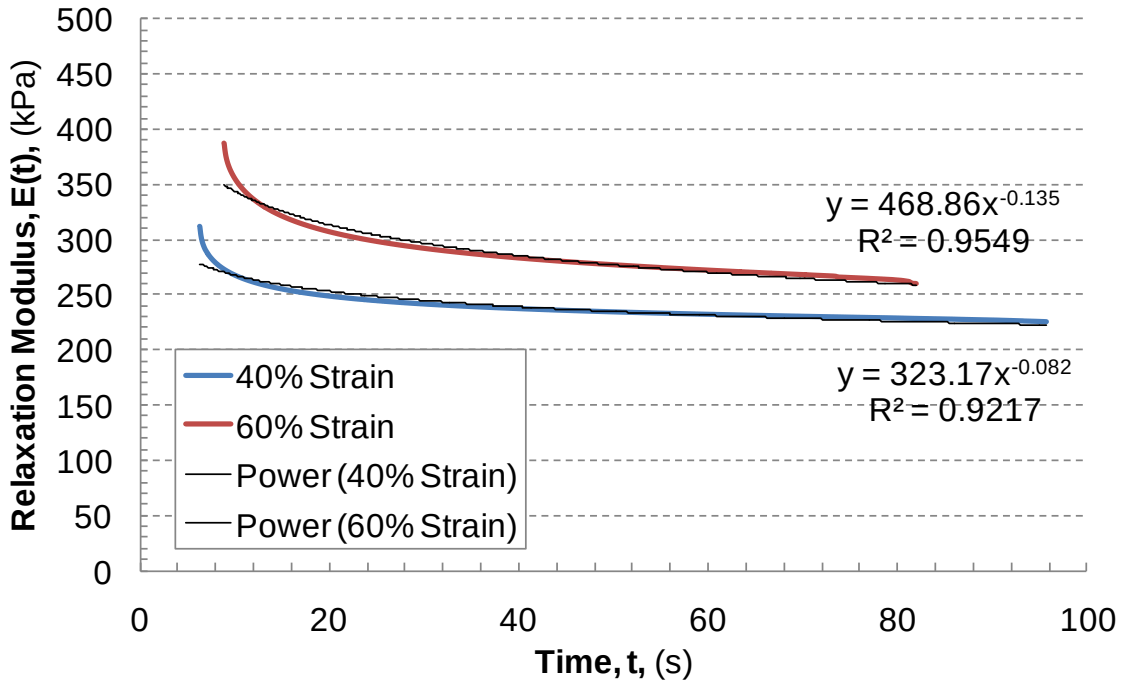

Figure D-1: Example of stress relaxation curves for Hydrogel A

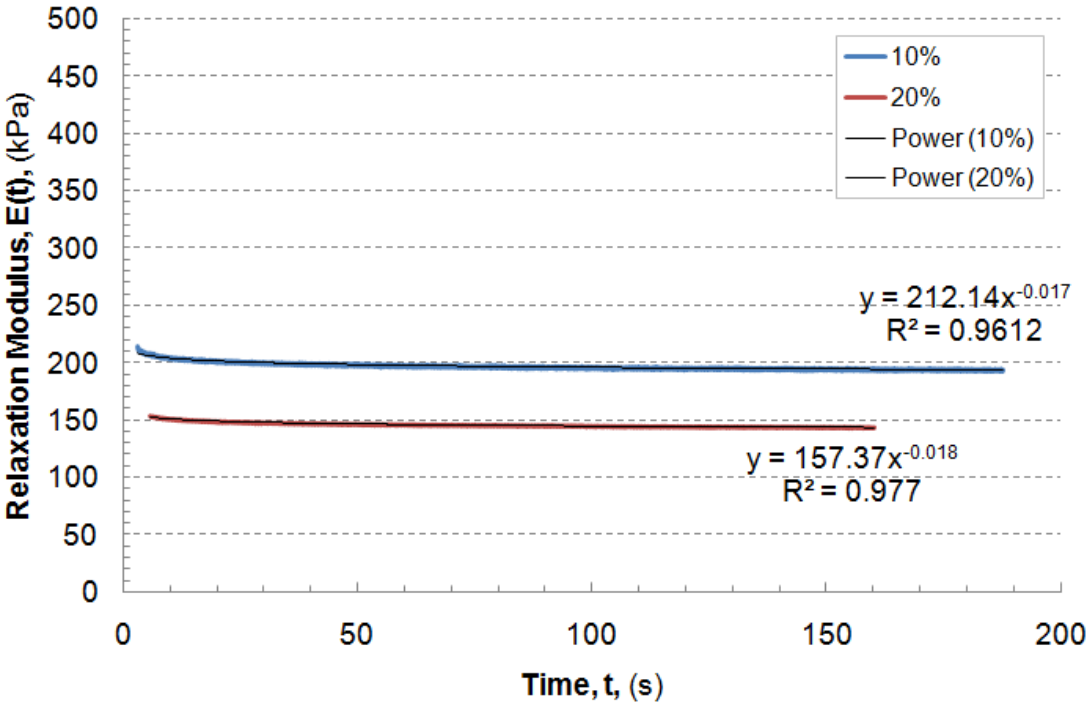

Figure D-2: Example of stress relaxation curves for Hydrogel B

Appendix E: MATLAB Crack Tracking Program for Constrained Tension Fracture

This code was developed in order to process images of constrained tension fracture samples recorded from a high-speed camera, stored as TIFF files, in order to determine the crack length, propagation rate, and the corresponding fracture energy at each instant in time. This code requires several parameters such as the high-speed camera frame rate, the initial sample dimensions, and the total number of images to be processed. Additionally, a CSV file of the load, displacement, and time from the Instron are required to complete a full analysis. Original images are converted into binary in order to distinguish between the crack area and the sample area as shown in the middle image of Figure 4-19. In order to get a clear binary image sometimes the intensity needs to be adjusted. A pixel associated with the perimeter of the crack is selected from the binary image and used to find the entire crack perimeter which is recorded by pixel location with the top left corner of the image being the origin. The pixel furthest to the right is declared the crack tip and is used to determine the crack length after selecting two known points on the original image as a reference length to convert from pixels to mm.

Below is an example of the crack tracking program developed in MATLAB® used to process and analyze images of the crack growth in a constrained tension fracture sample of Hydrogel A.

```
% Created by Geoff Tizard, 5/11/09

% This program is designed to process images saved as TIF files to track
% the crack propagation of a single notched clamp specimen.
%-------------------------------------------------------------------------
clear all
close all
clc
q=1;
%****NOTE****: User needs to consider changing loop length, image loading
values, perimeter
                %start position, and b/w intensity level. Do not always need
to change.
                %Need to know fps used for camera and correlation with
                %Instron data as well as sample dimensions.
%Intensity Settings to obtain appropriate contrast
iten(1:6000)=200;
iten(6001:6300)=175;
iten(6301:6600)=165;
iten(6601:6900)=120;
iten(6901:7200)=125;
iten(7201:7500)=105;
iten(7501:7800)=90;
iten(7801:8100)=70;
iten(8101:8400)=55;
iten(8401:8472)=45;
```

```
%Frame step and frames per second:
fps=3000;
frame_step=300;

%Sample dimensions (clamped plate):
lo=196;to=1.7;ho=27; % dimensions in mm length, thickness, width

for count=1:frame_step:8401% loop for images 1 to end
    % Call image to be processed----------------------------------
    % Load Image:
    second=sprintf('%06s',num2str(count));% sprintf(pad with 6 zero
charaters,convert a number to a string)
    f_name=strcat('pic_',second,'.tif');%creates string for file name of each
TIF frame
    im1=imread(f_name);% reads image from corresponding file name
figure(1), imshow(im1)
%     %crop (optional)
%     im2=im1(85:336,49:997);%im1(x:y,x:y)
%     figure(2),imshow(im2)
%
%     im2_a=im2;
%
%     figures
%     imshow(im2_a)
%     [x,y]=getpts(1
    % threshold/binarize original image using normalized image intensity
    im4 = im2bw(im1,iten(count)/255); % converts image to black and white
***adjust
    figure(2);imshow(im4)

    BW2 = bwperim(im4); %finds perimeter of binary image
    figure(3);imshow(BW2)


    boundary= bwtraceboundary(im4,[250 1],'S',8,inf);%Trace object in binary
image at a start point, direction, all points
    s_boundary_temp=size(boundary);
    s_boundary(1,q)=s_boundary_temp(1,1);
    crack_area(:,q)=bwarea(BW2);

    %%%% track crack tip in time
    x_tip=max(boundary(:,2));
    y_temp=find(boundary(:,2)==x_tip);
    y_tip=min(boundary(y_temp,1));
    crack_tip_x(:,q)=x_tip;
    crack_tip_y(:,q)=y_tip;

    figure(4);imshow(im4)

    figure(5);imshow(im1)
    hold on;
    plot(boundary(:,2),boundary(:,1),'r','LineWidth',2);
    hold on
    plot(crack_tip_x(q),crack_tip_y(q),'bo')
```

```
    close all
    q=q+1;
end
% Get points for pixel to length conversion:
figure(1),imshow(im1)%displays image
[x_pix,y_pix]=getpts(1);% can specify points with mouse from figure 1

%Conversion from pixels to length-------------------------------------
delta_pix=x_pix(2)-x_pix(1);
con_val=(10/delta_pix);%millimeters per pixel
crack_tip_xreal=con_val*crack_tip_x;

%Load Instron Data----------------------------------------------------
Instron_data=csvread('Test1.csv');% Time, Extension, Load
Strain=Instron_data(:,2).*(1/ho);
lambda1=1+Strain(:,1);
lambda2=lambda1(:,1).^-1;
lambda3(1:length(lambda1),1)=1;
Emod=368; %elastic modulus, kPa
for i=1:length(lambda1)
    Uo(i,1)=(1/6)*Emod*((lambda1(i).^2)+(lambda2(i).^2)+(lambda3(i).^2)-3);
end
G=Uo(:,1)*ho*(1/1000);
frame_no=1:frame_step:8401;
Time=frame_no*(1/fps);
deltaT(1,1:length(Time))=Time(1,2)-Time(1,1);

for j=1:length(crack_tip_xreal)-1
    crackrate(j,1)=(crack_tip_xreal(1,j+1)-crack_tip_xreal(1,j))/deltaT(j);
end
% Plots----------------------------------------------------------------
figure(2);plot(frame_no,crack_tip_xreal,'o');ylabel('Crack Length, a,
(mm)');xlabel('Frame Number');
figure(3);plot(Time,crack_tip_xreal,'o');ylabel('Crack Length, a,
(mm)');xlabel('Time, t, (s)');
figure(4);loglog(G,crackrate(1:length(crackrate)-1,1),'o');xlabel('Strain
Energy Release Rate, G_I, (kJ/m^2)');
ylabel('Crack Propagation Rate, da/dt, (mm/s)');
figure(5);plot(crack_tip_xreal(1,1:length(crackrate)),transpose(crackrate),'o
');xlabel('Crack Length, a, (mm)');
ylabel('Crack Propagation Rate, da/dt, (mm/s)');
tTime=Time';
cracklength=crack_tip_xreal';
```

Appendix F: SEM Images of the Fracture Surface of Hydrogel A

A Hydrogel A decreasing strain constrained tension fracture sample was strained on the pre-cracked end to approximately 20% strain as discussed in Chapter 4. After the crack propagation was observed over a period of 10 days, five 10 mm segments along one of the fracture surfaces were removed using a razor blade. Each segment represented a certain portion of the crack length and a corresponding crack growth rate. Scanning electron microscope (SEM) images of the surfaces were taken at a 20x magnification and are shown below in Figure F-1. The top edge of the fracture surface as shown in the decreasing strain setup diagram was the crack surface that was imaged. The first two images of the fracture surface corresponding to 10-20 mm and 35-45 mm depict a relatively smooth fracture surface, while the third figure corresponding to approximately 87-97 mm represents more of a brittle tearing. The final two images begin to show angled grooves along the fracture surface which are not consistent with slow crack propagation rate fractures. Since the sample was exposed to ambient conditions over a period of 10 days, significant solvent egress from the sample occurred and may have contributed to the drastic change in fracture surface along with the decrease in crack propagation rate.

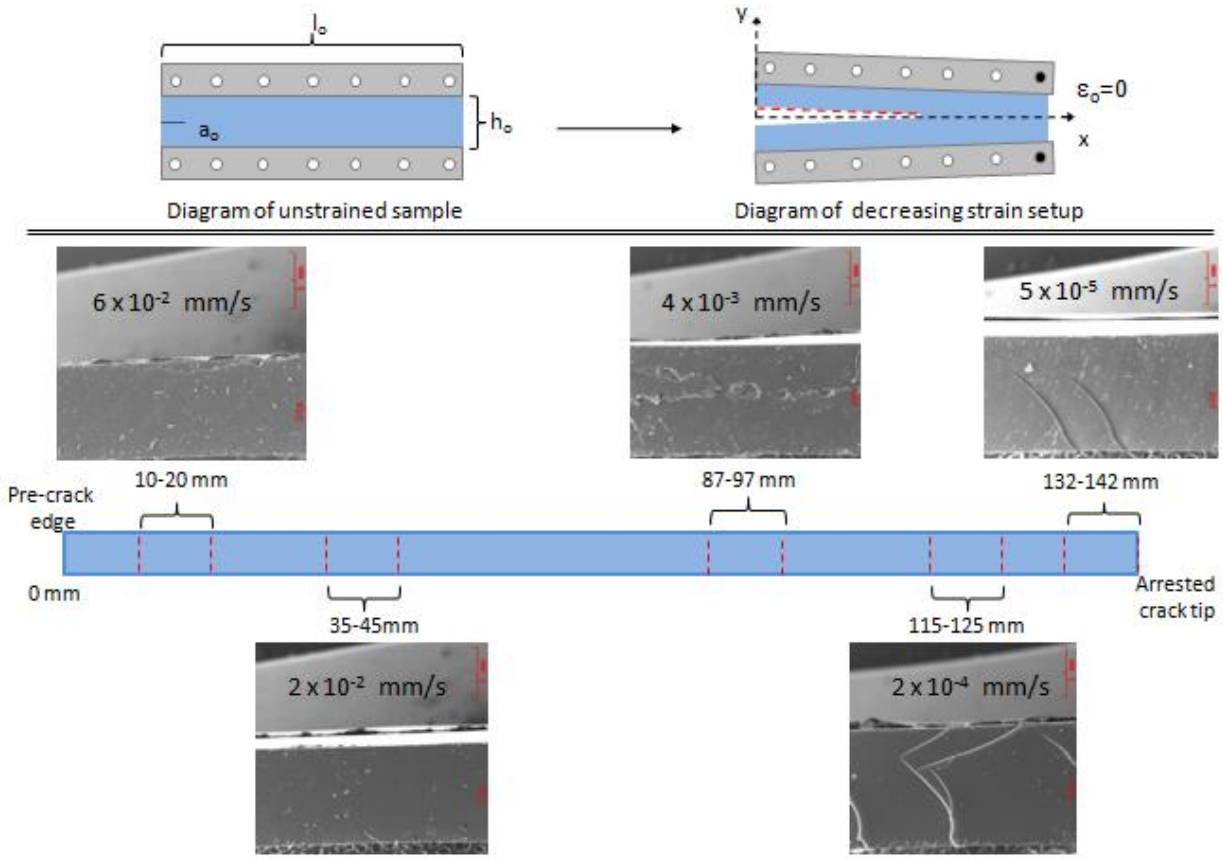

Figure F-1: Complete diagram of SEM images of Hydrogel A fracture surface

Appendix G: Digital Image Correlation (DIC) Technique to Investigate Time-Dependent Fracture Results

Figure G-1 presents several images of the strain level in the Y-direction on a constrained tension fracture sample placed under a fixed strain loading of 50% strain. These images provide insight into both the process zone of the material as well as the behavior of the material in the wake region of the propagating crack. Further, analysis of these results could provide refined estimates as to the degree of viscoelastic strain recovery which was also observed from analyzing images acquired by the highspeed camera used to monitor crack propagation.

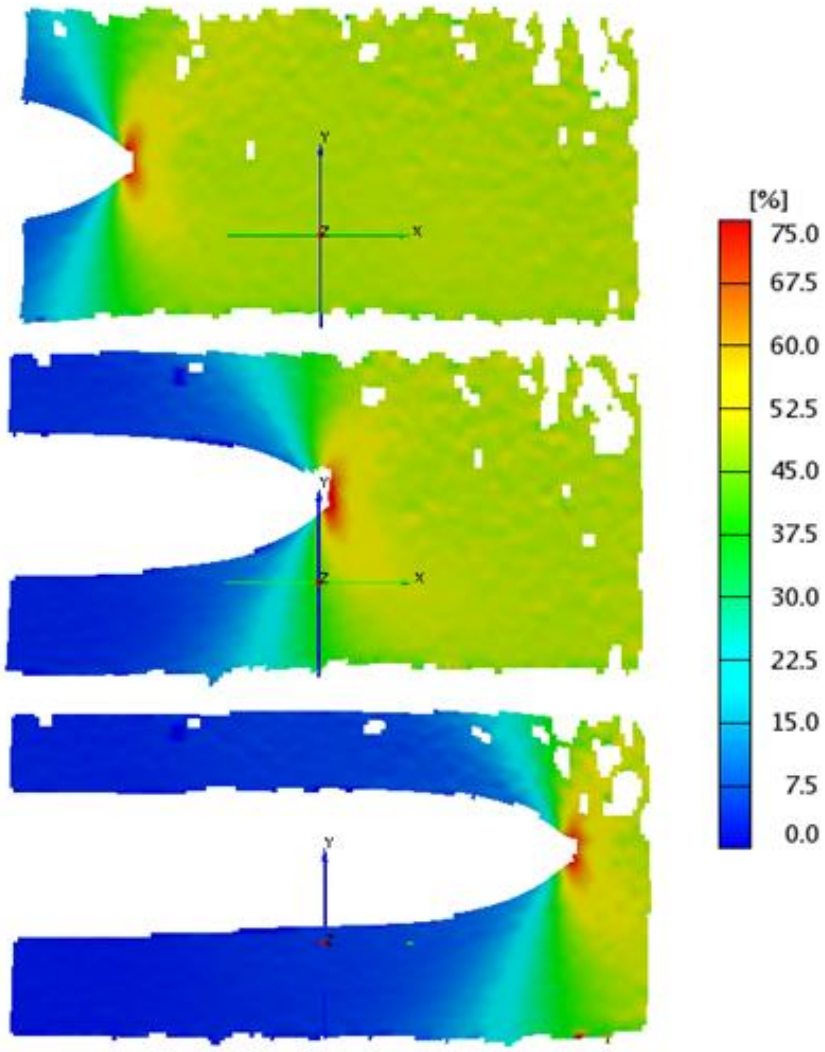

Figure G-1: DIC system images of the strain in the Y-direction for a fixed strain constrained tension fracture sample of Hydrogel A loaded to 50% strain

Appendix H: Correlation between Tan δ and Fracture Energy

In order to investigate a correlation between the master curves of the subcritical fracture energy curves and the loss factor tan δ at a reference temperature of 45oC a characteristic length value was needed in order to convert the crack propagation rate data from the fracture study of Hydrogel A and B into a frequency. There are several methods to determine the appropriate characteristic length value necessary for this correlation. Generally, the radius of the process zone serves as a good characteristic length; however, since there is no observed plastic deformation of the hydrogel samples this distance is not applicable. Therefore, the initial height, h_o, of the constrained tension samples was used as the characteristic length and proved to make relatively good correlation between the fracture energy and loss factor for both Hydrogel A and B as shown below in Figure G-1 and Figure G-2, respectively. Lastly, Figure G-3 depicts the correlation between the fracture energy and loss factor for each hydrogel system at several frequencies.

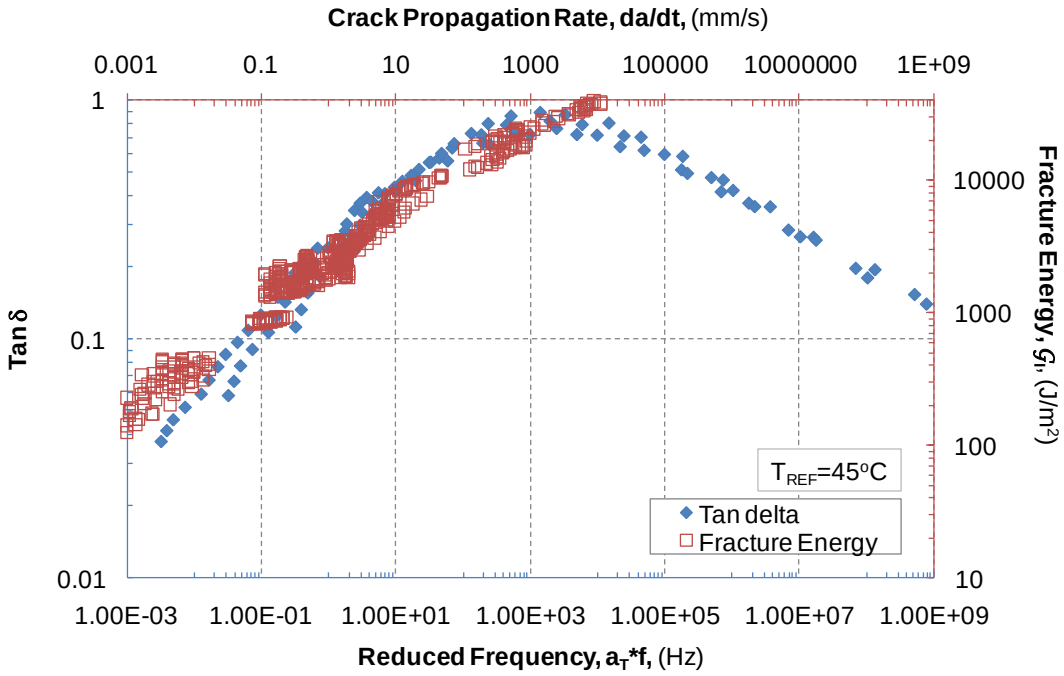

Figure G-1: Correlation between fracture energy and tan δ for Hydrogel A

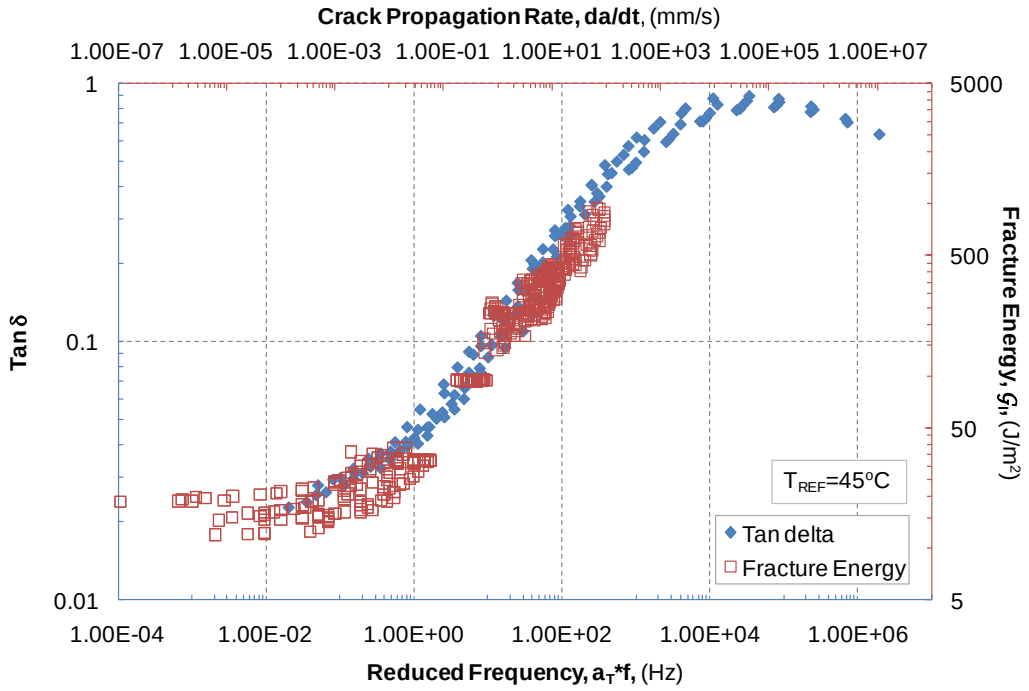

Figure G-2: Correlation between fracture energy and tan δ of Hydrogel B

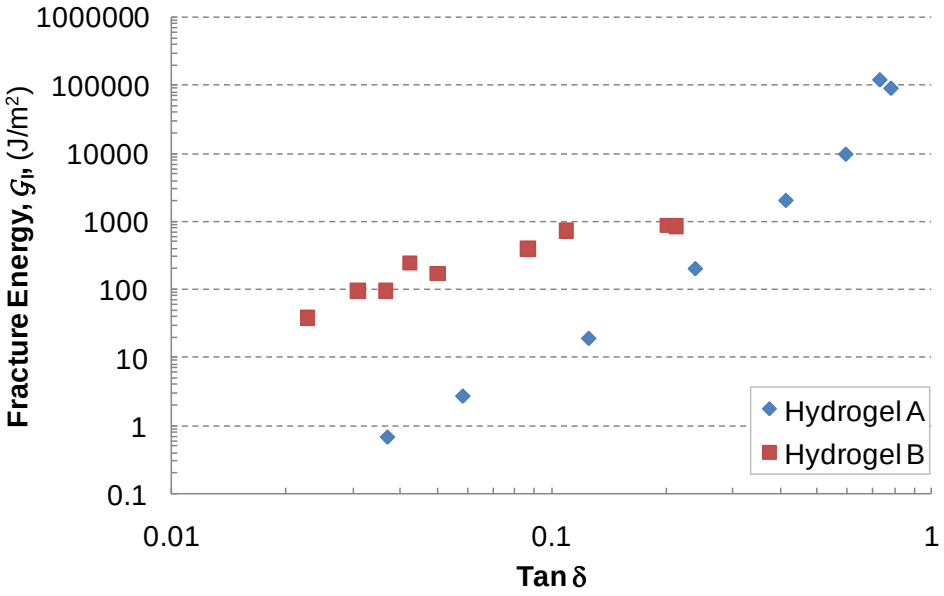

Figure G-3: Correlation of fracture energy and loss factor for Hydrogel A and B at several different frequencies

Appendix I: Effect of Temperature on Tearing Force for Hydrogel A and B

The effect of temperature on the tearing force required to initiate crack propagation in a constrained tension fracture specimen under the increasing strain loading condition, as discussed in Chapter 4, was investigated. On a load versus crosshead displacement plot for a constrained tension sample of Hydrogel A or B loaded in increasing strain, the tearing force was estimated to occur at the break or deviation in linearity of this plot, as shown in Figure H-1, and not the peak load. Using this method, the average tearing force was shown to increase with a decrease in temperature for Hydrogel A, while it proved to remain relatively the same with a decrease in temperature for Hydrogel B. This temperature dependence trend for Hydrogel A is similar to the dynamic mechanical analysis and uniaxial tension results presented in Chapter 3.

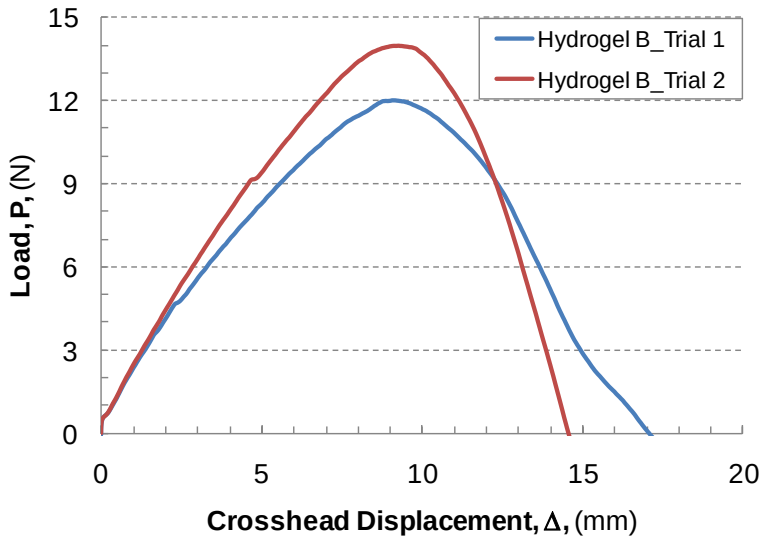

Figure H-1: Load-displacement curve for Hydrogel B loaded under increasing strain at 0^{o}C

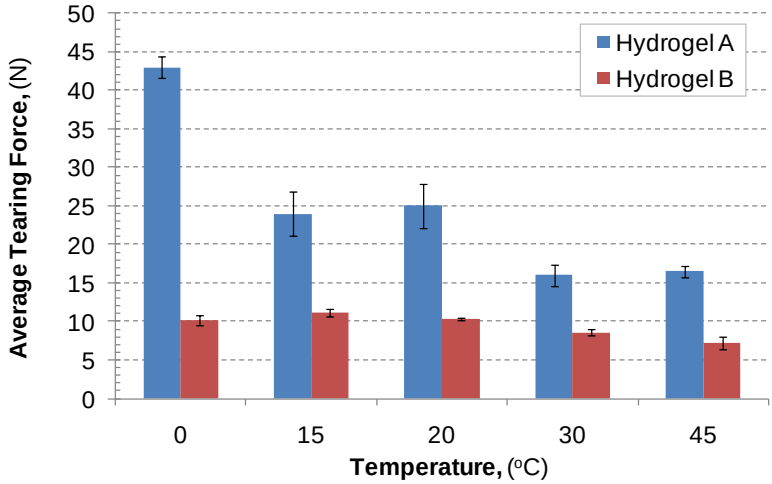

Figure H-2: Average tearing force for Hydrogel A and B at each temperature level